STRUCTURE AND MAGNETIC PROPERTIES OF Ni/NiO, Co/CoO COMPOSITE FILMS

YI JIABAO

(***B. ENG. TIANJIN UNIV. CHINA***)

A THESIS SUBMITTED

FOR THE DEGREE OF DOCTOR OF PHILOSOPHY

DEPARTMENT OF MATERIALS SCIENCE

NATIONAL UNIVERSITY OF SINGAPORE

2007

ACKNOWLEDGEMENTS

First and foremost I will offer my most sincere gratitude to my supervisor, Dr Ding Jun, who has supported me throughout my thesis with his immense patience and knowledge whilst allowing me the space to work in my own way. Without his encourage and effort, this thesis would not have been completed and written. I really appreciate his efforts in imparting the knowledge of materials science and magnetic materials. The novel and creative ideas given by Dr. Ding were indispensable to my research during the period of my PhD candidature in the Department of Materials Science and Engineering, National University of Singapore.

I would also like to acknowledge Prof. Feng Yuanping for the first principle calculations of NiO. I am truly indebted to the members of magnetic materials group in the Department of Materials Science and Engineering, who have been extremely helpful with their kind assistance and friendships. The active discussions throughout the study were most beneficial and resourceful. Special thanks are given to the lab officers of the Department of Materials Science and Engineering due to their technical support. I would also like to express my utmost gratitude to the financial support provided by the National University of Singapore.

Last but not least, I am especially grateful to my wife, Tong Ying, and son for their encouragement, utmost care and support throughout the entire execution of the project.

Publications during PhD study

1. **J.B. Yi**, Y.Z. Zhou, J. Ding, G.M. Chow, Z.L. Dong, T. White, X.Y. Gao, A.T.S Wee, and X.J. Yu, "An investigation of structure, magnetic properties and magnetoresistance of Ni films prepared by sputtering" ***J. Magn. Magn. Mater.*** 284, 303 (2004).

2. Y.C. Wang, J. Ding**, J.B. Yi**, B.H. Liu, T. Yu, Z.X. Shen, "High Coercivity Co-ferrite thin films on (100)-SiO_2 substrate" ***Appl. Phys. Lett***. 84, 2596 (2004).

3. H. Pan, B.H. Liu, **J.B. Yi**, C. Poh, S. Lim, J. Ding, Y. P. Feng, and J.Y. Lin, "Magnetic properties of single crystalline Ni and Co nanowires", ***J. Phys. Chem. B*** 109, 3098 (2005).

4. **J.B. Yi**, J. Ding, Z.L. Zhao, and B.H. Liu, "High coercivity and exchange coupling of Ni/NiO nanocomposite film" ***J. Appl. Phys***. 97, 10*K* 306 (2005).

5. **J.B. Yi** and J. Ding, "Exchange coupling in ferromagnetic/antiferromagnetic nanohybrid films" ***Solid state phenomenon*** 11, 175 (2006).

6. **J.B. Yi** and J. Ding, "Exchange coupling in amorphous CoO/crystalline Co bilayer". ***J. Magn. Magn. Mater***. 303, 160 (2006).

7. Z. L. Zhao, J.S. Chen, J. Ding , **J. B. Yi**, B. H. Liu, and J.P. Wang, "Formation and microstructure of high coercivity FePt thin films deposited at 400 ^oC" ***Appl. Phys. Lett.*** 88, 052503 (2006).

8. H. Pan, **J.B. Yi**, B.H. Liu, S. Thongmee, J. Ding, Y.P. Feng, J.Y. Lin, "Magnetic properties of highly-ordered Ni, Co and their alloy nanowires in AAO templates". ***Solid State Phenomenon*** 111, 123 (2006).

9. S.L. Tey, M.V. Reddy, G.V. Subba Rao, B.V.R. Chowdari, **J.B. Yi**, J. Ding, and J.J. Vittal, "Synthesis, structure and magnetic properties of $[Li(H_2O)M(N_2H_3CO_2)_3]\cdot 0.5H_2O$ (M = Co,Ni) as Single Precursors to $LiMO_2$ Battery materials" ***Chem. Mater.*** 18, 1587 (2006).

10. **J.B. Yi**, X.P. Li, J. Ding, and H.L. Seet, "Study of the grain size, particle size and roughness of substrate in relation to the magnetic properties of electroplated permalloy", ***J. Alloy and Comp.*** 428, 230 (2007).

11. X.P. Li, **J.B. Yi**, J. Ding, C.M. Koh, and H.L. Seet, J.H. Yin, S. Thongmee, "Effect of sputtered seed layer on electrodeposited $Ni_{80}Fe_{20}$/Cu composite wires" ***IEEE, Trans. Magn.*** 43, 2983 (2007).

12. **J.B. Yi**, X.P. Li, J. Ding, J.H. Yin, S. Thongmee, H.L. Seet, "Microstructure evolution of $Ni_{80}Fe_{20}$/Cu composite wires deposited by electroplating under an applied field" ***IEEE, Trans. Magn.*** 43, 2980 (2007).

13. **J.B. Yi**, Y.P. Feng, J. Ding, G.M. Chow. B.H. Liu, and J.H. Yin. "Evolution of structural and magnetism of NiO from amorphous, clusters to nanocrystalline" ***Phys. Rev. B*** 76, 224402 (2007).

14. H. Pan, **J.B. Yi**, R.Q. Wu, S. Lei, J.H. Yang, J.Y. Lin, Y.P. Feng, J. Ding, L.H. Van, and J.H. Yin "Room temperature ferromagnetism in carbon-doped ZnO" ***Phys. Rev. Lett***. 99, 127201 (2007).

Table of Contents

Summary

This project focused on understanding of the magnetic properties of Ni and NiO in the amorphous or disordered, cluster, nanocrystalline and well crystalline states and the understanding of the exchange coupling and magnetic behaviors of ferromagnetic/antiferromagnetic Ni/NiO nanocomposites. In this study, nanostructured samples were fabricated by co-precipitation and magnetron sputtering. It was found that NiO exhibited antiferromagnetism in a fully amorphous state with a very low Néel temperature. Ferromagnetism was observed in NiO clusters. NiO/Ni composite prepared by sputtering after annealing possessed high values of saturation magnetization at room temperature (up to 91 *emu/g*, which is more than two times larger than that of bulk Ni) due to a strong exchange coupling between Ni crystallites and NiO clusters. It has been found that NiO with a grain size of 2－4 *nm* is ideal for achieving a high coercivity in a Ni/NiO exchange coupling system. A coercivity of 2.4 *kOe* at room temperature has been achieved in a Ni/NiO composite prepared by magnetic annealing. Similarly, high coercivity has also been obtained in a Co/CoO nanocomposite prepared by magnetic annealing. Hence, the method of magnetic annealing is suitable to achieve high coercivity materials, which may be promising for the applications of hard magnets. Based on the investigation of this work, the contribution of the project is summarized below:

1) In this project, a whole picture of the structure and magnetic properties of NiO in the amorphous, cluster, nanocrystalline, and well crystalline state was well described. The study showed that amorphous NiO was antiferromagnetic. Clustered NiO was ferromagnetic with a maximum magnetization of 105 *emu/g* at

2 *K*. Nanocrystalline NiO was composed of surface spins or antiferromagnetic core. The magnetization of the nanocrystalline NiO was contributed from the surface spins. However, the magnetization was small. Strong exchange coupling with an exchange bias was observed in this nanocrystalline NiO. First principle calculation is in good agreement with the experimental results.

2) The composite of Ni/NiO prepared by sputtering annealed at 200 ^{o}C in an argon atmosphere showed a saturation magnetization of 91 *emu/g* at room temperature. In addition, in this study, a high coercivity was achieved at low temperatures (5—40 *K*) when the annealing was carried out at 350 ^{o}C.

3) Ni/NiO composite prepared by magnetic annealing showed a coercivity of 2.4 *kOe* at room temperature. This value is significant since Ni is one of the soft magnetic materials and has a low coercivity. The study of the mechanisms indicated that the high coercivity of the composite was due to the exchange coupling between Ni and NiO. The small grain size of NiO was attributed to the high coercivity. Similarly, high coercivity was achieved in a Co/CoO composite prepared by magnetic annealing. The coercivity of the composite is evidently higher than that prepared by sputtering under an oxygen partial pressure (reactive sputtering). The remanence was also enhanced.

List of Tables

List of Figures and Illustrations

Chapter 1

Introduction

This chapter gives an overview of the origins and types of magnetism. The chapter reviews the study of the exchange coupling between ferromagnets and antiferromagnets. The current development of the theories on exchange coupling is introduced. Factors, such as grain size, roughness, thickness and orientation of the antiferromagnet that affects exchange bias and coercivity, are discussed. Finally, the finite size effect is reviewed and discussed.

1.1 Brief Review of Magnetic properties of Materials

1.1.1 Origin of magnetism

Magnetic phenomena originate from the quantized angular momentum of orbiting and spinning atomic electrons. Four quantum parameters can determine the magnetic moment based on Hund's rules. The principle quantum number n determines the energy and size of the shell of an electron. The orbital angular momentum quantum number l determines the energy level of the splitting subshell, corresponding to *s,p,d,f*. m_l determines the orbital angular momentum along the applied magnetic field. m_s determines the component of spins along the applied magnetic field.

In a crystal with 3*d* transition metal ions, the orbital moment of 3*d* ions can be quenched because of the high molecular field inside the crystal. Hence orbital moment does not contribute to the magnetic moment. The moment is contributed from the electron spins. However, recently studies showed that the orbital moment was not completely quenched and it makes a small contribution to the magnetic moment [1].

1.1.2 Type of magnetism

1.1.2.1 Diamagnetism

Diamagnetism refers a fundamental property of all materials, though it is usually very weak. It is due to the non-cooperative behavior of orbiting electrons when exposed to an applied magnetic field. Diamagnetic substances are composed of atoms which have no net magnetic moments (i.e., all the orbital shells are filled and there are no unpaired electrons). When a diamagnetic material is exposed to a magnetic field, a negative magnetization is produced and thus the susceptibility is negative.

1.1.2.2 Paramagnetism

In a paramagnetic material, some of the atoms or ions have a net magnetic moment due to unpaired electrons in partially filled orbitals. The individual magnetic moments do not interact magnetically like diamagnetism. The magnetization is zero when the field is removed. In the presence of a field, there is a partial alignment of the magnetic moments in the direction of the magnetic field, resulting in a net positive magnetization and positive susceptibility.

Paramagnetism can be described by Langevin theory [2]. In the Langevin theory, the magnetic moments are non-interacting. The well-known Langevin equation (1.1) is shown below:

$$M = NmL(\alpha) = Nm\left[\coth\alpha - \frac{1}{\alpha}\right] \tag{1.1}$$

The function in the bracket is the Langevin function, $L(\alpha)$, and $\alpha = \frac{mH}{kT}$, where M is magnetization; N is the total number of moments per unit volume; m is the net atomic

magnetic moment; H is the applied field; K is the Boltzmann constant; T is the absolute temperature. It is derived from Equation 1.1 that, as $\alpha \to \infty$, $L(\alpha)$ approaches 1. Thus, as $H \to \infty$, M approaches Nm. It means that all the moments tend to be perfectly parallel. On the other hand, as α is much smaller than 1, the Langevin function may be expanded as Equation 1.2.

$$L(\alpha) = \frac{\alpha}{3} - \frac{\alpha^3}{45} + \cdots \tag{1.2}$$

After neglecting the terms beyond the first term of Equation 1.2, and replacing α with $\frac{mH}{kT}$, one can get the Equation 1.3.

$$M = \frac{Nm^2}{3kT} H \tag{1.3}$$

This yields the field independent susceptibility,

$$\chi = \frac{M}{H} = \frac{Nm^2}{3kT} \tag{1.4}$$

Equation 1.4 is the mathematic expression of the well-known Curie law, namely, the *1/T* dependence of the susceptibility of a paramagnetic substance on the temperature. The curve is shown in Fig. 1.1.

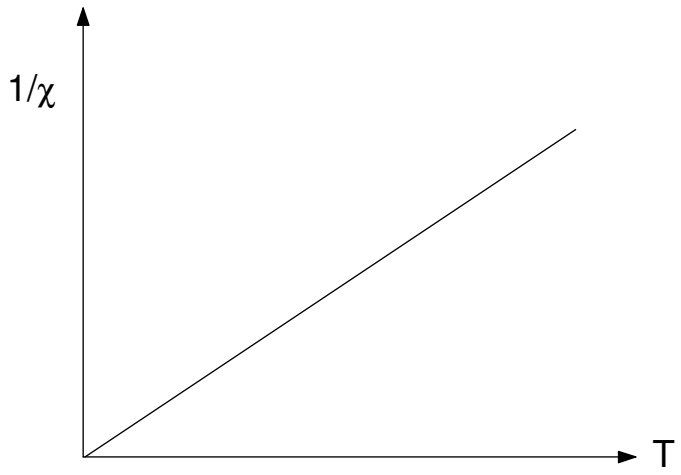

Fig. 1.1. A graphic illustration of 1/χ versus T for a paramagnet.

1.1.2.3 Ferromagnetism

In some magnetic materials, the atomic moments exhibit very strong interactions. These interactions are very large, equivalent to a magnetic field in the order of 1000 *tesla*, or approximately 100 million times of the strength of the earth's magnetic field. The exchange force is a quantum mechanical phenomenon due to the relative orientation of the spins of two electrons.

Weiss firstly postulated the presence of a strong inner magnetic field, namely molecular field, and developed a theory to describe the temperature dependence of the saturation magnetization [3]. According to his theory, the molecular field is proportional to the magnetization of the ferromagnet. Hence, the molecular field is expressed below:

$$H_m = wM \qquad (1.5)$$

where w is the proportionality factor, M is the magnetization.

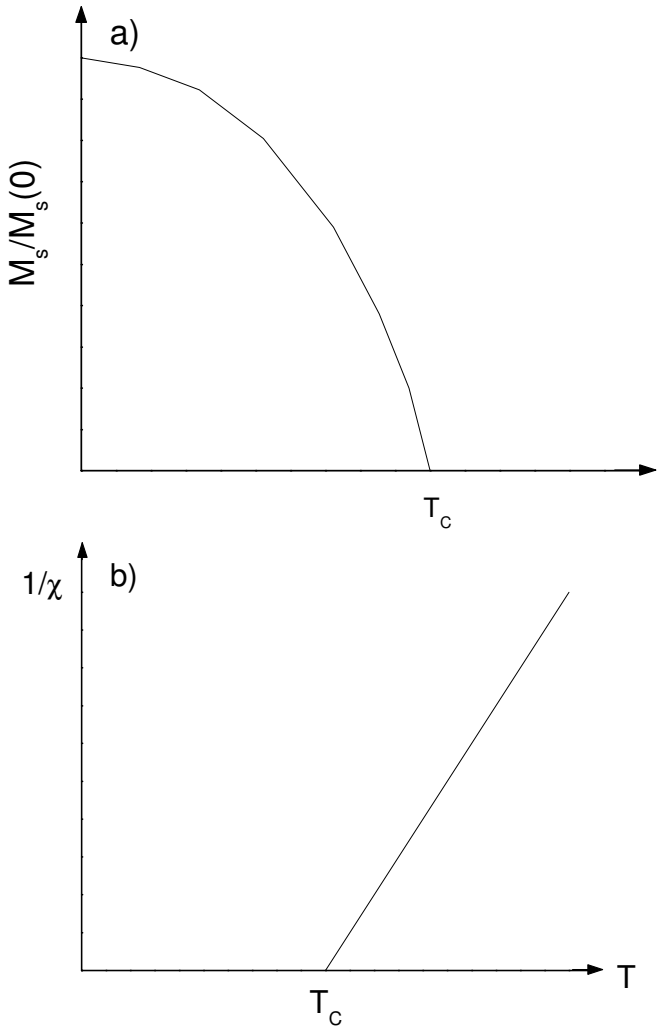

Fig. 1.2. a) The magnetization dependence on the temperature for a ferromagnetic material below the Curie temperature T_C; b) the susceptibility as a function of temperature of a ferromagnetic material above T_C.

When a magnetic field H is applied parallel to the magnetization M of the system, an individual atomic moment has the potential energy U_H

$$L(\alpha) = \frac{\alpha}{3} - \frac{\alpha^3}{45} + \cdots \tag{1.6}$$

From the statistics, the average magnetization M is given by

$$M = NmL\left\{\frac{m(H+wM)}{kT}\right\} \tag{1.7}$$

From Equation (1.7), one can derive Equation (1.8), when the temperature $T>T_C$.

$$\frac{1}{\chi} = \frac{H}{M} = \frac{3k(T-T_C)}{Nm^2} \tag{1.8}$$

Equation (1.8) means that the susceptibility above the Curie temperature is inversely proportional to $(T-T_c)$, which are called the Curie-Weiss law, as shown in Fig. 1.2b. Below T_C, the curve between magnetization and Curie temperature is shown in Fig. 1.2a.

1.1.2.4 Antiferromagnetism

In some magnetic materials, the structure contains two sub-lattices. The two sub-lattices have magnetic moment with the same magnitude but the opposite direction, due to the negative charge coupling. Hence the net magnetic moment is zero, as shown in the Fig. 1.3.

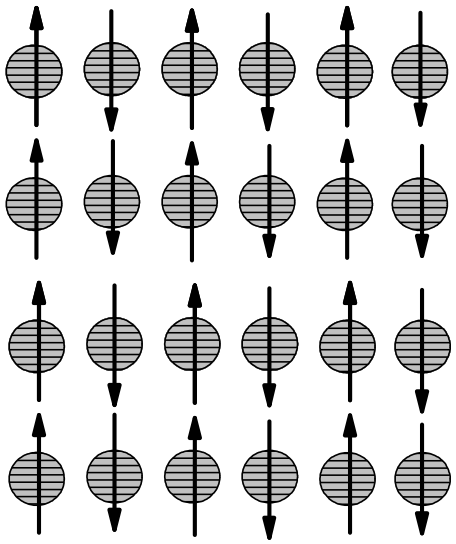

Fig. 1.3. Configuration of spin array in an antiferromagnet.

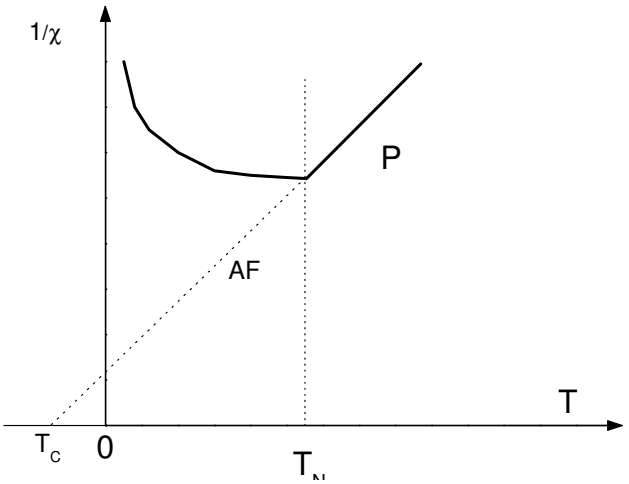

Fig. 1.4. The susceptibility as a function of temperature (T_N is the Néel temperature). AF: Antiferromagnetism; P: paramagnetism.

1.1.2.5. Ferrimagnetism

Ferrimagnetism is a term proposed by Néel [4] to describe the magnetism of ferrites. In these substances, magnetic ions occupy two kinds of lattice sites, A and B. Spin on A sites align antiparallel to those on B site because of the strong negative interaction acting between the two spin systems. Since the number of magnetic ions and the magnitude of spins of individual ions are different on A and B sites, such an order arrangement of spins gives rise to a resultant magnetization. Hence, ferrimagnetic materials show a magnetization without the action of any external magnetic field. With increasing the temperature, the arrangement of the spins is disturbed by thermal agitation, which is accompanied by a decrease in spontaneous magnetization until Curie temperature, at which ferrimagnetism changes to paramagnetism.

1.2 Hysteresis loops

Important parameters of ferromagnetic and ferromagnetic materials can be obtained from the hysteresis loop, as shown in Fig. 1.5. The net magnetization of a magnet in the pristine state is zero due to the random distribution of magnetic domains. After applying a magnetic field, there is a domain wall displacement before the domain rotation, which follows the direction of the magnetic field. The net magnetic moment increases with increasing the applied magnetic field. If the magnetic field is large enough, all the domains will turn to the same direction as that of the applied field. The magnetization is saturated, called saturation magnetization. The magnetization curve is called the initial curve. If the applied field is reduced to zero, the domains then gradually relax to its easy axis. The magnet will have a remnant magnetization, called remanence. If the magnetic field is increased continuously in the negative direction, the magnetization will be reduced to zero at a certain applied magnetic field. The

magnetic field is called coercivity. If the negative applied field is large enough, the negative saturation magnetization can be obtained. All the domains follow the same direction as that of the negative applied field. The curve of magnetization versus the applied field formed by the cycled magnetic field is called a hysteresis loop.

In general, the coercivity is strongly dependent on the magnetic crystalline anisotropy. Large crystalline anisotropy can lead to a high coercivity. However, the coercivity is evidently affected by other factors, such as vacancies, dislocations and grain boundaries of the magnet. In addition, the coercivity can also be affected by the shape, stress and the preparation method. For instance, an additional magnetic anisotropy can be induced by magnetic annealing in ferrite system [5]. Another important anisotropy is the exchange anisotropy, as described in 1.3.

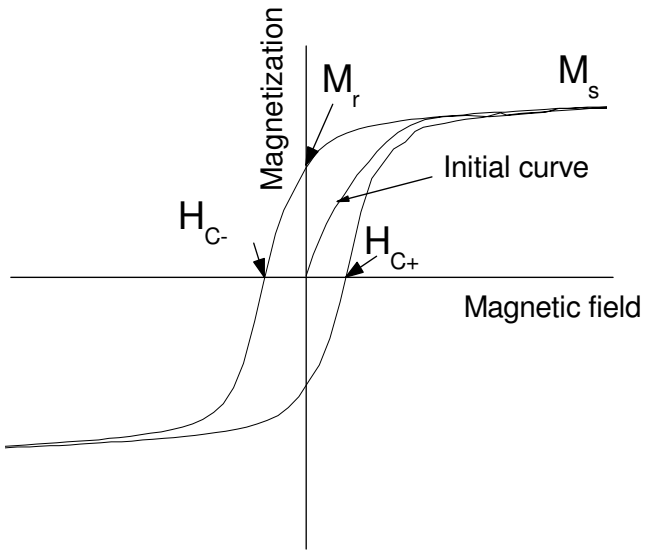

Fig. 1.5. Typical hysteresis loop of a magnetic material.

1.3 Exchange coupling between ferromagnets and antiferromagnets

1.3.1 Theories

Meiklejohn and Bean [6] have discovered the exchange bias in the oxidized fine cobalt powders, known as Co/CoO core/shell. The hysteresis loop shifted to the negative field direction when a Co/CoO core/shell sample was cooled under a magnetic field. The shifted hysteresis loop is shown in Fig. 1.6. In this project, the exchange bias is defined as $H_E = |H_{C-}| - |H_{C+}|$. Here, H_E is the exchange bias; H_{C-} is the negative coercivity; and H_{C+} is the positive coercivity. In the practical applications of hard/permanent magnetic materials, the maximum energy product $(BH)_m$, which characterizes the strength of a magnet, is calculated from the second quadrant. Hence, the coercivity in the negative direction, H_{C-}, determines the magnetic properties in hard magnets. The coercivity of this project is defined as $H_C = |H_{C-}|$.

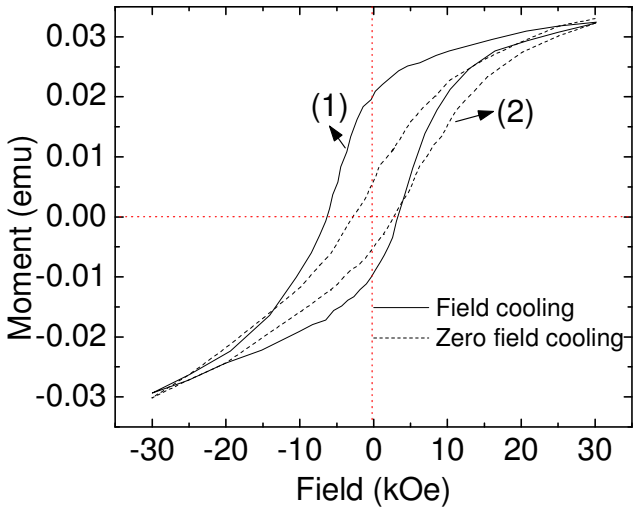

Fig. 1.6. Curve (1) shows the resulting loop after cooling antiferromagnet/ferromagnet above the Néel temperature of the antiferromagnet under a magnetic field. Curve (2) shows the loop when cooled in zero field.

Meiklejohn and Bean [6] interpreted the phenomenon as the exchange coupling between the ferromagnet and antiferromagnet through their interface. The exchange coupling between an antiferromagnet (AFM) and ferromagnet (FM) is shown in Fig. 1.7a. The ferromagnet spins are coupled with antiferromagnet spins after cooling above the Néel temperature of the antiferromagnet. For the convenience of the study,

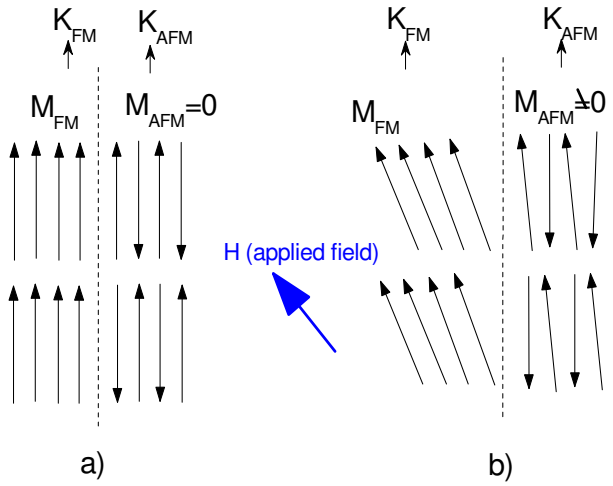

Fig. 1.7 a) The description of the spin state in an antiferromagnet (AFM) and ferromagnet (FM) exchange coupling system; b) the change of the magnetization of the ferromanget component (M_{FM}) and antiferromagnet component (M_{AFM}) after applying a magnetic field, as shown in the graph.

it is assumed that the anisotropy directions of the antiferromagnet and ferromagnet are the same, as shown in the Fig. 1.7a. The easy magnetization direction of the ferromagnet is also the same as that of the antiferromagnet. The net magnetization of the antiferromagnet is zero since the antiferromagnet spins have the same magnitude but opposite directions. If a magnetic field is applied, as shown in Fig.1.7b, the magnetization of the ferromagnet will follow the direction of the applied field. A small magnetization of the antiferromagnet can be observed. The magnetization also follows the direction of the applied field. The change of the magnetization after applying a

magnetic field is shown in Fig. 1.7b. The directions of an applied field (H), the magnetization of the ferromagnet (M_{FM}), the magnetization of the antiferromagnet (M_{AFM}) and the anisotropy of the antiferromagnet and ferromagnet are illustrated in Fig. 1.8.

Assuming a coherent rotation of the magnetization of a ferromagnet and antiferromagnet, the energy per unit area can be written as:

$$E = -HM_{FM}t_{FM}\cos(\theta-\beta) + K_{FM}t_{FM}\sin^2(\beta) + K_{AFM}t_{AFM}\sin^2(\alpha) - J_{INT}\cos(\beta-\alpha) \quad (1.10)$$

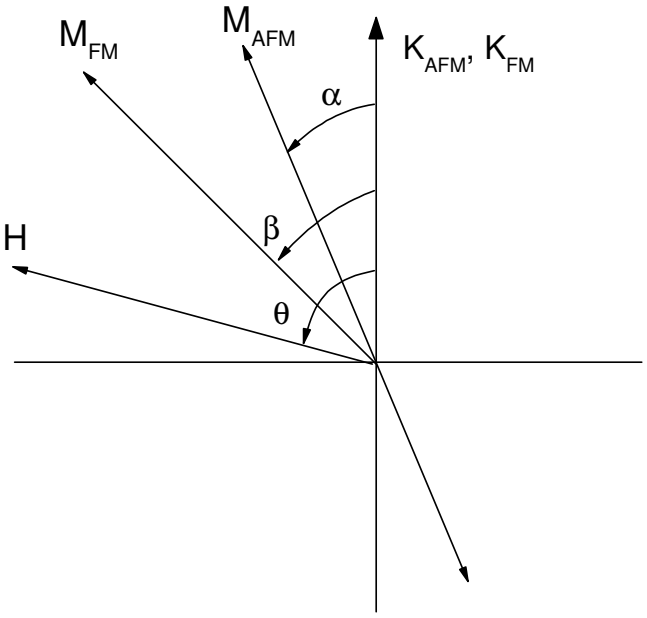

Fig. 1.8 The description of the AFM and FM angles related with the magnetization, anisotropy and applied field. Note that the AFM and FM anisotropy axes are assumed collinear and that the AFM sub-lattice magnetization M_{AFM} has two opposite directions.

Here, the antiferromagnet and ferromagnet anisotropy axes are assumed to be in the same direction, as discussed in the previous paragraphs. β, α, and θ are the angles between the magnetization and the ferromagnet anisotropy axis, the antiferromagnet sub-lattice magnetization (M_{AFM}) and the antiferromagnet anisotropy axis, the applied

field and the ferromagnet anisotropy axis (Fig. 1.7). Neglecting the ferromagnet anisotropy, which is generally considerably much smaller than the K_{AF}, and minimizing respect to α and β, the hysteresis loop shift can be obtained

$$H_E = \frac{J_{F/AF}}{a^2 M_F t_F} \tag{1.11}$$

where $J_{A/AF}$ is the exchange parameter; a is the lattice parameter; M_F is the ferromagnet saturation magnetization. t_F is the ferromagnet thickness. Here, the order of magnitude of H_E depends on the unknown parameter $J_{F/AF}$, a feature common to all of the theoretical models developed in the exchange bias context. Assuming $J_F \geq J_{AF-F} \geq J_{AF}$, the resulting value for H_E is orders of magnitude larger than experimentally observed [7]. For the potential applications in the permanent magnet [8], magnetic recording media [9, 10], magnetic random access memory (MRAM) and domain stabilizer based on the anisotropic magneto-resistance [11], the phenomenon was widely investigated and many theories have been proposed, such as uncompensated antiferromagnet spin theory developed by Néel [12]; domain wall model by Mauri *et al* [13]; random interface model by Malozemoff [14]; orthogonal ferromagnet/antiferromagnet magnetization model by Koon [14]. Recently, Schulthess and Butler [16, 17] proposed a new model to combine Molozemoff's random interface field and Koon's orthogonal magnetic arrangement. The above theories can explain most of the experiment results. However, in experiments, different researchers may obtain opposite results. In some experiments, the magnitude of exchange bias (H_E) decreased with increasing roughness [18, 19]. Some systems appeared to be less sensitive to roughness or behaved in the opposite way. Other parameters such as the crytallinity [20], interface impurity layers [21], anisotropy [22], ferromagnet thickness [18, 23], antiferromagnet thickness [24-26] affected the exchange bias greatly. Among

these parameters, the grain size effect in exchange bias remains unclear. The effect of grain size is expected to be similar to the thickness effect discussed in the previous part. However, the effect of the grain size may be related with other parameters, such as the crystallinity, texture, spin structure and antiferromagnet anisotropy [26-29]. Hence it was reported that H_E increased with increasing grain size in some systems. In other systems, H_E decreased with increasing grain size [27, 28, 30].

1.3.2 High Coercivity in exchange coupling system

From the discovery of the exchange bias in the oxidized cobalt fine particles by Meiklejohn and Bean [6], the hysteresis loop also showed a large coercivity beside showing a shift of the hysteresis loop. The large coercivity is attributed to be due to the exchange coupling between an antiferromagnet and ferromagnet. Recently, the coercivity behavior in exchange coupling systems was widely studied. Leighton *et al.* studied the Fe/FeF_2 system to show that spin disorder (spin frustration) may be one of the reasons for the high coercivity [31]. Koon and Schulthess *et al.* showed that spin flopping of the antiferromagnet may be one of the important reasons for the increase in the coercivity [15, 16]. Zhang [32] proposed a random field anisotropy model to explain the increase in the coercivity in an exchange coupling system. The increase in the coercivity was thought to be the random field anisotropy due to the exchange coupling between the antiferromagnet and ferromagnet. The random anisotropy was produced by the inhomogeneous exchange coupling, which induced small energy barriers. The small grain size of an antiferromagnet may play an important role in the inhomogeneous coupling. This is because the random easy axis of the small grain size may lead to a lot of small energy barriers. However, the coercivity is also dependent on

many other parameters, such as the microstructure, thickness and grain size of the antiferromagnet and ferromagnet [33].

1.3.3 ΔM curves

Magnetic interaction can be used for the investigation of the mechanisms of coercivity [34, 35]. ΔM curves can be used in the study of the interaction state of magnetic thin films [36,37]. The equation of delta curve was derived by Kelly *et al* [38] to account for the interactions between magnetic particles by modifying Wohlfarth relation [39].

$$\Delta M(H) = M_d(H) - [1 - 2M_r(H)] \quad (6.1)$$

where M_d *(H)* is the DC demagnetization (DCD) remanence and M_r *(H)* is the isothermal remanence (IRM).

For the recording of a DCD curve, firstly, the sample is saturated with a sufficiently high positive magnetic field. Then a reverse field is applied and the demagnetization remanence magnetization is measured when the reverse field is reduced to zero. The measurement is then cycled with increasing the reverse field until the negative saturation is reached.

The curve of IRM is measured on the pristine or well demagnetized magnetic material. The sample is firstly applied with a positive magnetic field. Secondly, the applied field is removed and the remnant magnetization is recorded. The measured process is cycled with an increment of the applied field until the saturation of the sample. The IRM curve is obtained by plotting the remnant magnetization versus the applied field. In the above equation, if the $\Delta M(H)$ is positive, it is usually associated with the exchange

coupled granular systems [40]. If $\Delta M(H)$ is negative, it suggests that interaction in the film may be attempting to demagnetize the material.

1.3.4 Antiferromagnet in the exchange coupling

An antiferromagnet is one of the important components of an exchange coupling system. The microstructure of an antiferromagnet, such as grain size, interface roughness, interface domain structure, the orientation *etc*.[33], will greatly affect the properties, as discussed previously. There are many kinds of antiferromagnets. In the early works after Meiklejohn and Bean's discovery of the exchange bias in the oxidized CoO particles, CoO, NiO and FeO metal oxides were widely investigated in the antiferromagnet/ferromagnet systems. Other oxides such as CoNiO and NiFeO were also studied through the oxidation of metallic CoNi and NiFe particles. Later, for practical applications, Mn based antiferromagnets were developed. For example, $Fe_{50}Mn_{50}$, one of the most widely studied materials for its high blocking temperature, has high interface energy and is easily prepared [41-48]. It has been extensively used in spin valve systems. Other compounds such as Ni_xMn_{1-x}, $Cr_xMn_yM_{1\sim x\sim y}$, where M = Pd, Ir, Ni,Co, Pt, Rh, Cu, Ti , $Pd_xPt_yMn_{1\sim x\sim y}$, Co_xMn_x, $Fe_xMn_yRh_{1\sim x\sim y}$ and $Cr_xAl_{1\sim x}$ were investigated and explored for their good corrosion properties and high Néel temperature. Other antiferromagnets, for example, FeF_2 and MnF2 [33, 49], are normally used for the mechanism investigation since they have clear and simple structures.

1.3.5. NiO and CoO in exchange coupling

After the discovery of exchange coupling in oxidized Co particles, CoO was widely studied. Gangopadhyay *et al.* [50-52] studied the oxidized CoO particles and the

bilayer of ferromagnet/CoO [53]. The effect of the microstructure on the exchange bias and coercivity behavior was studied [52]. However, due to its low Néel temperature (292 *K*), it cannot be used for practical applications. Recently, NiO has attracted great interest for its high Néel temperature (520 *K*), chemical stability and clear microstructure. In addition, NiO has a melting temperature as high as 1960 ^{o}C and has a density of 6.7 g/cm^3. It has a cubic structure, which is similar to that of CoO. The structure is shown in Fig. 1.9. The antiferromagnetic NiO crystallizes in a rock-salt structure with a lattice constant of 5.417 *Å*. In a NiO unit cell, the spins are ferromagnetically coupled within the (111) planes whereas the spins of alternating (200) planes are antiferromagnetically coupled. The magnetic anisotropy constant *K is* 3.3×10^5 J/m^3 [54]. Hence, spin valve structures with a NiO film as the pinning layer have been reported [25, 55, 56]. The grain size effect, texture, orientation, stress effect and domain structure on the exchange bias have also been widely studied [56, 57]. However, the investigation of the exchange bias and coercivity in a NiO/ferromagnet system is limited. This is due to the fact that NiO has a low interface energy density when it is fabricated by common deposition methods, such as sputtering, CVD, MBE, PLD. In general, the exchange bias of a NiO/ferromagnet composite/bilayer is smaller than 100 *Oe*. Hence, many researchers are trying to know what the ultimate values of the exchange bias and coercivity in a NiO/ferromagnet systems could be obtained since the variation of interface energy density of NiO is very broad (0.05–0.29 erg/cm^3). The exchange bias of the confined structure with narrow arrayed Ni/NiO wires was investigated by Fraune *et al.* [58]. They observed an exchange bias of 300 *Oe* at 5 *K* and a coercivity of 600 *Oe*. The study showed that it might be possible to obtain a high coercivity and large exchange bias in a NiO/ferromagnet system. As studied by other researchers, the structure of the interface, grain size and the formation

of the domains in the interface between antiferromagnet and ferromagnet during the film deposition may affect the exchange bias and coercivity [59-61]. Hence, how to optimize these factors may be of importance to obtain the desired exchange bias and coercivity.

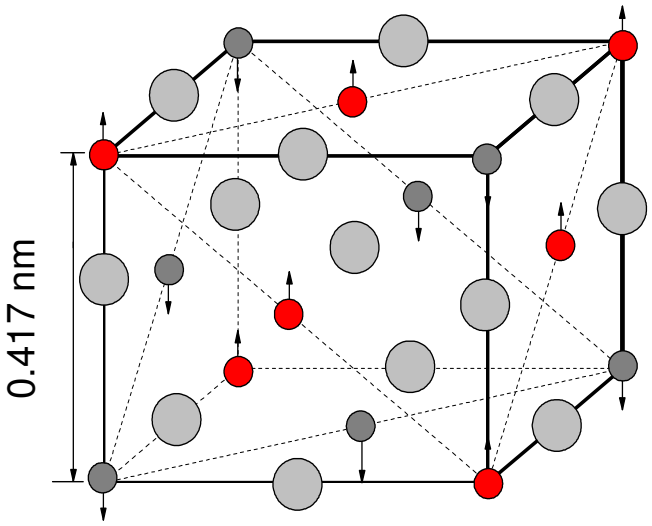

Fig. 1.9. The crystal structure of NiO. The arrows show the spin up and spin down in a NiO antiferromagnet (the larger diameter atom is oxygen ions, the smaller is the Ni ions).

1.4. Magnetization of NiO nanoparticles

It was predicted by Néel that the uncompensated spins would show a magnetic moment in an antiferromagnet [62]. As described above, NiO has a clear and simple structure, which is suitable for the study of the uncompensated moment. Large magnetic moment of NiO nanoparticles has been observed [63-65]. The surface spins were supposed to be attributed to the magnetization. Some researchers ascribed the magnetization to be related to Ni^{3+}. However, other researchers claimed that the magnetization was not related with Ni^{3+} at all [66,67]. Kodama *et al.* [67] observed that small NiO particles showed not only a large magnetic moment but also a high

coercivity together with a shift in the hysteresis loop at low temperature. The calculation of the nanoparticles showed that the spin configurations in the nanoparticles yielded 8, 6 or 4 sub-lattice configuration, indicating a finite size effect, in which the reduced coordination of surface spins caused a change in the magnetic order throughout the particles. Hence during magnetic reversal by applying a magnetic field, there were a number of paths. This kind of reversal may lead to the large coercivity and loop shift when the bulk and surface anisotropies are included. However, most of the exchange bias phenomena could be explained as the surface driven finite size effect due to the exchange coupling between the antiferromagnetic core and ferromagnetic surface spins. The large magnetization is not limited to NiO nanoparticles. For instance, relatively large magnetization was observed in CoO thin layer or small particles [68]. The magnetization of nanoparticles in other systems such as CuO, Co_3O_4, CoNiO, Ni_2FeO_4, Mn [69-73] was also widely investigated.

1.5 Motivations

Based on the introduction above, nanostructured materials show different properties from their bulk counterparts. NiO in the nanostructured state shows a high magnetization, though NiO is an antiferromagnet. The magnetic properties of the nanosized NiO have been widely investigated [63-65]. However, for all these studies, no one detailed study provides an entire picture of the magnetic properties of an antiferromagnet in the amorphous, cluster, nanocrystalline and bulk state.

The exchange coupling effect has attracted interest for its potential applications in spin valves, reading head, MRAM and hard disk drive [72-76]. In an exchange coupling system, a ferromagnet (FM) and an antiferromagnet (AFM) are coupled with each

other by field cooling above the Néel temperature of the antiferromagnet [6]. As discussed previously, this feature is beneficial to many applications. However, the mechanism is not well understood, though it has been widely studied [13-16]. The shift of the hysteresis loop in an exchange coupling system is strongly dependent on the interface roughness, morphology and domain structure [13-15]. Hence, the preparation method may greatly affect the exchange bias and coercivity in an antiferromagnet/ferromagnet system. In addition, another feature of the exchange coupled system is to obtain relatively large coercivity, which is important for hard magnet [11]. Moreover, the exchange coupling energy can stabilize the nanoparticles of ferromagnet to overcome superparamagnetism [77]. However, the mechanisms of the high coercivity are not well understood.

The major objectives of this work are shown below:

1) Synthesis of amorphous, nancluster, nanocrystalline and well crystalline NiO. The investigation of the properties of the synthesized NiO with different structures.

2) The fabrication of Ni/NiO composites using a sputtering technique. The study of the mechanisms of the high magnetization and coercivity of Ni/NiO composites. The study of Ni/NiO composites prepared by magnetic annealing. The investigation of the mechanisms of the high coercivity at room temperature.

3) The fabrication of Co/CoO composites by magnetic annealing. The investigation of the mechanisms of the high coercivity.

1.6 Summary

In this chapter, the terminologies related to the magnetism and exchange coupling are introduced. The discovery of the exchange bias and relatively large coercivity is reviewed, followed by the introduction of the theory development. The exchange coupling has attracted great interest due to the potential applications in the hard disk recording media and spintronic devices. The studies on the exchange coupling showed that the exchange coupling depends on the ferromagnetic and antiferromagnetic materials, the microstructure, interface formation, grain size and prepared condition of the antiferromagnet/ferromagnet composites. Hence, the preparation method is of importance, as described in the next chapter. In addition, the magnetization of nanosized antiferromagnet has been reviewed. The introduction leads to the motivation of the project. In this project, efforts are made to investigate the evolution of NiO magnetic properties from amorphous, cluster, nanocrystalline to crystalline structure. High magnetization materials will be obtained by the exchange coupling of NiO nanoclusters with ferromagnetic Ni films. High coercivity materials in the antiferromagnet/ferromagnet system can be achieved through the optimization of the preparation condition.

References

[1]. V. Fernandez, C. Vettier, F.D. Bergevin, C. Giles, and W. Neubeck, Phys. Rev. B 57, 7870 (1998).

[2]. S. Chikazumi, "Physics of magnetism", Krieger Publishing Company, Florida, USA, P7 (1978).

[3] P. Weiss, J. De Phys., 6, 661 (1907).

[4]. L. Néel, Ann. Physique 3, 137 (1948).

[5]. R.F. Penoyer and L.R. Bickford, Phys. Rev. 108, 271 (1957).

[6]. W. Meiklejohn and C.P. Bean, Phys. Rev. 102, 1413 (1956).

[7]. W. Meiklejohn, J. Appl. Phys. 33, 1328 (1962).

[8]. F.S. Luborsky, Electro-Technol. 9, 107 (1962).

[9]. M. Ohkoshi, K. Tamari, M. Harada, S. Honda, and T. Kusuda, IEEE Trans. J. Magn. Japan 1, 37 (1985).

[10]. A.A. Glazer, A.P. Potapov, and R.I. Tafirov, Sov. Phys. JETP. Lett. 15, 259 (1972).

[11]. C. Tang, J. Appl. Phys. 55, 2226 (1984).

[12]. L. Néel, Ann, Phys. (Paris) 2, 61 (1967).

[13]. D. Mauri, H.C. Siegmann, P.S. Bagus, and E. Kay, J. Appl. Phys. 62, 3047 (1987).

[14]. A.P. Malozemoff, Phys. Rev. B 35, 3679 (1987).

[15]. N.C. Koon, Phys. Rev. Lett. 78, 4865 (1997).

[16]. T.C. Schulthess and W.H. Butler, Phys. Rev. Lett. 81, 4516 (1998).

[17]. W.H. Bulter, J. Appl. Phys. 85, 5510 (1999).

[18]. J. Nogues, D. Lederman, T.J. Moran, I.K. Schuller, and K.V. Rao, Appl. Phys. Lett. 68, 3186 (1996).

[19]. D. Lederman, J. Nogues, and I.K. Schuller, Phys. Rev. B 56, 2332 (1997).

[20]. H. Fujiwara, K. Nishioka, H.C,M.R. Parker, S. Gangopadhyay, and R. Metzger, J. Appl. Phys. 79, 6286 (1996).

[21]. K. Uneyama, M. Tsuchiya, and M. Takahashi, IEEE Trans. Magn. 33, 3685 (1997).

[22]. W. Meiklejohn and C.P. Bean, Phys. Rev. 105, 904 (1957).

[23]. M. Takahashi, A. Yanai, S. Taguchi, and T. Suzuki, Japn. J. Appl. Phys. 19, 1093 (1980).

[24]. K.T.Y. Kung and R.T. Campbell, J. Appl. Phys. 70, 6231 (1991).

[25]. S. Soeya, S. Tadokoro, T. Imagawa, M. Fuyama, and S. Narishige, J. Appl. Phys. 74, 6297 (1993).

[26]. M. Tsunoda, Y. Tsuchiya, M. Konoto, and M. Takahashi, J. Magn. Magn. Mater. 171, 29 (1997).

[27]. K. Takano, R.H. Kodama, A.E. Berkowitz, W. Cao, and G. Thomas, Phys. Rev. Lett. 79, 1878 (1997).

[28]. R. Nakatani, H. Hoshiya, K. Hoshino, and Y. Sugita, J. Magn. Magn. Mater. 173, 321 (1997).

[29]. C.H. Lai, T.C. Anthony, R. Iwamura, and R.L. White, IEEE Trans. Magn. 32, 3419 (1996).

[30]. C.H. Lai, H. Matsuyama, R.L. White, and T.C. Anthony, IEEE Trans. Magn. 31, 2609 (1995).

[31]. C. Leighton, J. Nogues, B.J. Jonsson-Akerman, and I.K. Schuller, Phys. Rev. Lett. 84, 3466 (2000).

[32]. S. Zhang, D.V. Dimitrov, G.C. Hadjipanayis, J.W. Cai, and C.L. Chien, J. Magn. Magn. Mater. 199, 468 (1999).

[33]. J. Nogues and I.K. Schuller, J. Magn. Magn. Mater. 192, 203 (1999).

[34]. Z.L. Zhao, J. Ding, K.Inaba, J.S. Chen, and J.P. Wang, Appl. Phys. Lett. 83, 2196 (2003).

[35]. J.G. Zhu and H.N. Bertram, J. Appl. Phys. 69, 4709 (1991).

[36]. K. O'Grady, M. El-Hilo, and R.W. Chantrell, IEEE Trans. Magn. 29, 2608 (1993).

[37]. Z.L. Zhao, J. Ding, K.Inaba, J.S. Chen, and J.P. Wang, Appl. Phys. Lett. 83, 2196 (2003).

[38]. P.E. Kelly, K. O'Grady, P.I. Mayo, and R.W. Chantrell, IEEE Trans. Magn. 25, 3881 (1989).

[39]. E.P. Wohlfarth, J. Appl. Phys. 29, 595 (1958).

[40]. G.B. Ferguson, K. O'Grady, J. Popplewell, and R.W. Chantrell, IEEE Trans. Magn. 25, 3449 (1989).

[41]. M.M. Chen, C. Tsang, and N. Gharsallah, IEEE Trans. Magn. 29, 4077 (1993).

[42]. R. Jungblut, R. Coehoorn, M.T. Johnson, J.A.D. Stegge, and A. Reinders, J. Appl. Phys. 75, 6659 (1994).

[43]. W.F. Egelhoff, P.J. Chen, C.J. Powell, M.D. Stiles, and R.D. McMichael, J. Appl. Phys. 79, 2491 (1996).

[44]. K.M.H. Lenssen, A.E.M.D. Vierman, and J.T.M. Donkers, J. Appl. Phys. 81, 4915 (1997).

[45]. S.L. Burkett, S. Kora, and J.C. Lusth, IEEE Trans. Magn. 33, 3544 (1997).

[46]. C. Giles, C. Malgrange, J. Goulon, F. Debergevin, C. Vettier, A. Fontaine, E. Dartyge, S. Pizzini, F. Baudelet, and A. Freund, Physica B 209, 784 (1995).

[47]. P.B. Guillemaud, A.K.P. Long, T.C. Anthony, and J.A. Burg, IEEE Trans. Magn. 32, 4627 (1996).

[48]. N. Smith, A.M. Zeltser, D.L. Yang, and P.V. Koeppe, IEEE Trans. Magn. 33, 3385 (1997).

[49]. P. Miltényi, M. Gruyters, G. Güntherodt, J. Nogués, and I.K. Schuller, Phys. Rev. B 59, 3333 (1999).

[50]. S. Gangopadhyay, G.C. Hadjipanayis, C.M. Sorensenfo, and K. Klabunde, Nanostruct. Mater. 1, 449 (1992).

[51]. S. Gangopadhyay and G.C. Hadjipanayis, J. Appl. Phys. 73, 6964 (1993).

[52]. G.H. Wen, R.K. Zheng, K.K. Fung, and X.X. Zhang, J. Magn. Magn. Mater. 270, 407 (2004).

[53]. J.A. Borchers, Y. Ijiri, S.H. Lee, C.F. Majkrzak, G.P. Felcher, R.H.K. Takano, and A.E. Berkowitz, J. Appl. Phys. 83, 7219 (1998).

[54]. M.T. Hutchings and E.J. Samuelsen, Phys. Rev. B 6, 3447 (1972).

[55]. M.J. Carey and A.E. Berkowitz, J. Appl. Phys. 73, 6892 (1993).

[56]. S.S. Lee, D.G. Hwang, C.M. Park, K.A. Lee, and J.R. Rhee, J. Appl. Phys. 81, 5298 (1997).

[57]. Z.Y. Liu and S. Adenwalla, J. Appl. Phys. 93, 2091 (2003).

[58]. M. Fraune, U. Rudiger, G. Guntherodt, S. Cardoso, and P. Freitas, Appl. Phys. Lett. 77, 3815 (2000).

[59]. C.H. Nam, B.K. Cho, and S. Lee, J. Appl. Phys. 93, 6584 (2003).

[60]. G.H. Yu, C.L. Chai, F.W. Zhu, J.M. Xiao, and W.Y. Lai, Appl. Phys. Lett. 78, 1706 (2001).

[61]. M. Fraune, U.R. diger, G. Gutherodt, S. Cardoso, and P. Freitas, Appl. Phys. Lett. 77, 3815 (2000).

[62]. C. Dewitt, B. Dreyfus, and P.D. deGennes, “L. Néel in low Temperature Physics”, Geodon and Breach, New York, p413 (1962).

[63]. J.T. Ricardson and P.R.W.O. Miligan, Phys. Rev. 10, 102 (1956).

[64]. J. Cohen, K.M. Creer, R. Pauthenet, and K. Srivastava, J. Phys. Soc. Japn. 17 (Suppl. B-I), 685 (1962).

[65]. W.J. Schuele and J.A.P.V.D. Deetscreek, J. Appl. Phys. 33, 162 (1962).

[66]. J.T. Richardson, D.I. Yiagas, B. Turk, K. Forster, and M.V. Twigg, J. Appl. Phys. 70, 6977 (1991).

[67]. R.H. Kodama, S.A. Makhlouf, and A.E. Berkowitz, Phys. Rev. Lett. 79, 1393 (1997).

[68]. M. Gruyters, Phys. Rev. Lett. 95, 077204 (2005).

[69]. A. Punnoose and M.S. Seehra, J. Appl. Phys. 91, 7766 (2002).

[70]. L.Y. Zhang, D.S. Xue, and C.X. Gao, J. Magn. Magn. Mater. 267, 111 (2003).

[71]. Y. Köseoğlu, F. Yılsız, G. Salazar-Álvarez, M. Toprak, M. Muhammed, and B. Aktas, Phys. Stat. Sol (b) 242, 1712 (2005).

[72]. S.A. Makhlouf, J. Magn. Magn. Mater. 246, 184 (2002).

[73]. R.H. Kodama, A.E. Berkowitz, J.E.J. MxNiff, and S. Foner, Phys. Rev. Lett. 77, 394 (1996).

[74]. M. Pinarbasi, S. Metin, H. Gill, M. Parker, B. Gurney, M. Carey, and C. Tsang, J. Appl. Phys. 87, 5714 (2000).

[75]. C. Tsang and S.K. Decker, J. Appl. Phys. 52, 2465 (1981).

[76]. S. Parkin, X. Jiang, C. Kaiser, A. Panchula, K. Roche, M. Samant, Proc. IEEE 91, 661 (2003).

[77]. V. Skumaryev, S. Stoyanov, Y. Zhang, G. Hadjipanayis, D. Givord, and J. Nogués, Nature 423, 850 (2003).

Chapter 2

Experimental Techniques

Ni and Co films were deposited using sputtering. Ni/NiO and Co/CoO specimens were prepared by two methods: sputtering under an oxygen partial pressure and the annealing of Co or Ni films in oxygen atmosphere.

2.1 Film Deposition: Sputtering

The sputtering technique is widely used in the research and industry. It allows a wide selection of materials to be sputtered. It produces films of high purity, great adhesion, good uniformity and homogeneity at relatively low cost.

Sputtering is the ejection of surface atoms of a solid by the bombardment of energetic particles such as argon ions. Fig. 2.1 shows a schematic illustration of a sputtering system. The primary construction of a sputtering system consists of substrate holders and targets. The targets are connected to a negative voltage supply, which can be either direct current (DC) or radio frequency (RF). The substrate holder can be grounded, floated, biased or heated. The chamber is kept in a high vacuum using a pump system, which consists of mechanical and turbo pumps. The sputtering gas is normally argon gas or some other inert gas, which has a large atomic mass. However, in some cases, nitrogen or helium gases with light atomic mass are utilized for the deposition. The function of the gas is to provide a medium in which a glow discharge can be initiated and maintained to continuously supply the bombarding particles.

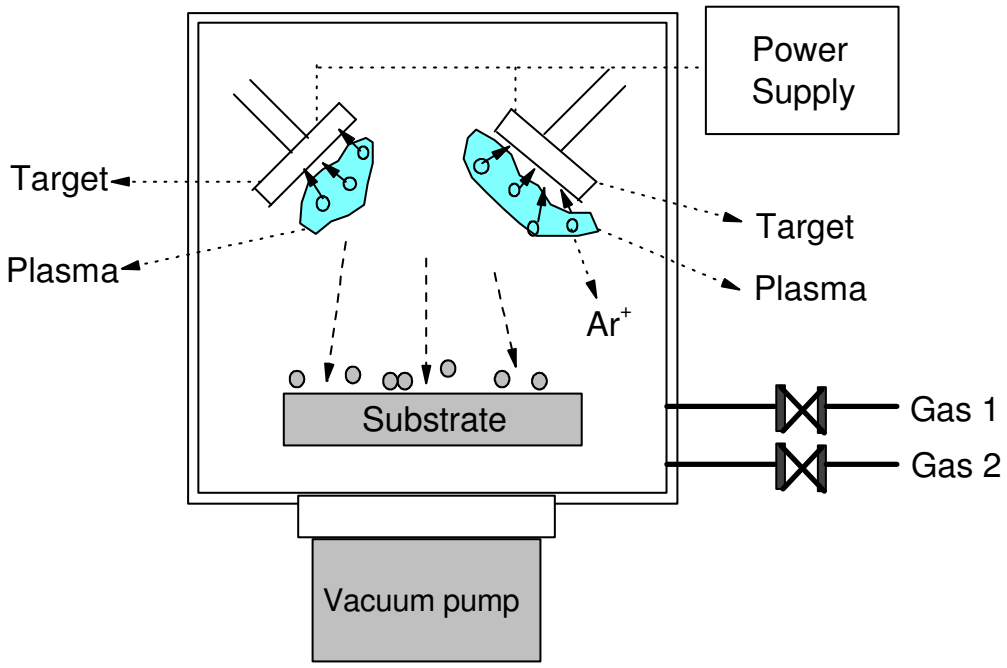

Fig. 2.1 Schematic drawing of a DC sputtering system.

Sputtering is initiated by the application of a negative potential to the target. When the voltage exceeds a threshold value, stable glow discharge appears. In the presence of a negative potential, free electrons are accelerated and ionize the gas atoms. The target, having a negative potential, attracts the positive charged argon ions. Argon ions are accelerated towards the target. The target material is ejected and moves toward the substrate. The potential difference between the substrate and the target must be large enough to allow effective sputtering.

In this thesis, a sputtering system (Discovery 18, Denton, USA) with both magnetron DC and RF sputtering was used for the deposition of thin films. The base vacuum of the system was 2×10^{-6} *torr*. The deposition pressure was approximately 7×10^{-3} *torr*. Ar was used as the ionization gas by a precise control of the flowing rate with a digital

flow meter. A Ni or Co (Good fellow, UK) target with a purity of 99.99 % was used to deposit Ni or Co films on glass substrate. The sputtering power varied from 10 to 200 *W* by adjusting the sputtering voltage and current. Ni/NiO, Co/CoO, NiO and CoO films were obtained by the deposition of Ni or Co films under different oxygen partial pressures. All the films were firstly deposited for a relatively long time (e.g. 3000 *s*). The thickness of the deposited films was measured using a profilometer. Then the deposition rate was obtained when the thickness was divided by the deposition time. In this project, the thickness of the film was controlled by changing the deposition time at a constant deposition rate which was obtained by calibration.

2.2 *X*-ray diffraction (XRD)

A beam of monochromatic *X*-ray will be scattered by the atoms within the crystal when the beam impinges on a crystal, in which the atoms are arranged periodically in three dimensions. The coherently scattered x-rays, having the same frequency and definite phase difference, interfere with one another, constructively or destructively. A diffraction pattern is generated when the scattered rays mutually reinforce one another. The principle of *X*-ray diffraction is governed by the well-known Bragg's law [1].

$$2d \sin\theta = n\lambda \qquad (2.1)$$

Where θ is the angle between the incident *X*-ray and the diffraction plane, d is the interplane (diffraction plane) distance; λ is the wavelength of the incident *X*-ray, and n is an integer corresponding to the order of the diffraction plane.

The above equation relates the diffraction angle (θ) with the crystal structure (d) and the wavelength (λ) of the incident *X*-ray. The unique set of d spacing for a particular material can be found in the powder diffraction files (PDF) complied by the Joint

Committee of Powder Diffraction Standards (JCPDS). For a polycrystalline powdered material, if the individual crystal is less than 100 *nm* in the grain size due to the broadening of equipment, the crystallite size can be estimated using the Scherrer equation:

$$L = \frac{\kappa\lambda}{B\cos\theta} \tag{2.2}$$

where B is the peak width measured at half intensity (radians). κ is the particle shape factor (for spherical particles, κ=0.9) and L is the diameter of the crystallites ($\AA$).

One of the major problems in the determination of the crystallite size from line broadening is to determine value of *B*. Of the many methods proposed, the Warren's method [1, 2] is the simplest:

$$B^2 = B_M^2 - B_S^2 \tag{2.3}$$

where B_M is the measured breadth at half-maximum intensity and B_S is the peak width of the standard material, usually high quality single crystal silicon for the measurement of equipment broadening.

However, when a grain size is smaller than 2.5 *nm*, it is very difficult to obtain the grain size by the above-mentioned method because diffraction effects are diffuse and close to the background noise [3].

In this study, a Bruker D8 ADVANCE *X*-ray diffraction system (XRD) with CuK_α radiation was used for the phase characterization and grain size analysis. Standard θ–2θ scan or glancing angle scan was used to collect XRD spectra. The glancing angle method is surface-sensitive and can avoid the influence of the substrate in the spectrum.

The *X*-ray incident angle is 0.5–2^{o}. The phase was identified using standard powder diffraction files of *JCPDS*. The grain size calculation is based on the XRD profile analysis using the integral broadening method.

2.3 Scanning electron microscopy (SEM)

Scanning electron microscopy (SEM) is normally employed to study the surface morphology and particle/grain size. Electrons from the electron gun are accelerated towards the surface of the sample and the electrons interact with the sample resulting in an ejection of secondary electrons, backscattered electrons, primary electrons and *X*-rays. A detector can collect the number of secondary electrons, backscattered electrons and other radiation signals. The image formed by the collection of secondary electrons reflects the surface roughness. However, the image formed by the collection of backscattered electrons is dependent on the size of the nucleus. Hence, it can indicate the information of the presence of different elements in the samples. The amplified current from the detector by collecting electrons combined with the spot of cathode ray tube (CRT) scanning across the screen can provide the information of sample surface.

In this study, a Philips XL30-FEG-SEM was used to investigate the surface morphology and particle/grain size of the samples. The beam energy was varied from 5 to 30 *keV*. For the electrical conductive samples, e.g. Ni films, the samples were mounted in the sample holder with aluminum tape connected to the sample surface to avoid charging effect. For the NiO films, the samples were coated with approximately 10 *nm* of gold film using a BAL-TEC Sputter Coater SCD005, followed by wrapping aluminum tape on the film surface.

2.4 Energy-dispersive x-ray spectrometer (EDS)

The energy-dispersive *X*-ray spectrometer (EDS) is an attractive tool for a quantitative *X*-ray microanalysis. Each incoming *X*-ray excites a number of electrons into the conduction band of the Is-Li detector leaving an identical number of positively charged holes in the outer electron shells. The energy required for each of the excitations is 3.8 *eV*. Hence, the number of electron-hole pairs generated is proportional to the energy of the *X*-ray photon being detected. The incoming X-ray excited electron to jumb to the coduction band. At the same time, the higher energy shell electron will fall into the holes left by the incoming X-ray excitation. Due the energy different between the high energy shell and low energy shell, X-ray is released. The released energy of the X-ray is only dependent on the atomic structure. Hence, every atom exhibits a characteristic *X*-ray emission spectrum. The fact that a spectrum of interest from 0.1 *keV* to 20 *keV* can be acquired in a relatively short time (10~100 *s*) allows for a rapid evaluation of the specimen. In this study, EDS (Cambridge), which was attached on the SEM system (Philips XL30-FEG), was used for the element analysis. The beam energy was 12 *keV* during measurement. The collecting time was set to be 40 *s*.

2.5 Atomic Force Microscopy (AFM)

Atomic force microscopy (AFM) is one of the most powerful tools for determining the surface topography with a sub-nanometer resolution [4]. It reproduces the image of the sample surface using a sharp tip as a probe which is commonly made from silicon or silicon nitride. The probe is attached to a flexible cantilever with a specific spring constant. The cantilever deflects in the *z*-direction due to the surface topography during tip scanning. A laser reflecting from the surface of the films is traced by a four-

segment-photodiode. The computer processes the electrical differential signal of the photodiode obtained from each point of the surface and generates a feedback signal for a piezo-scanner to maintain a constant force on the tip. This information is then processed into a topographical image.

Three basic measuring modes (contact mode, tapping mode and non-contact mode) are used for the surface analysis. In the tapping mode AFM, the cantilever is oscillated typically with a frequency of 50–500 *Hz*. When the tip is close to the surface, it "taps" the surface which leads to a reduction in oscillation amplitude. This reduction is used to identify and measure topographic features of the surface. In this work, A DI III AFM system was used for the scanning. Tapping mode was used for the surface analysis.

2.6 Raman spectroscopy

Raman Spectroscopy is the inelastic scattering of light. It is a non-destructive technique of probing a material with a visible light source. It was first discovered in 1927 by Sir C.V. Raman and was originally used as a method for the identification of organic solvents and compounds. This was accomplished by recognizing characteristic vibrations that corresponded to the different bonds in the material.

In this study, Raman spectra were obtained with a laser Raman microprobes (Labram HR800, Jobin Yvon Horiba Inc.). The Raman system was optically coupled to an Olympus U-5RE-2 microscope, which provided for both the visual observation of the sample and the collection of backscattered Raman radiation for a small volume at micrometer level. The spectrometer had two interchangeable gratings with 1800 *gr/mm*,

blazed at 500 *nm*, and was equipped with an air-cooled CCD detector (1024×256, 26 microns pixel size, Wright Instruments Inc.) An argon laser with the light wavelength of 514.6 *nm* was used as the excitation source. The spectra were taken at room temperature. The spectra of the samples were acquired at 3 second integration and a step of 0.5 cm^{-1}. The laser power was smaller than 7 *mW* and the slit width of the monochrometor was 500 μm, which corresponded to a resolution of 2.5 cm^{-1}.

2.7 X-ray Photoelectron Spectroscopy (XPS)

Surface analysis by *X*-ray photoelectron spectroscopy (XPS) involves the irradiation of a solid in a vacuum with monoenergentic soft *X*-rays in a vacuum chamber and the analysis of the emitted electrons. These photons have limited penetrating power into a solid on the order of 1–10 nanometers. The photons interact with atoms in the surface region. With the result that the kinetic energy of the electron can be measured as:

$$KE = h\nu - BE - \varphi_s \tag{2.4}$$

where $h\nu$ is the energy of the photons. *BE* is the binding energy of the atomic orbital from which the electron originates and φ_s is the spectrometer work function [5].

The spectrum is obtained by a plot of the number of detected electrons per energy interval versus their kinetic energy. Each element has a characteristic spectrum. The spectrum of a mixture of elements may be considered as the sum of the peaks of the individual constituents. Identification of chemical states can be obtained from an accurate estimation of the separations and peak position, as well as from certain spectral features. In the XPS, the composition of the film can be measured by utilizing the peak area and peak height sensitivity factors.

In this project, surface analysis was performed by XPS (ESCA LAB 220i-XL spectrometer). A *MgKα* (1253.6 *eV*) *X*-ray was used. The total energy resolution was 900 *meV*.

2.8 Transmission electron microscopy (TEM)

The transmission electron microscope is an analytical tool that allows detailed micro-structural examination through high-resolution and high-magnification imaging. It also enables the investigation of crystal structure, orientation and chemical composition, precipitates and contaminants through diffraction pattern, *X*-ray, and electron-energy analysis. In the TEM, three kinds of images can be obtained with different mechanisms of image formation: bright-field, dark-field and high-resolution image.

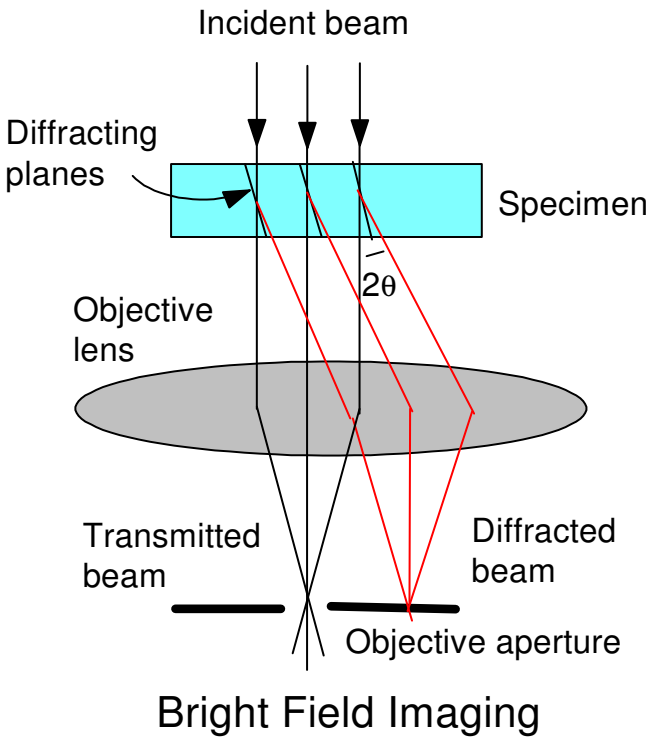

Fig. 2.2 The description of the bright-field imaging.

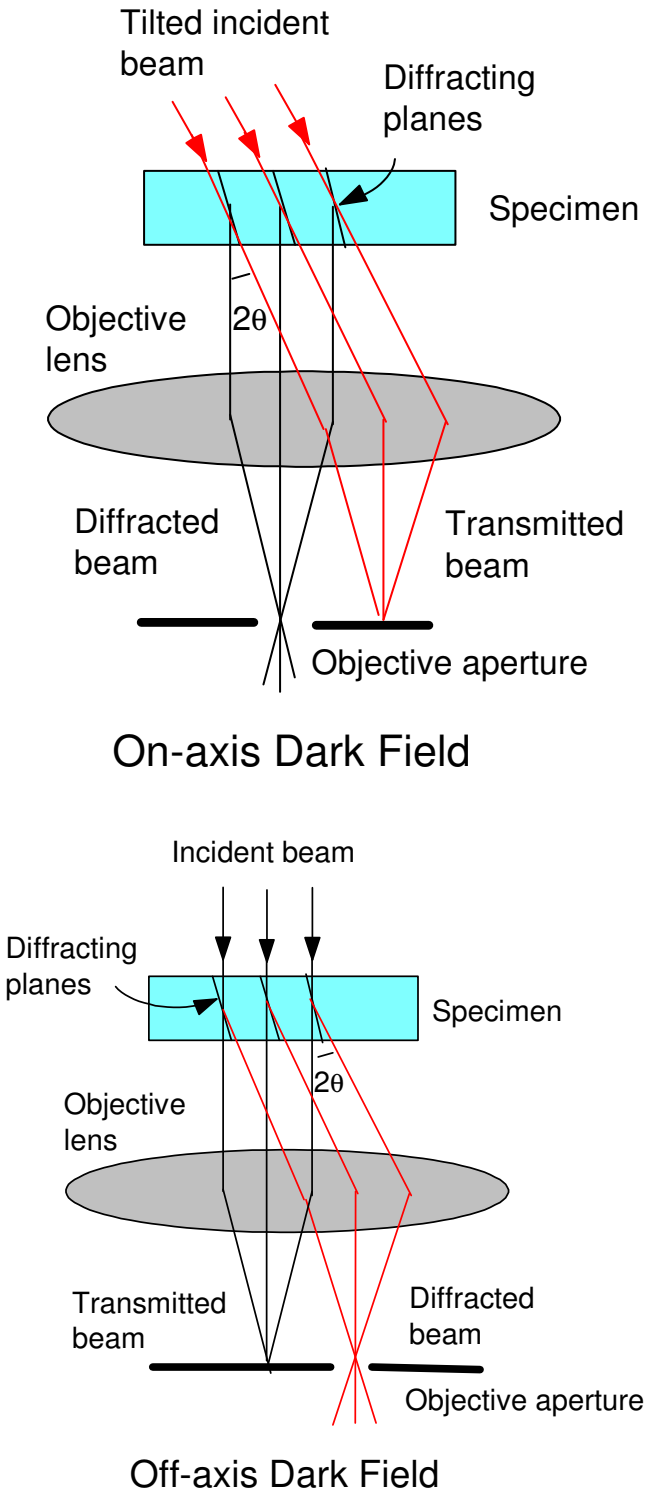

Fig. 2.3 The description of the dark-field imaging.

Dark-field images occur when the objective aperture is positioned off-axis from the transmitted beam in order to allow only a diffracted beam to pass. If a sample is crystalline, many electrons will undergo elastic scattering from the various (*hkl*) planes. This scattering produces many diffracted beams. If any one of these diffracted beams is allowed to pass through the objective aperture, an image can be obtained. This image is known as a dark-field image. Usually, in order to reduce spherical aberration and astigmatism and to improve overall image resolution, the diffracted beam will be deflected so that it lies parallel with the optic axis of the microscope. This type of image is said to on-axis dark-field image, as shown in upper graph of Fig. 2.3. On the contrary, when the image is not formed by the diffraction beam in the optic axis, the image is called off-axis dark-field image, as shown in the lower graph of Fig. 2.3. Dark-field images are particularly useful in examining micro-structural detail in a single crystalline phase. In this work, A JEOL JEM3010 HRTEM was employed to analyze the atomic microstructure and interfaces of deposited films with an accelerated voltage of 300 *keV*.

2.9 Vibrating sample magnetometer (VSM)

The magnetic properties were measured by a vibrating sample magnetometer (VSM). The principle of the measurement by VSM is based on Faraday's law electromagnetic induction, which states that the voltage induced $V(t)$ in an electrical circuit is proportional to the rate of change of magnetic flux linking to the circuit $d\phi/dt$.

$$V(t) = - C.d\phi/dt \qquad (2.5)$$

where C is a constant. A uniform magnetic field is applied on the samples during the measurement. The magnetic field is generated by an electromagnet or a superconducting magnet. The samples are amounted in the middle of the uniform

magnetic field and oscillated by a vibrator, which is a mechanically coupled loudspeaker type velocity transducer. The samples are set to oscillate at low frequencies, e.g. 45 *Hz*. The magnetic flux is detected by means of a set of suitably placed pick-up coils. The amplitude of the coil signal is proportional to the sample magnetization, which is transferred to a magnetic moment by linking to proper electric circuit.

In this study, magnetic properties were measured using the Oxford instrument 3001 vibrating sample magnetometer (VSM) with a maximum field of 90 *kOe* at a temperature in the range of 80–300 *K*. Lakeshore 4500 furnace mounted on the 7300 VSM system was used for the measurement of the Curie temperature, which is higher than room temperature, the magnetic field cooling or magnetic annealing of Ni/NiO and Co/CoO composite. The temperature increasing rate was 1~5 ^{o}C */min.*

2.10 Superconducting quantum interference device (SQUID)

In 1911 H. K. Onnes found superconductivity in certain materials at very low temperatures. The phenomenon was explained successfully by BCS (Bardeen, Cooper and Schrieffer) theory. In 1956 when Cooper explained a process by which two electrons near the Fermi level could couple each other to form an effective new particle, even under a very weak attractive force. This particle was subsequently called the Cooper pair. The superconductivity is due to the Cooper pair transportation in a circuit. If two superconducting regions are kept isolated from each other by a very thin non-superconducting material, there will be a tunneling across the gap. The tunneling of the electron-pairs across the gap carrying a superconducting current was predicted by Josephson [6]. The junction between the two superconductors is called a

"Josephson Junction". A Superconducting Quantum Interference Device (SQUID) uses the properties of electron-pair wave coherence and Josephson Junctions to detect very small magnetic field. The central element of a SQUID is a ring of superconducting material with one or more weak links. Due to the very high sensitivity of the detector of SQUID, it can measure a very small magnetic moment in the range of 10^{-6}–10^{-8} *emu*. The system allows the control of temperature very accurately from 2 to 400 *K*.

In this project, a superconducting quantum interference device (SQUID, MPMS, Quantum design, USA) was used for the magnetic properties measurement. The samples were cut into 5×5 *mm*. A special straw provided by Quantum Design was used for the sample holder. Before measurement, the magnet was reset for eliminating the remnant magnetic field trapped in the superconducting coils. Data were corrected for the magnetism of the sample holder and for the diamagnetic contributions which were measured with the empty holder or holder with substrate but without films on the surface.

2.11 Extended *X*-ray absorption fine structure (EXAFS)

EXAFS refers to the sinusoidal variation of the *X*-ray absorption coefficient as a function of *X*-ray photon energy, which occurs after each absorption edge of an element and extend s for up to 1500 eV further. This phenomenon forms the basis of the analytical technique of EXAFS spectroscopy, which can be used to obtain structural information about molecules without the need for obtaining single crystals.

X-rays can be absorbed by atoms in molecules. Generally, the proportion of *X*-rays absorbed (the absorption coefficient) will decrease as their energy increases, but at certain values of energy, specific to each element, a sudden increase in the amount of

energy absorbed is observed. These energies are known as absorption edges. The energies correspond to the ejection of an electron from the atom in question (*i.e.* ionization). The ejected electron can be considered as a wave, traveling outwards from the central absorbing atom. The increase in absorption at the edge occurs when the energy of the incident *X*-rays is equal to the threshold energy necessary to eject an electron.

Simple models of *X*-ray absorption predict a gradual monotonic decrease in the absorption coefficient with increasing energy away from the absorption edge. Such behavior is observed in spectra of isolated atoms, *e.g.* noble gases (Xe, Kr *e tc.*), but for atoms either in a molecule or a condensed phase, the presence of other atoms around the absorber causes oscillations in the absorption coefficient near the edge. These oscillations in the post edge region arise from the back-scattering of the emitted electron wave off neighboring atoms and so the structure of the post edge region of the *X*-ray absorption spectrum is related to the radial distribution of atoms in the sample. Hence, by analyzing this structure (the frequency and amplitude of the oscillations), information about the local environment of the absorbing element can be derived.

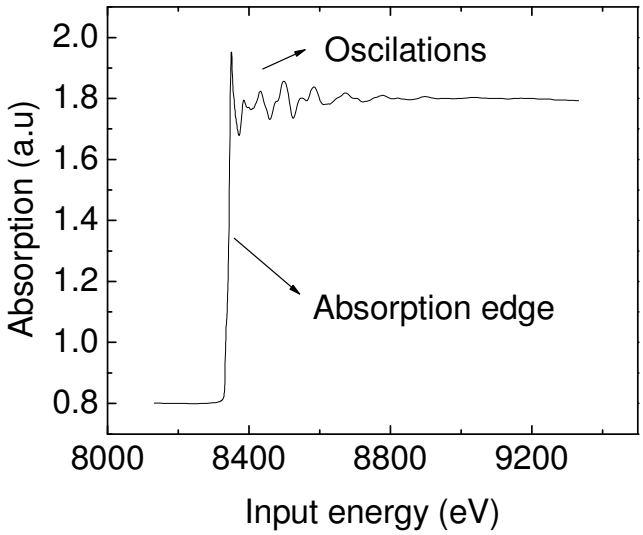

Fig. 2.4 A typical EXAFS spectrum including the absorption edge and ocsilations part.

The EXAFS effect (the oscillations in the post edge absorption coefficient) is small compared to the absorption resulting from the electron ejection (ionization), hence a strong *X*-ray source is required, to produce features sufficiently intense to be analyzed. Synchrotron *X*-ray sources meet this requirement; they produce *X*-ray radiation by accelerating pulses of electrons to a speed approaching that of light, in a circular path of *ca.* 20 metres radius. Because of the complexity of the equipment necessary to achieve this, there are only about 30 such sources in the world. Typically, the *X*-ray beam is divided between different sections, to allow various experiments to run concurrently. The EXAFS experiment involves placing a sample of the compound under investigation in the path of the *X*-ray beam, selecting an absorbing element, and changing the energy of the *X*-rays incident on the sample so that it varies above and below the absorption edge of interest. This variation is done in a series of small steps; at each stage the amount of *X*-rays before and after the sample is measured, so that the amount absorbed by the sample can be determined as a function of energy.

The measurements of the amount of *X*-rays absorbed *versus X*-ray energy are corrected for certain factors such as the general background decrease in the absorption coefficient, to give the observed EXAFS spectrum. A theoretical model is then derived, to match the observed theoretical spectrum as closely as possible. The parameters of the model include the type, number and distance of atoms in the molecule which are close to the absorbing atom under study. Hence, information about the local structure of the molecule can be obtained.

EXAFS spectroscopy differs from diffraction *X*-ray techniques as it is sensitive only to short-range order and can be applied equally well to crystalline or amorphous solids, and also to liquids and even gases. The structure around different elements in the sample can be obtained simply by varying the incident *X*-ray energies to cause ionization of each element in turn. As EXAFS spectroscopy is element-specific, the presence of impurities which either do not contain the absorber, or are far from the absorber, will not cause interference. Sample preparation is quick and data collection relatively easy.

The main deficiencies of the technique are the sensitivity only to short range order (generally to *ca.* 4 Å away from the absorbing element), the lack of three dimensional information, and the large amount of data reduction and analysis involved.

2.12 X-ray Magnetic Circular Dichroism (XMCD)

XMCD is the difference between the absorption spectra of left and right circularly polarized x-rays. XMCD at the p core levels of the 3d metals and at the d core levels of the rare earths, where the dipole transition excites the core electron into the (partially)

localised unoccupied states, provides information about the electronic and magnetic structure. The technique has several advantages compared to its counterparts in the visible region, such as the magneto-optical Kerr effect and the Faraday effect. As the wavefunction of the involved core state is strongly localised and therefore well defined, XMCD is relatively straightforward to analyse and furthermore is element, site and symmetry selective.

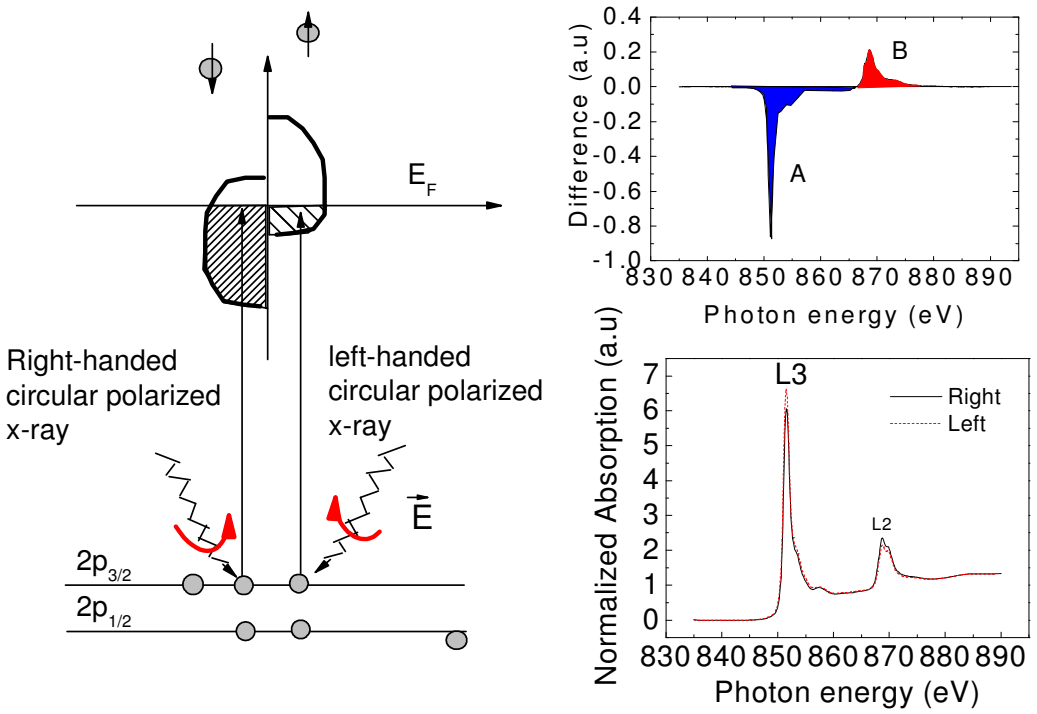

Fig, 2.5. The principles of X-ray magnetic circular dichroism (XMCD).

If there is a net spin moment (imbalance in the spin-up and spin down moments) or a net orbital momentin the valence band electrons, there will be a difference in the absorption spectra between photons of different polarization. The net orbital moment in a 3d magneteic element is induced due to the existence of the spin moment. And is

typically smaller (5-15%) than the spin moment. Areas A and B are obtained by integration the difference spectra (also called the dichroism spectra) of the left and right circular polarized light. The spin and orbital moment can be obtained separately form linear combinations of areas A and B. as seen in this figure. In this example, area A is negative and area B is positive. Hence M_{orb}, is much smaller than M_{spin}.

The experimental proof of X-ray Linear Dichroism (XLD) is given by Van der Laan and B.T. Thole *et al.* [7] in 1986, while the first experiments with circularly polarized x-rays are performed in the high energy range by Schütz and W. Wagner *et al.* [8]. In 1990, Chen and Sette *et al.* measure XMCD in the $L_{2,3}$ edges ($2p \rightarrow 3d$ transitions) of Ni [9] and of Co and Fe [10] and find effects as large as 20 % of the total absorption. For these edges the transitions take place directly to the empty 3d states, which are strongly polarized. A real explosion of the use of XMCD has followed the development of sum rules by Thole and coworkers. [11] These sum rules, applied to the total absorption and XMCD spectra, allow to obtain direct values for the orbital and spin moment of the probed atom.

From the sum rule, the XMCD cannot be quantitively analyzed. In the transition of XAS from 2p→3d, the lz sum rule can be written as:

$$\langle l_z \rangle = -2 \frac{\int d\varepsilon (I_+ - I_-)}{\int d\varepsilon (I_+ + I_- + I_0)} \tag{2.6}$$

where $\langle l_z \rangle$ is the average of the magnetic quantum number of the orbital angular momentum per 3d hole. I_0 is the XAS with the linerarly polarized light whose

polarization vector is parallel to the magnetization. The integration $\int_{j=3/2}(\int_{j=1/2})$ is taken over the whole $2p_{3/2}(2p_{1/2})$ absorption region. The S_z sum rule is written as :

$$\langle S_Z \rangle + \frac{7}{2}\langle t_Z \rangle = -\frac{3}{2}\frac{\int_{j=3/2} d\varepsilon(I_+ - I_-) - 2\int_{j=1/2} d\varepsilon(I_+ - I_-)}{\int d\varepsilon(I_+ + I_- + I_0)} \tag{2.7}$$

where t_Z is the z component of the magnetic dipole operator $t = s - 3r(r \cdot s)/|r|^2$. The integration is taken only over the absorption region. By dividing EQ. (2.6) with Eq. (2.7). We obtain.

$$\frac{\langle l_z \rangle}{\langle S_Z \rangle + \frac{7}{2}\langle t_Z \rangle} = \frac{4}{3}\frac{\int d\varepsilon(I_+ - I_-)}{\int_{j=3/2} d\varepsilon(I_+ - I_-) - 2\int_{j=1/2} d\varepsilon(I_+ - I_-)} \tag{2.8}$$

Normally, for the convenient calculation of the ratio of spin and orbital moment, the equation of the spin and orbital moment can be written as:

$$\mu_l = -\frac{2N_h}{3P\cos\theta}\frac{A_{3/2} + A_{1/2}}{A_d}\mu_B \tag{2.9}$$

$$\mu_s = -\frac{N_h}{P\cos\theta}\frac{A_{3/2} - 2A_{1/2}}{A_d}\mu_B \tag{2.10}$$

$$\frac{\mu_l}{\mu_s} = \frac{A_{3/2} + A_{1/2}}{A_{3/2} - 2A_{1/2}} \tag{2.11}$$

with A_j being the integrated XMCD spectra at the L_{III} (j=3/2) and L_{II} (j=1/2) edges. For the holes of ferromagnet, it can be experimentally measured. Hence the spin and orbital moment can be obtained seperatetly.

2.11 Summary

In this chapter, the procedures for synthesizing nanostructured Ni, NiO, Ni/NiO, Co, and Co/CoO films using sputtering were introduced. A variety of techniques including XRD, SEM, EDX, TEM, AFM, XPS and Raman spectroscopy were employed to investigate the morphology and microstructure of the films. Magnetic properties were taken by VSM and SQUID at different temperatures.

References

[1]. B.D. Cullity, "Elements of X-ray Diffraction", Addison-Wesley, New York, p348 (1978).

[2]. W.T. Sproull, "X-Ray in Practice", McGraw-Hill, New York, p235 (1946).

[3]. L.D. Bianco, A. Hernando, M. Multigner, C. Prados, J.C. Sanchez-Lopez, A. Fernandex, C.F. Conde, and A. Conde, J. Appl. Phys. 84, 2189 (1998).

[4]. F. Fivet, J.P. Lagier, B. Blin, B. Beaudoin, and M. Figlarz, Solid State Ions 32/33, 198 (1989).

[5]. F. John, F.W. Sticle, E.P. Sobol, and D. Kenneth, "Handbook of X-ray Photoelectron Spectroscopy", Physical Electronics, New York, p421 (1989).

[6]. B.D. Josephson. Rev. Mod. Phys. 46, 251 (1974).

[7]. G.van der Laan, B.T. Thole, G.A. Sawatzky, J.B. Goedkoop, J.C. Fuggle, J.M. Esteva, R. Karnatak, J.P. Remeika, H.A. Dabkowska, Phys. Rev. B 34, 6529 (1986).

[8]. G. Schütz, W. Wagner, W. Wilhelm, P. Kienle, R. Zeller, R. Frahm, G. Materlik, Phys. Rev. Lett. 58, 737 (1987).

[9]. C.T. Chen, F. Sette, Y. Ma, S. Modesti, Phys. Rev. B **42**, 7262 (1990).

[10]. F. Sette, C.T. Chen, Y. Ma, S. Modesti, N.V. Smith, "X-Ray Absorption Fine Structure", Ellis Horwood, Chichester, United Kingdom, p966 (1991).

[11]. B.T. Thole, P. Carra, F. Sette, G. van der Laan, Phys. Rev. Lett. **68**, 1943 (1992).

Chapter 3

Structure and Magnetic Properties of Ni Films Prepared by Sputtering

3.1. Introduction

Ni is one of the fundamental elements in magnetic materials. Ni films were widely studied due to their potential applications in the recording media and semiconductor technology [1-3]. Many interesting phenomena were observed in Ni films [4-6].

Today, nickel films can be fabricated by a variety of methods, such as sputtering, MOCVD, MBE, PLD, Electro-deposition, *etc*. Among these methods, sputtering is one of the most commonly used methods for the film growth [7]. The microstructure and properties of thin films prepared by sputtering are strongly influenced by the preparation condition, such as substrate materials, substrate temperature, thickness, and deposition rate [8,9]. In order to the investigate Ni/NiO composite films in this project, Ni films were investigated as the starting work. Structure and magnetic properties of Ni films dependent on the preparation conditions (thickness and annealing temperature) were studied.

3. 2. Experimental procedure

Nickel target (with a purity of 99.97 %) was employed for the fabrication of Ni films using a DC magnetron sputtering system (Discovery 18, Denton). The base pressure was 2.5×10^{-6} *torr* and the work pressure was approximately 7.5×10^{-3} *torr*. Ni films were deposited on glass substrates at room temperature. The film thickness varied from 15 to 400 *nm* controlled by the sputtering time under a variation of deposition powers (10–200 *W*). The annealing process was carried out in a furnace by a flow of mixed gas (95 % Ar+5 % H_2) with a rate of 100 *ml/min*. The annealing was carried out at 500 ^oC for 1h. Film thickness was measured using a surface profilometer (Tencor Instruments) with a vertical resolution of 5 *Å*. A micro-balance with a resolution of 10^{-6} *g* was used

for the estimation of deposited mass by the calculation from the difference between the weight before and after the deposition.

3.3 Characterization and microstructure analysis

3.3.1. Calibration for the thickness and deposition rate

Fig. 3.1a shows the thickness dependence of the films on the sputtering time. The thickness increased linearly with the deposition time, though there was a deviation

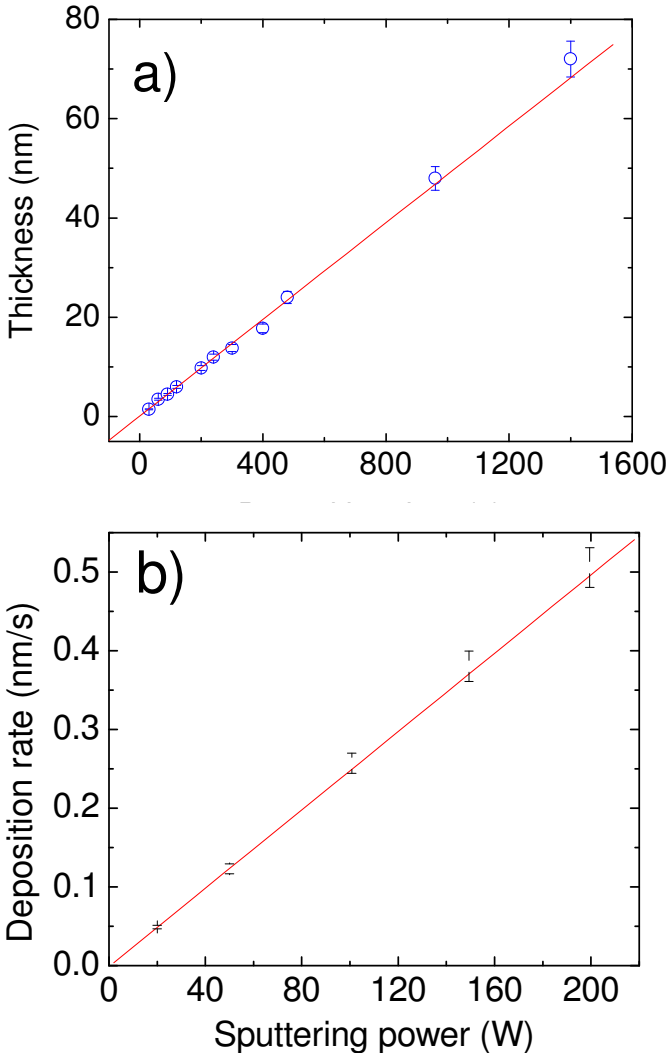

Fig. 3.1. a) Thickness dependence on the sputtering time. The deposition power is 20 W and b) the deposition rate dependence on the sputtering power.

after long time deposition. This may be due to the defects (such as holes or stacking error) of the films for the long time deposition. Fig. 3.1b shows that the sputtering power also has a linear relationship with the deposition rate. The two graphs indicate that it is easy to control the thickness and deposition rate due to their linear relationship.

3.3.2 XRD analysis

Fig. 3.2 shows the *X*-ray diffraction patterns of Ni films with different thicknesses. When the thickness is 15 *nm*, there was only a very weak detectable peak, which corresponds to the (111) peak of *fcc*-Ni. After the film was annealed at 500 ℃, the (111) peak in the spectrum became more pronounced even though the condition of XRD remains unchanged. This result implies the possible presence of disordering

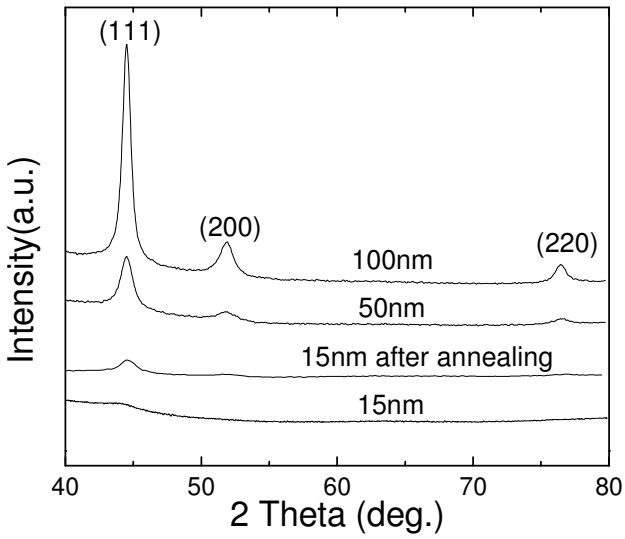

Fig. 3.2. X-ray diffraction spectra of Ni films. a) 15 nm in the as-deposited state; b) 15 nm after annealing at 500 ^{o}C for 1h; c) 50 nm in the as-deposited state and d) 100 nm in the as-deposited state.

(very small grain size and/or amorphous structure). When the thickness was increased to 50 and 100 *nm*, there were three peaks, as expected for the poly-crystalline *fcc*-Ni.

There was no significant change in the XRD spectrum when the two films (50 and 100 *nm*) were annealed at 500 ℃. However, the peaks became sharper, showing a better crystallinity.

3.3.3 TEM analysis

Fig. 3.3 shows the high-resolution TEM micrographs of Ni films with different thicknesses in the as-deposited state**.** In Fig. 3.3a, small Ni crystallites surrounded by areas without lattice pattern were observed. During the HRTEM examination, no lattice pattern could be obtained in these areas. The result indicates the presence of an amorphous structure. When the thickness increased to 50 *nm* (Fig. 3.3b), the amount of amorphous phase was reduced. In a Ni film with a thickness of 100 *nm*, only a small amount of amorphous phase was found in the grain boundaries. Fig. 3.3a shows that the average crystal size is approximately 4 *nm* for the Ni film with a thickness of 15 *nm*. The average crystal size of Ni films with a thickness of 50 and 100 *nm* was approximately 5 *nm*, which was slightly larger than that of the Ni film with a thickness of 15 *nm*.

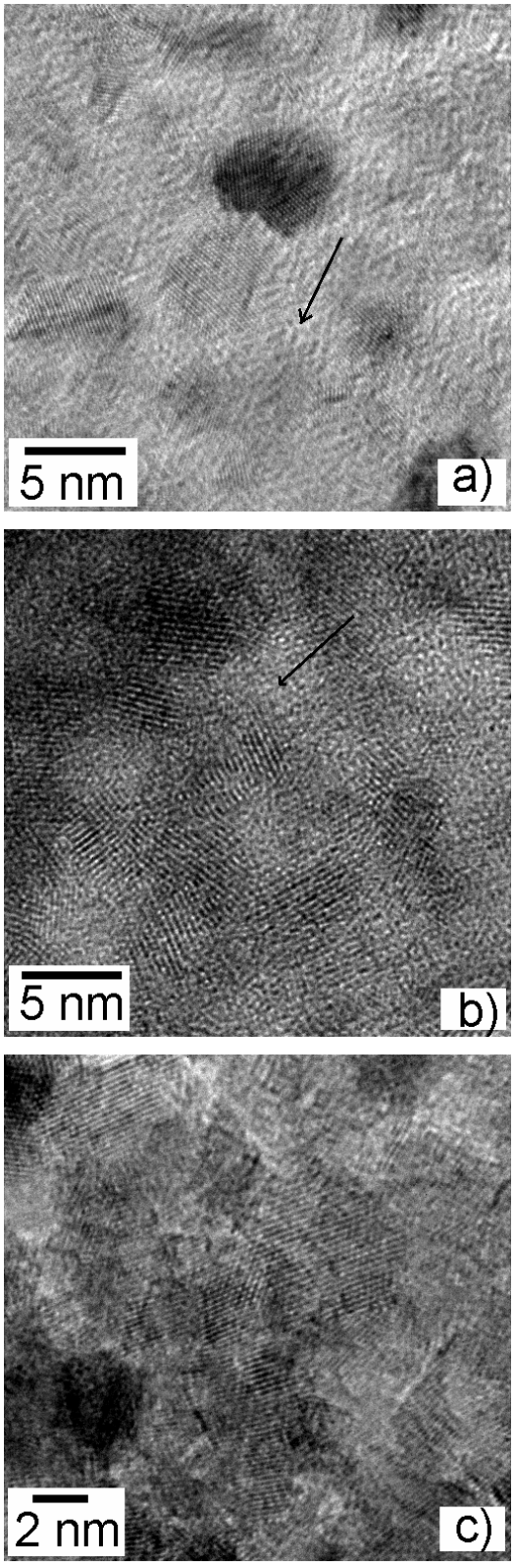

Fig. 3.3. HRTEM micrographs of the as-deposited Ni films with different thicknesses. a) 15 nm; b) 50 nm and c) 100 nm (the arrows indicate amorphous areas).

Fig. 3.4 shows the HRTEM micrographs of the film with a thickness of 15 *nm* after annealing. The microstructure was not uniform, as observed from the image. Large Ni grains (>20 *nm*) were observed as shown in Fig. 3.4a. There were also a large number of circular structures, as shown in Fig. 3.4b. The presence of the circular structure suggests the existence of disordered structure of Ni because when Ni film was deposited with a very low deposition rate or with a substrate temperature of 300 ^{o}C, no such structure can be observed. For thicker films (50 and 100 *nm*), only large grains could be observed (similar to that shown in Fig. 3.4a), supporting that the circular structure is related to the disordered structure. However, the mechanism of the formation of the circular structure in the film with a thickness of 15 *nm* after annealing is not well understood. There is no report on the formation of circular structure. It may be related to large amount of disordered structure. Other factors such as the interaction between the substrate and the film, induced stresses during annealing and/or the formation of islands may all contributed to formation of the structure. Fig. 3.4 c shows the low magnitude image of the film. The grain size is slightly larger than 20 nm, consitstent with that shown in Fig. 3.4 a.

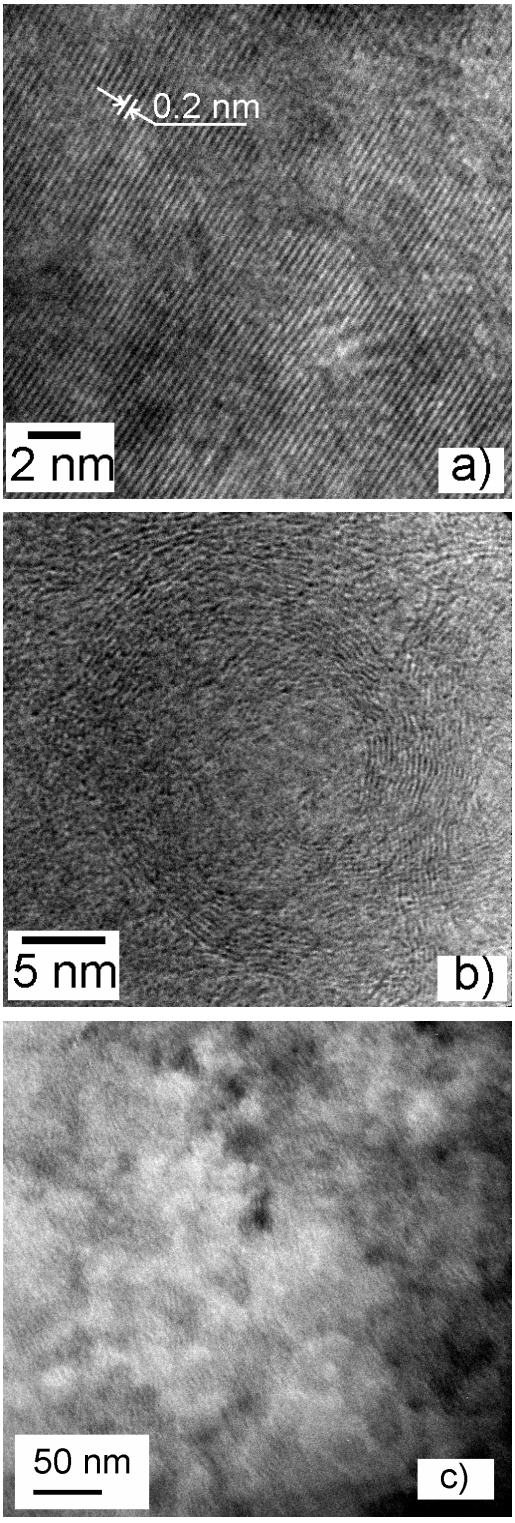

Fig. 3.4. TEM micrographs of the Ni film with a thickness of 15 nm after annealing (the lattice spacing of 0.2 nm indicates an orientation of Ni (111), a) HRTEM image showing large gran size; b) HRTEM showing circular structure; c) low magnitude image.

3.3.4 Coordination number examined by EXAFS

XRD spectra and HRTEM images have shown the presence of disordered structure in the as-deposited Ni films. Extending *X*-ray absorption fine structure (EXAFS) is another effective way to obtain some information of the microstructure [10]. The EXAFS data of Ni films were analyzed using a standard WinXAS 97 procedure [11, 12]. A cubic spline fit was used to remove the non-oscillatory background. The data were then converted into photoelectron wave vector k. The data were then Fourier transformed to real space to obtain radial distribution function by choosing a Gaussian window function. Fig. 3.5 gives the Fourier transformed (FT) amplitudes of the as-deposited and subsequently annealed Ni films with a thickness of 100 *nm*. The coordination number of the as-deposited film was estimated to be 7.1, which is much lower than that of Ni foil, used as a reference (coordination number is 12 for *fcc*-Ni). It should be noted that the magnitude of the first peak depends on both the coordination number N and the disorder about the average distance. The disorder introduces typically a Debye-Waller factor σ^2. Thus, the Debye-Waller factor lowers the signal at large k values. However, the fitting results of the samples showed little difference between the σ^2 values. Hence, the trend of amplitudes can be a good reflection of the coordination numbers. The local environment and the low coordination number of the Ni films support the presence of disordering in the structure [13]. After the annealing of the film at 300 and 500 ℃, the coordination number increased to 9.23 and 10.26 respectively, confirming the increase in crystallinity. The coordination numbers are still lower than that of the standard Ni foil. This may be due to the presence of voids and defects in the films. It should be noted that no sign of oxidation was evident in the EXAFS spectra.

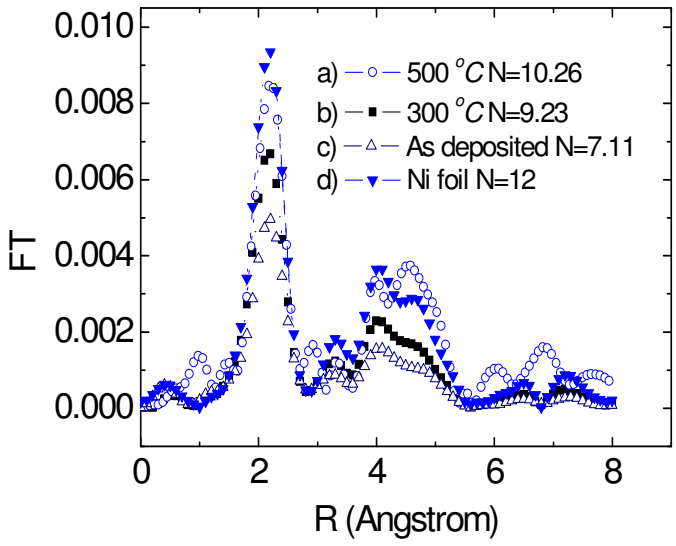

Fig. 3.5. Fourier transformed EXAFS spectra of Ni films before and after annealing.

3.3.5 SEM analysis of the annealed Ni films

Fig. 3.6 shows the SEM images of Ni films with different thicknesses in the as-deposited state. It shows that the films are smooth and uniform. However, when the thickness of the film increases to 100 nm, some small particles can be seen in the SEM image. Fig. 3.7 shows the SEM images of Ni films after annealing at 500 ℃. Islands were formed in the film with a thickness of 15 *nm*. The island size was about 1 *μm*. The Ni film with a thickness of 50 *nm* showed some voids, indicating the initial state of island formation. The formation of islands by annealing may be employed to fabricate patterned films [14]. No formation of islands was observed in the film with a thickness of 100 *nm* after annealing at 500 ℃. However, the surface of the film became rougher and some small porosity could be seen in the SEM image. The particle size was much larger than that in the as-deposited counterpart. One particle consisted of many small grains (the grain size was approximately 20 *nm* from the HRTEM study, as shown in Fig. 3.4).

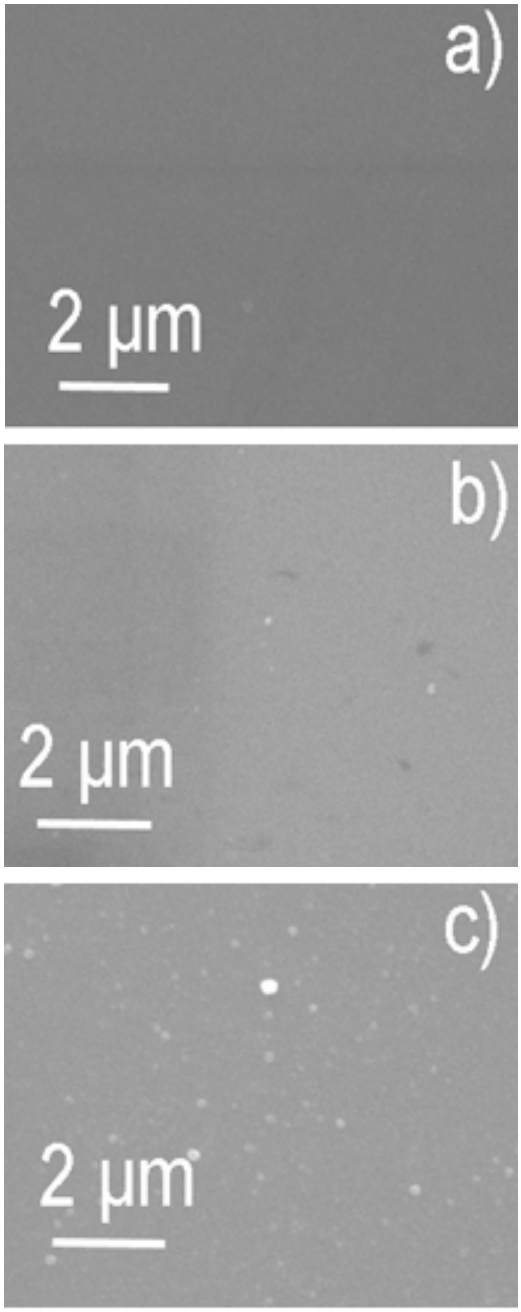

Fig. 3.6. SEM image of the as-deposited Ni films *with a thickness of a) 15 nm; b) 50 nm and c) 100 nm.*

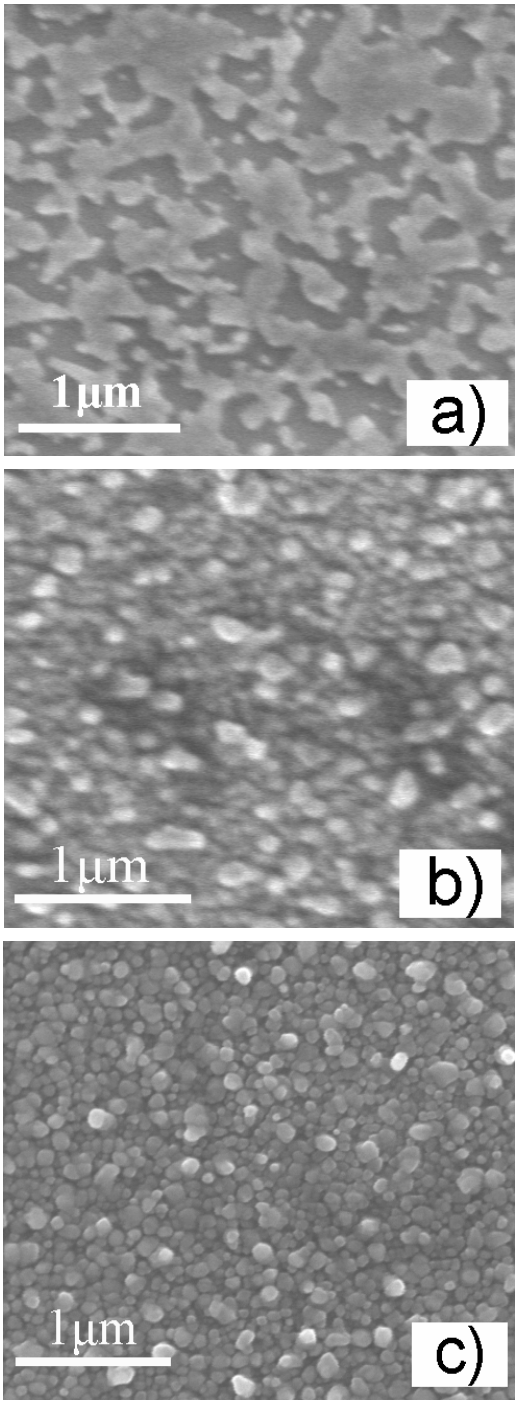

Fig. 3.7. SEM images of the annealed Ni films (500 ^{o}C) with a thickness of a) 15 nm; b) 50 nm and c) 100 nm.

3.4 Magnetic properties

Fig. 3.8 shows the magnetic properties (saturation magnetization M_s and coercivity H_c) of Ni films in the as-deposited and annealed state. The magnetization of the Ni film with a thickness of 15 *nm* in the as-deposited state was very low (24.7 *emu/g*). The value was only approximate 50 % of that of bulk-Ni (54 *emu/g*). The low value of

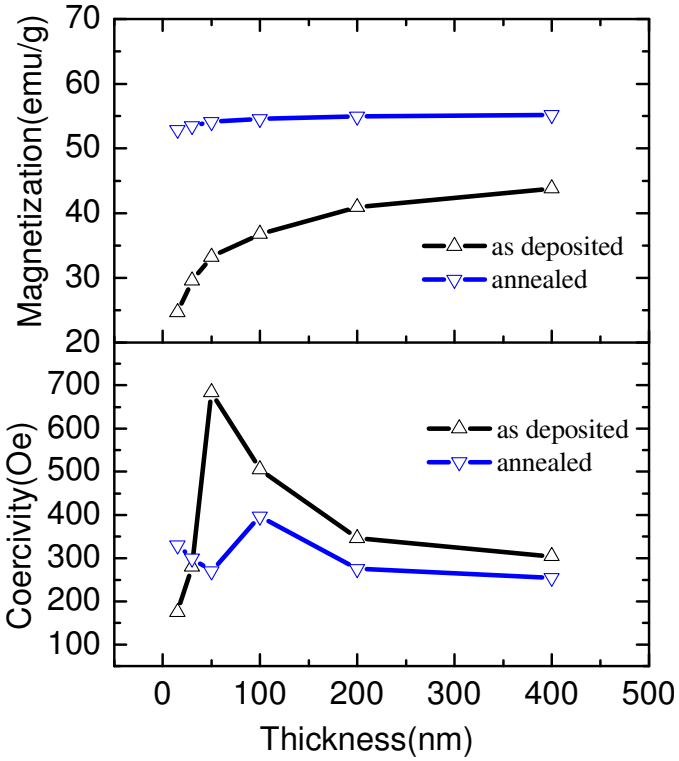

Fig. 3.8. Magnetization and coercivity as a function of the thickness of Ni films before and after annealing.

magnetization was probably due to the disordered structure in the thin films [15, 16]. The saturation magnetization (M_s) increased with increasing thickness. This is because the crystallinity of the thicker films is better, as shown in the XRD and TEM studies (Fig. 3.1 and Fig. 3.2). For the thicker films (100-400 *nm*), the saturation magnetization (34.5–46 *emu/g*) was still below that of bulk Ni. This is probably due to

a certain degree of disordering, as observed in Fig. 3.3c. After the film was annealed at 500 °C, the saturation magnetization was close to that of bulk Ni. The magnetization of a Ni film with a thickness of 15 *nm* was slightly lower than that of the thicker Ni films. This is probably associated with the circular structure, as observed in the TEM study (Fig. 3.4b). Coercivity H_c reached a maximum of 700 *Oe* at 50 *nm* for the as-deposited films (Fig. 3.8). It has been reported [17] that voids and oxidation in the grain boundary may serve as pinning centers for the high coercivity. In this study, the disordered/amorphous structure may play an important role in the high coercivity. The annealed films with different thicknesses showed coercivities in the range of 250–400 *Oe*. The variation of the coercivities is smaller than that of the as-deposited films. The results showed that Ni films in the as-deposited and annealed state had different magnetic properties and different microstructures.

3.5 Resistivity

Fig. 3.9 shows the thickness dependence of electrical resistivity of Ni films in the as-deposited and annealed state. Ni film with a thickness of 15 *nm* in the as-deposited state had a high value of resistivity (35 $\mu\Omega$-*cm*), probably due to the presence of a large amount of disordered structure. Resistivity decreased with increasing the thickness. Ni film with a thickness of 400 *nm* in the as-deposited state had a resistivity of 10 $\mu\Omega$-*cm*. The value is higher than that of bulk Ni (7 $\mu\Omega$-*cm*), suggesting a certain degree of disordering in the film. Certainly, the defects in the film may also affect the resistivity. Ni film with a thickness of 15 *nm* after annealing had a very high resistivity (280 $\mu\Omega$-*cm*). The high resistivity of the film may be due to the formation of islands. For the annealed films with a thickness in the range of 50–400 *nm*, resistivity decreased with increasing the thickness. The curve of resistivity versus thickness can

be relatively well described with the Fuchs-Sondheimer Model [18,19]. The resistivity of the film with a thickness of 400 *nm* was 7.4 $\mu\Omega$-*cm* which was very close to that of bulk Ni, showing a good crystallinity of the film.

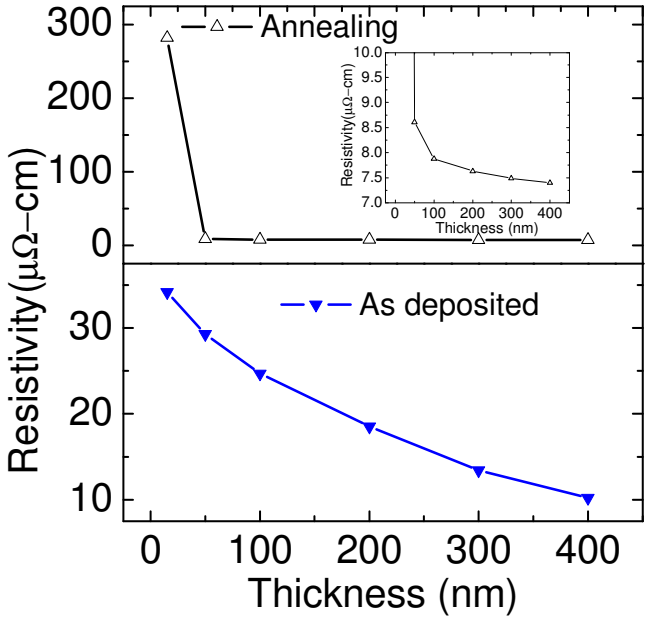

Fig. 3.9. Resistivity as a function of the thickness of Ni films in the as-deposited and annealed state. The inset is the enlargement of annealed samples with a thickness larger than 50 nm.

3.6 Discussion

The above results showed that a high sputtering rate (200 *W*) led to the formation of some amorphous Ni when the film was thin (15 *nm*). When the film thickness was increased to 100 *nm*, a certain amount of amorphous structure still remained. The presence of amorphous structure resulted in a low magnetization. In this work, a separate experiment was performed in order to confirm that the formation of the amorphous Ni was associated with the high sputtering power during deposition.

3.6.1 The effect of substrate and sputtering power on the saturation magnetization of Ni films.

Table 3.1 shows the effect of the sputtering power and substrate on the saturation magnetization of Ni film with a thickness of 100 *nm*. It can be seen that sputtering power affects both the crystallinity and the magnetization. The saturation magnetization increased with decreasing the sputtering power, from 36.7 *emu/g* at 200 *W* to 53 *emu/g* at 20 *W*. It should be noted that the value of 53 *emu/g* is very close to the saturation magnetization of bulk Ni (54 *emu/g*). XRD study also confirmed that a low sputtering power benefited film crystallinity. The microstructure of Ni films deposited with 20 *W* is shown in Fig. 3.10, indicating a fully crystalline structure.

Table 3.1. The dependence of saturation magnetization (M_s) of Ni films with a thickness of 100 nm on sputtering power and substrate.

Sputtering power (*W*)	**Substrate**	**Ms (*emu/g*)**
20	glass	53
40	glass	52.3
100	glass	41.9
200	glass	36.7
200	quartz	41.4
200	silicon	42.4
200	copper	50.1

On the other hand, it can be seen from the table that the materials of the substrate also play an important role in the crystallinity of Ni films. Under the same condition (sputtering power: 200 *W* and thickness: 100 *nm*), the saturation magnetization of Ni films on the substrate of quartz and silicon wafer was higher than that of a Ni film deposited on glass substrate. When Cu foil was used as the substrate, the saturation magnetization of a Ni film reaches 50.1 *emu/g*, which was not far below the expected

value of bulk Ni. These results indicate that the crystallinity of a Ni film can be strongly affected by the substrate. The high saturation magnetization of a Ni film deposited on Cu substrate was probably due to the similarity in the structure of *fcc*-Cu and *fcc*-Ni. In addition, their lattice parameters are close to each other

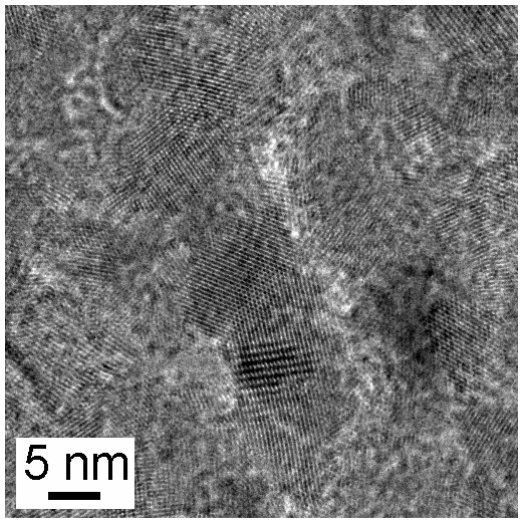

Fig. 3.10. TEM micrograph of a Ni film with a thickness of 100 nm deposited with a power of 20 W.

3.6.2 XMCD analysis

X-ray magnetic circular dichroism (XMCD) has been extensively used for the measurement of magnetic moment of ferromagnetic materials [20-25]. In this study, XMCD and *X*-ray absorption spectra (XAS) experiments were carried out. The magnetic moment of the as-deposited Ni film (15 *nm*) was measured by XMCD at room temperature. A standard poly-Ni foil (Goodfellow, UK) was measured as a reference. Fig. 3.11 shows the XMCD spectra of the as-deposited Ni film and Ni foil.

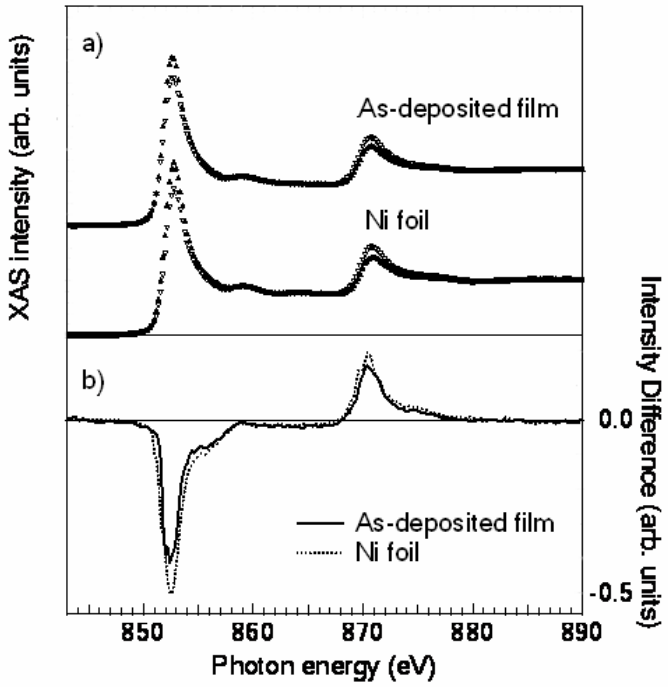

Fig. 3.11. a) Ni L edge X-ray absorption spectra for the as-deposited Ni film and standard polycrystalline Ni foil, respectively. Spectra for both magnetizations are represented by different triangles: Parallel (solid triangles) and antiparallel (open triangles) alignment of photon spins and sample magnetization directions; b) dichroism spectra calculated from a) the intensity difference shown by solid lines for Ni foil and dashed lines for the as-deposited Ni, respectively.

Before the XMCD measurement, the sample was etched with Ar ion sputtering and fully magnetized by a magnetic coil to produce a magnetic field parallet ot the film plane. The dichroism spectroscopy was then obtained by reversing either the helicity of the circularly polarized light or the magnetization direction. The results showed that the total magnetic moment of Ni foil was about 0.6 μ_B as expected in the reference of Ni foil [26]. The total magnetic moment of the as-deposited film was about 20 % lower than that of the Ni foil, confirming the low magnetization in the as-deposited films.

3.7. Summary

Ni films with different thicknesses have been prepared by magnetron sputtering. XRD, HRTEM and EXAFS studies revealed that there was a large amount of amorphous structure in the Ni films with a thickness of 15 *nm* in the as-deposited state. Crystallinity increased with increasing the film thickness. The as-deposited Ni film consisted of very small Ni grains (4–5 *nm*). After annealing (500 °*C*), large grains (20 *nm*) were observed. For a Ni film with a thickness of 15 *nm*, island formation was observed and some circular structure was evident under HRTEM. The formation of the circular structure needs further investigation. Samples with a large amount of amorphous structure showed a very low saturation magnetization (compared with bulk Ni). There is no evidence to show that the film was partially oxidized. Hence the amorphous structure was attributed to the low saturation. The saturation magnetization increased with increasing the film thickness due to the better crystallinity of the thicker films. Large resistivity was observed in the as-deposited films. After annealing at 500 °*C*, an increase in the saturation magnetization and a decrease in the resistivity were observed. The saturation magnetization and resistivity of the thick films (100–400 *nm*) were very close to those of bulk-Ni. All the results showed that amorphous Ni phase led to the low magnetization and high resistivity. The large amount of amorphous structure resulted from the high deposition rate. Low sputtering rate led to good crystallinity of the films. In addition, the thickness of the film also affected the film crystallinity. Therefore, the microstructure, magnetization, crystallinity of the Ni films using sputtering can be tuned by adjusting the deposition parameters.

References

[1]. J.F. Greff, I. Petej, E. Jouguelet, and C. Dennis, J. Phys. D-Appl. Phys. 35, R121 (2002).

[2]. D.K. Sarkar, M. Falke, H. Giesler, S. Teichert, G. Beddies, and H.J. Hinneberg, Appl. Phys. A-Mater. Sci. Proc. 70, 681 (2000).

[3]. P.S. Lee, K.L. Pey, D. Mangelinck, J. Ding, D.Z. Chi, T. Osipowicz, J.Y. Dai, and L. Chan, J. Electrochem. Soc. 149, G505 (2002).

[4]. S.A. Haque, A. Matsuo, Y. Seino, Y. Yamamoto, S. Yamada, and H. Hori, Physica B 305, 121 (2001).

[5]. I. Rhee and K.I. Chan, IEEE Trans. Magn. 37, 1032 (2001).

[6]. C. Prados, D.V. Dimitrov, G.C. Hadjipanayis, and A. Hernando, J. Magn. Magn. Mater. 177, 1293 (1998).

[7]. O. Kohmoto, N. Mineji, Y. Isagawa, and O. Kubo, J. Magn. Magn. Mater. 239, 36 (2002).

[8]. T.T. Kawabat, K. Kitabatake, A. Yamada, K. Mikami, Y.H. Kajioka, and K. Toiyama, J. Vac. Sci. Technol. A 19 (2001).

[9]. T. Zeng and H.K. Wong, J. Appl. Phys. 79, 6279 (1996).

[10]. J.C. Yang, Y.G. Shul, C. Louis, and M. Che, Catal. Today 44, 315 (1998).

[11]. S.I. Zabinsky, J.J. Rehr, A. Ankudinov, R.C. Albers, and M.J. Eller, Phys. Rev. B 52, 2995 (1995).

[12]. T. Ressler, M. Hagelstein, U. Hatje, and W.T. Metz, J. Phyique, IV 7, 731 (1997).

[13]. C.J. Sun, G.M. Chow, J.P. Wang, E.W. Soo, Y.K. Hwu, J.H. Je, T.S. Cho, H.H. Lee, and D.Y. Noh, J. Appl. Phys. 91, 7182 (2002).

[14]. H. Yukihiro, Y. Motoki, I. Hiroya, Z. Shigeaki, and Y. Yukio, Sur. Sci. 38, 116 (1999).

[15]. W.Y. Ching, L.W. Song, and S.S. Jaswal, Phys. Rev. B 30, 544 (1984).

[16]. K. Tamura and H. Endo, Phys. Lett. 29A, 52 (1969).

[17]. M.S. Miller, F.E. Stageberg, Y.M. Chow, K. Rook, and L.A. Heuer, J. Appl. Phys. 75, 10 (1994).

[18]. K. Fuchs, Pro. Camb. Phil. Soc. 34, 100 (1938).

[19]. E.H. Sondheimer, Adv. Phys. 1, 1 (1952).

[20]. P. Carra, B.T. Thole, M. Altarelli, and X.D. Wang, Phys. Rev. Lett. 70, 694 (1993).

[21]. W.J. Antel Jr., T. Hushes, H. Laidler, P.J. Doherty, and A. Johnston, J. Magn. Magn. Mater. 242-245, 961 (2002).

[22]. G. van der Laan, Phys. Rev. Lett. 82, 640 (1999).

[23]. C.T. Chen, Y.U. Idzerda, H.J. Lin, N.V. Smith, G. Meigs, E. Chaban, G.H. Ho, E. Pellegrin, and F. Sette, Phys. Rev. Lett. 75, 152 (1995).

[24]. B.T. Thole, P. Carra, F. Sette, and G. van der Laan, Phys. Rev. Lett. 68, 1943 (1992).

[25]. J. Stöhr, J. Electron Spectrosc.Relat. Phenom. 75, 253 (1995).

[26]. T. Jo and G.A. Sawatzky, Phys. Rev. B 43, 8771 (1991).

Chapter 4

Magnetism Evolution of NiO in the Amorphous, Cluster and Nanocrystalline States

4.1 Introduction

Recently, NiO have attracted much interest due to its potential applications as components for the spin valves and spin devices. This is because that NiO has a relatively high Néel temperature (520 *K*) and good chemical stability [1.2]. In addition, NiO has simple rock salt structure, as discussed in Chapter 1. The simple structure provides advantages for the basic researches in the spin related phenomena. In this chapter, the magnetism of amorphous, cluster, nanocrytalline and well crystalline NiO is investigated in detail.

4.2 Experimental procedure

NiO nano-powders were prepared by annealing nickel hydroxide precursor, which was derived from co-precipitation of Ni_2SO_4 (0.2 *M*) and NaOH (0.5 *M*) solutions. The nickel hydroxide precursor was washed with de-ionized water. The precipitates were then rinsed with anhydrous ethanol several times to remove most of the water. The precursor was dried at room temperature after centrifuging, followed by an annealing at 170－900 ℃ for one hour in air. As the precipitation method could not deliver uniform amorphous NiO powders because of the existence of $Ni(OH)_2$, sputtering was used for the fabrication of the uniform amorphous NiO sample. NiO film was deposited on glass substrate by DC magnetron sputtering using a Ni target (Good fellow, UK) with a purity of 99.99 %. During sputtering, an oxygen partial pressure of 1.4×10^{-3} *torr* was introduced.

4.3 Synthesis and analysis of amorphous, cluster and nanocrystalline specimens

4.3.1 Synthesis of fully amorphous nickel oxide by sputtering

There are two methods in the preparation of amorphous nickel oxide films using sputtering technique. The first method involves the sintered nickel oxide target being directly used for the sputtering. The second method involves the use of the metallic Ni target for the sputtering under an oxygen partial pressure (reactive sputtering). It was found that nickel oxide films, prepared from a sintered nickel oxide target, did not possess an amorphous structure using the existing sputtering system. Hence, in this work, nickel oxide films were deposited under an oxygen partial pressure using a Ni target (the deposition power was 20 *W*). Fig. 4.1 shows the XRD spectra of Ni films deposited with and without an oxygen partial pressure of 1.4×10^{-3} *torr*. Pure Ni film

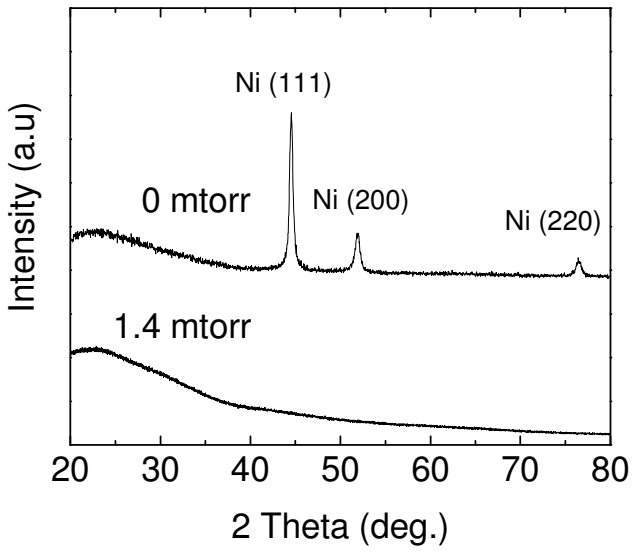

Fig. 4.1 XRD spectra of Ni and nickel oxide films prepared by sputtering under an oxygen partial pressure of 0 and 1.4×10^{-3} torr, respectively.

with three peaks was seen when the film was deposited without an oxygen partial pressure. When an oxygen partial pressure of 1.4×10^{-3} *torr* was introduced during the

deposition, there were no observable peaks of Ni or nickel oxide in the XRD spectrum. A wide hump in the range of 20–40 degree suggests an amorphous structure of the film.

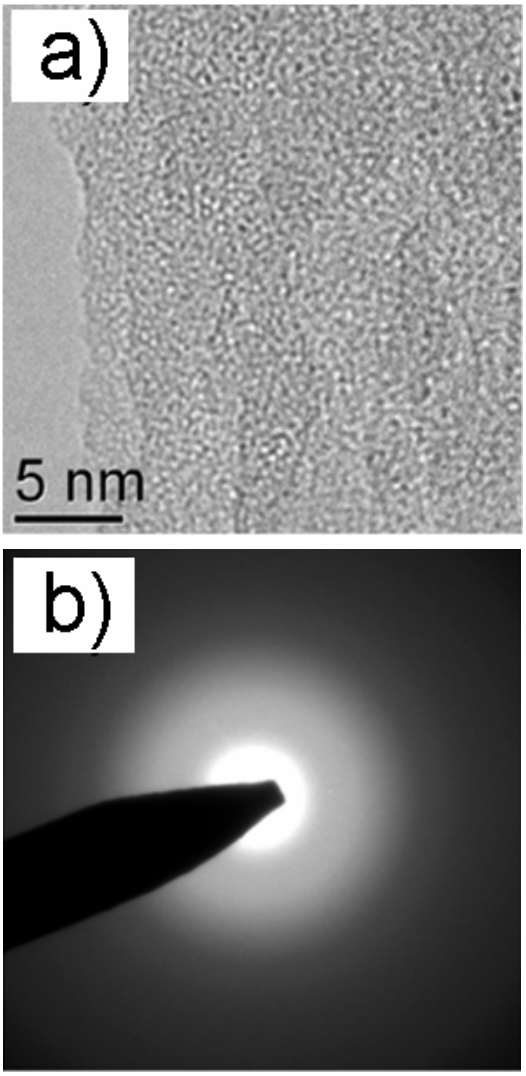

Fig. 4.2 a) HRTEM micrograph of a nickel oxide film deposited under an oxygen partial pressure of 1.4 ×10^{-3} torr and b) the SAED of the film.

Fig. 4.2 shows a high resolution TEM micrograph of a nickel oxide film deposited by sputtering under an oxygen partial pressure of 1.4 ×10^{-3} *torr*. The film was a fully amorphous structure as no grains or crystalline lattice could be found. During the

examination, the sample was carefully tilted and focused. The electron diffraction pattern also showed an amorphous structure of the film (Fig. 4.2b). From the analysis of XRD and HRTEM, it may be concluded that fully amorphous nickel oxide films can be fabricated by sputtering using a Ni target under an oxygen partial pressure of 1.4 $\times 10^{-3}$ *torr*.

4.3.2 Synthesis of nickel oxide in the cluster and nanocrystalline structures (co-precipitation and subsequent annealing)

In the subchapter 4.3.1, fully amorphous nickel oxide has been prepared by sputtering. However, the recrystallization through the annealing of the amorphous NiO resulted in relatively large grains. Therefore, the combination of co-precipitation and subsequent annealing was used in the synthesis of nickel oxide clusters and nanocrystalline nickel oxide particles with different particle sizes.

4.3.2.1 Thermal gravitation analysis (TGA)

After the co-precipitation, the powders were dried in air. The dried powders were then annealed at a temperature of 100－900 ^{o}C. Thermal gravitation (TG) was used for the examination of the precursor and annealed powders. The TG curves are shown in Fig. 4.3. For the as-prepared powders, there were two steps in the TG curve. The first one appeared below 100 ℃, probably due to the evaporation of physically absorbed water. The second step appeared at 150-200 ℃, which was probably attributed to the decomposition of $Ni(OH)_2$. The water content in $Ni(OH)_2 = NiO + H_2O$ corresponded to 19.5 *wt%* of water. The weight loss of the sample was approximately 20 *wt%* in the temperature range of 100 to 300 ℃, agreeing well with the proposed decomposition. The result indicates that the as-prepared sample has a composition of $Ni(OH)_2$ plus a

large quantity of physically absorbed water. Under the heat rate of 10 ℃*/min* (during the TGA measurement), the decomposition occurred in the temperature range of 150–200 ℃.

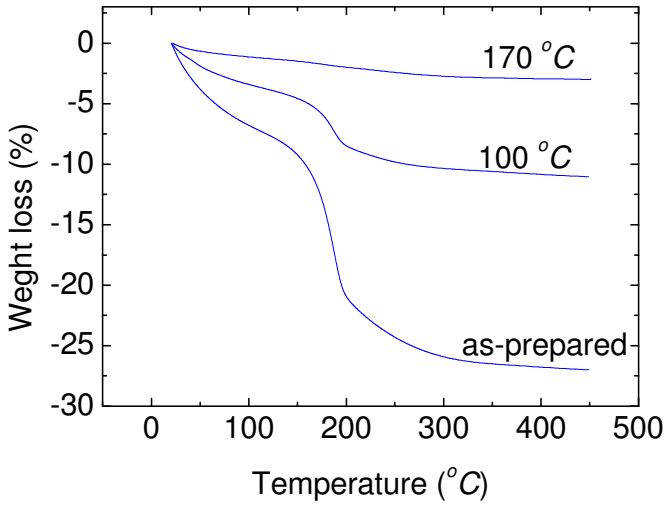

Fig. 4.3. TGA curves of NiO powders of a) as-prepared; b) annealed at 100 ^oC and c) annealed at 170 ^oC.

For the sample annealed at 100 ℃ (Fig. 4.3), there was still some water. Except the physically absorbed water, the second step was reduced to approximately 5 *wt %*. The result indicates that decomposition has occured during the heat treatment at 100 ℃, but the decomposition cannot be completed at this temperature. After annealing at 170 ℃, TGA showed that the amount of the residual water was very small. The composition of the powder was expected to be NiO when the powder was annealed at 170 ^oC or above. Therefore, in this study, the powders annealed at 170 ℃ or higher have been used as NiO cluster and well-crystalline samples for the magnetic investigation.

4.3.2.2 XRD analysis

Fig. 4.4 shows the XRD spectra of NiO powders annealed at different temperatures for 30 *min*. No peaks could be observed in the powder annealed at 170 ^{o}C. After the powder was annealed at 300 ^{o}C, several peaks appeared. The peaks could be indexed to the different crystallographic planes of *fcc*-NiO. When the annealing temperature was higher, the peaks became sharper, indicating an increase in the crystallinity. No other phases could be found in the XRD analysis. Using the Scherrer equation (Equation. 2.2 in Chapter 2), the grain size can be calculated according to the XRD spectra as shown in Fig. 4.5. The instrumental line-broadening was deducted before the calculation (0.1^{o}). The calculated results are shown in the Fig. 4.5. The grain sizes increased from 3.5 *nm* to ~50 *nm* after the powders annealed from 300 to 900 ^{o}C. The results indicate that the grain size and crystallinity increase with increasing annealing temperature.

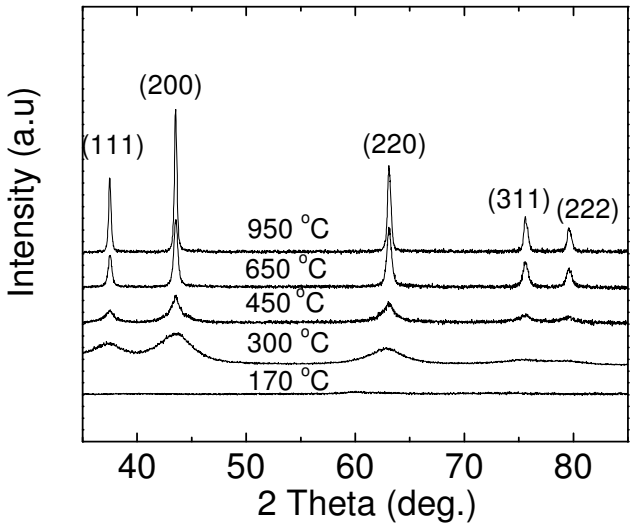

Fig. 4.4. XRD spectra of co-precipitated NiO powders annealed at different temperatures.

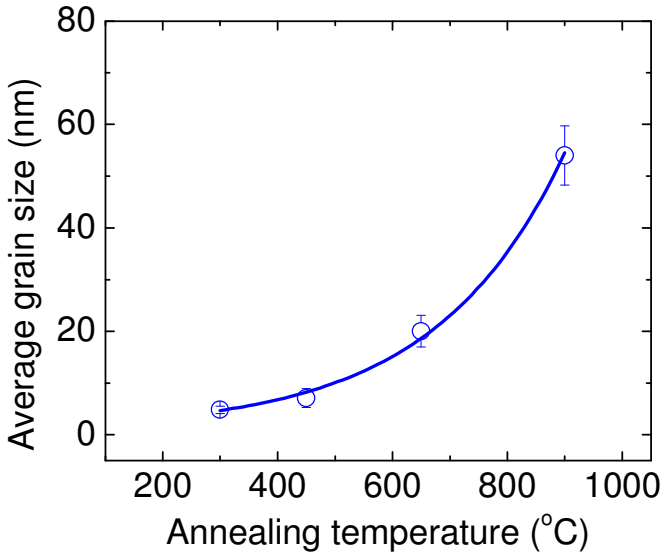

Fig. 4.5. Grain size dependence of NiO powders on the annealing temperatures. The grain size is calculated by Scherrer equation. The line is a guide to eyes.

4.3.2.3 Structural analysis by TEM

It is shown previously that no XRD peaks of were observable for nickel oxide powders. However, the structure under the high-resolution TEM was not uniform as shown by the non-uniform contrast and some crystalline lattices (Fig. 4.6a). The dark-field image (Fig. 4.6b) showed small NiO clusters with a cluster size in the order of 1 *nm*. No diffraction rings can be observed in the selected area diffraction pattern (Fig. 4.6c).

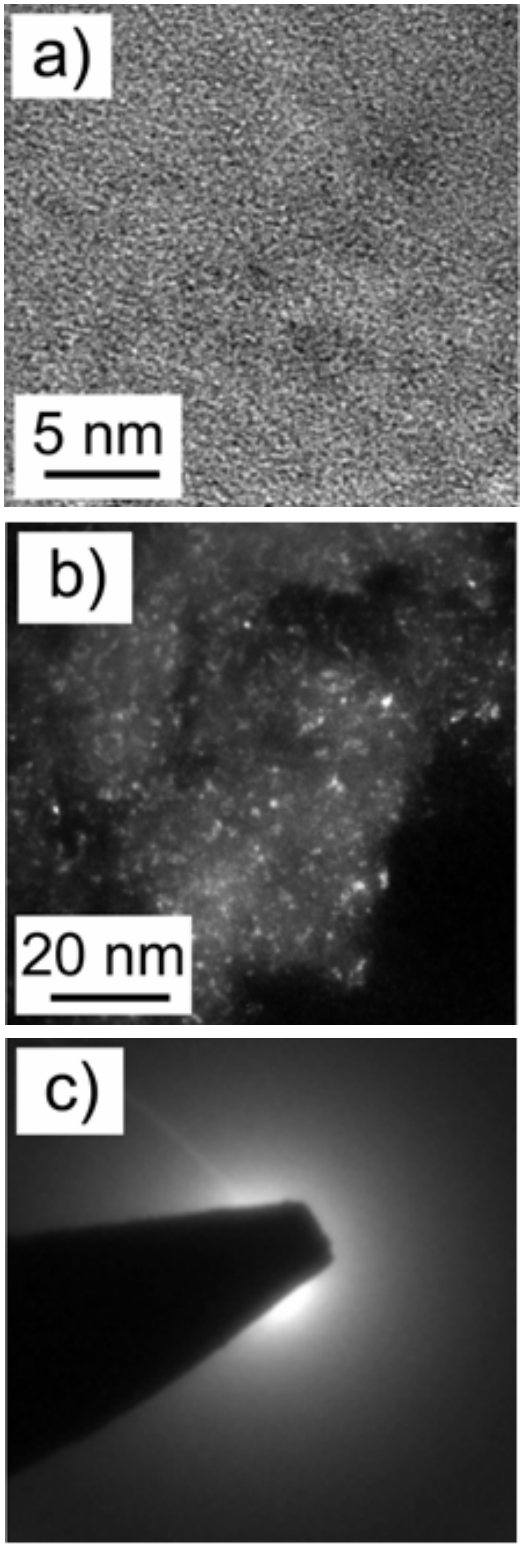

Fig. 4.6. TEM micrographs of a) bright-field image and b) dark-field image of the NiO powder annealed at 170 ^{o}C; c) selected area electron diffraction (SAED) pattern of the powder.

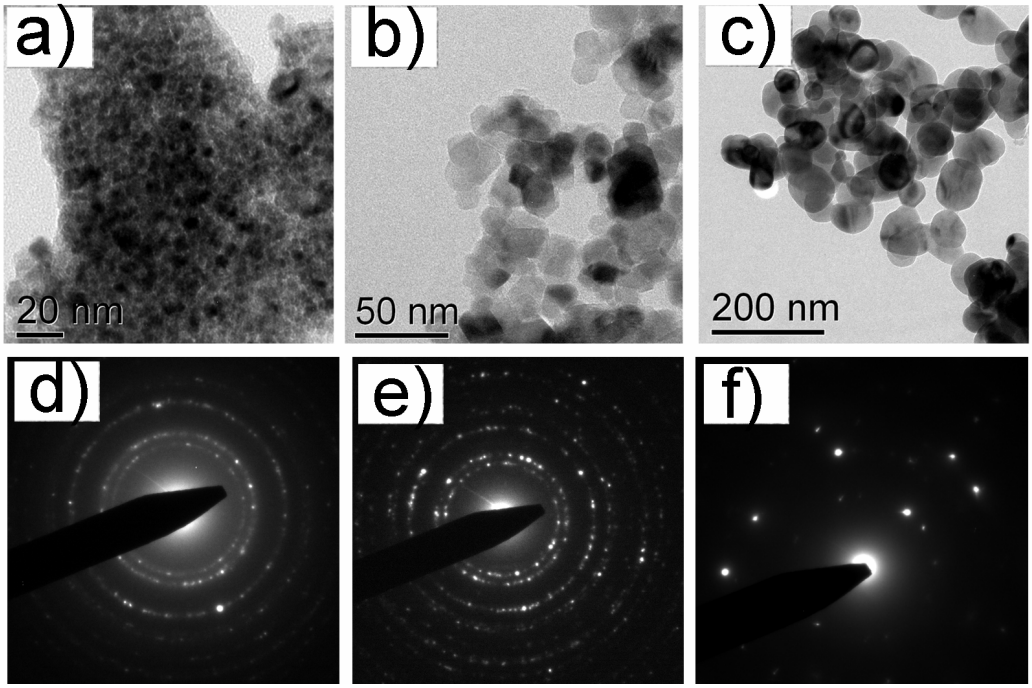

Fig. 4.7. Bright-field TEM micrographs of NiO powders annealed at a) 300 ^{o}C; b) 650 ^{o}C; c) 900 ^{o}C; d),e) and f) are the SAED patterns of a), b) and c), respectively.

Well crystalline NiO nanocrystals were observed in NiO samples annealed at 300 ℃ or above, as shown in Fig. 4.7. The crystal size increased with increasing the annealing temperature. The average grain size of the NiO powder annealed at 300 ^{o}C was 3–5 *nm*. It increased to around 18 and 50 *nm* when the annealing temperature increased to 650 and 900 ^{o}C respectively, as shown in Fig. 4.7b and c. The selected area electron diffraction (SAED) patterns of the corresponding NiO powders are shown in Fig. 4.7d, e and f. The patterns demonstrated that the crystallinity increased with increasing annealing temperature. It should be noted that only the NiO phase could be identified from the analysis of the electron diffraction patterns.

4.4 Maximum magnetization of NiO with different microstructures (amorphous, cluster and nanocrystalline)

NiO bulk is an antiferromagnet with a Néel temperature of 520 *K* [3]. NiO has been widely used as the pinning layer in spin valves and other spintronic devices [4-7]. However, the magnetic properties of nanostructured NiO have not been well understood. Therefore, it is interesting to investigate the magnetic properties of the NiO in the states of amorphous, cluster and nanocrystalline structures. Fig. 4.8 shows the maximum magnetization of the NiO film derived from sputtering (fully amorphous) and the powders derived from co-precipitation method after annealing at different temperatures (the largest applied magnetic field was 50 *kOe* and the hysteresis loops were taken at 2 *K*). From the graph, amorphous NiO deposited by sputtering showed a zero magnetization. For the NiO powders, there was a dramatical increase in magnetization when the powders were annealed at 150–200 ^{o}C. A maximum magnetization of 105 *emu/g* was achieved when the powder was annealed at 170 ^{o}C. A further increase in the annealing temperature led to a drastic decrease in magnetization.

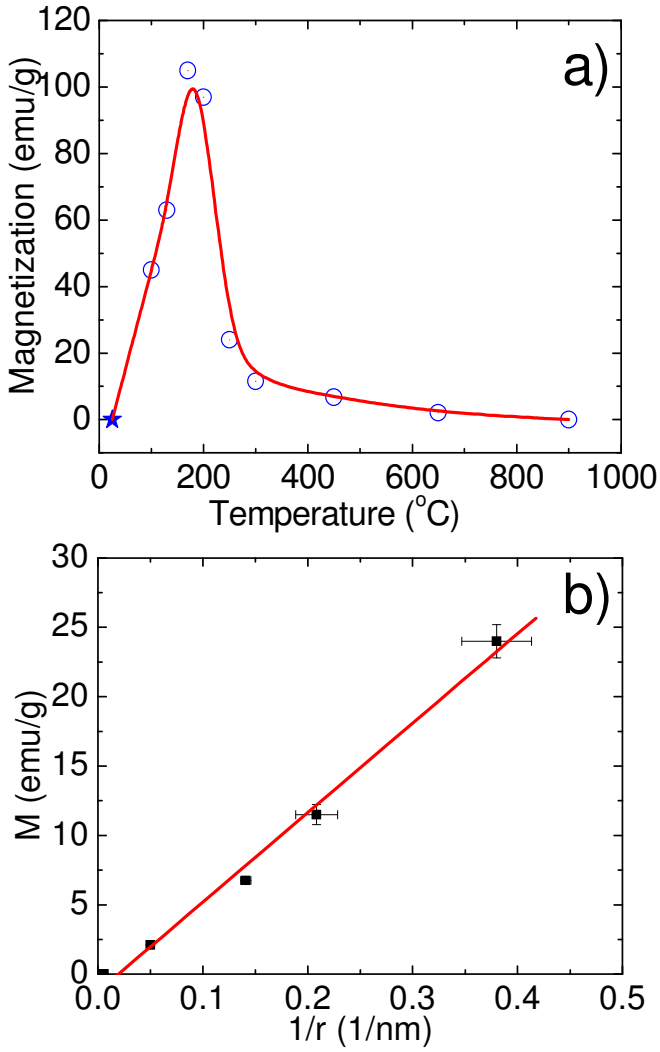

Fig. 4.8. a) Maximum magnetization measured at 2 K under the maximum magnetic field of 50 kOe for the fully amorphous NiO derived from sputtering and powders derived from co-precipitation annealed at different temperatures (the star symbols the magnetization of the fully amorphous structure); b) maximum magnetization versus the inverse of the grain sizes (1/r) for nanocrystalline NiO particles (after annealing at 300 ^{o}C or higher).

Only very small magnetization could be obtained when the annealing was carried out at 650 ^{o}C. It should be noted that the NiO powder annealed at 200 ^{o}C resulted in a magnetization of 95 *emu/g,* slightly lower than that annealed at 170 ^{o}C.

As reported by many research groups [8, 9], uncompensated surface spins existed in nano-sized NiO particles accompanied with an exchange bias and high coercivity. For the samples after annealing at 300 ^{o}C or higher, the maximum magnetization was plotted as a function of the inverse of grain size (1/r), shown in Fig. 4.8b. The linear relationship suggests that the uncompensated surface spins may be attributed to the magnetization (here the 1/r is derived from the surface area πr^2 over the volume $4/3\pi r^3$. It clearly show that the larger the surface area, the larger the maximum magnetization). The details of the uncompensated surface spin, exchange coupling between surface spin and the antiferromagnetic core are discussed in the sub-chapter 4.7.

4.5 Antiferromagnetism in the fully amorphous NiO

Fig. 4.9 shows the magnetization curves of an amorphous NiO taken at different

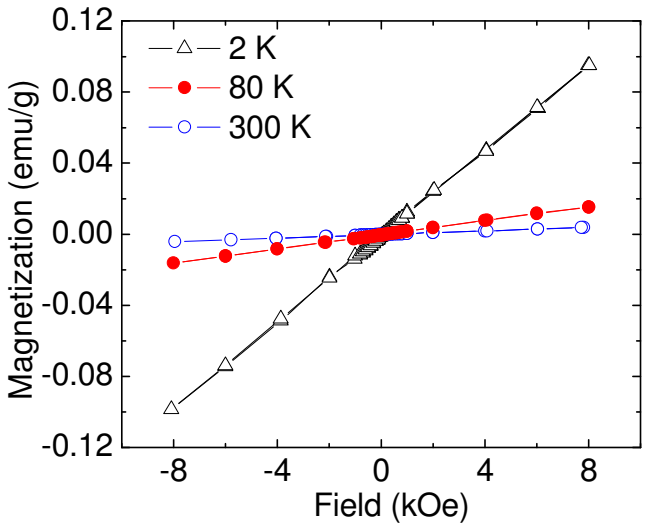

Fig. 4.9. Magnetization curves of a fully amorphous NiO film derived from sputtering.

temperatures. The magnetization curves taken in the entire temperature range (2–300 *K*) showed a linear relationship between magnetization and magnetic field. Hence, NiO

in the amorphous state cannot be ferromagnetic. It may be paramagnetic or antiferromagnetic.

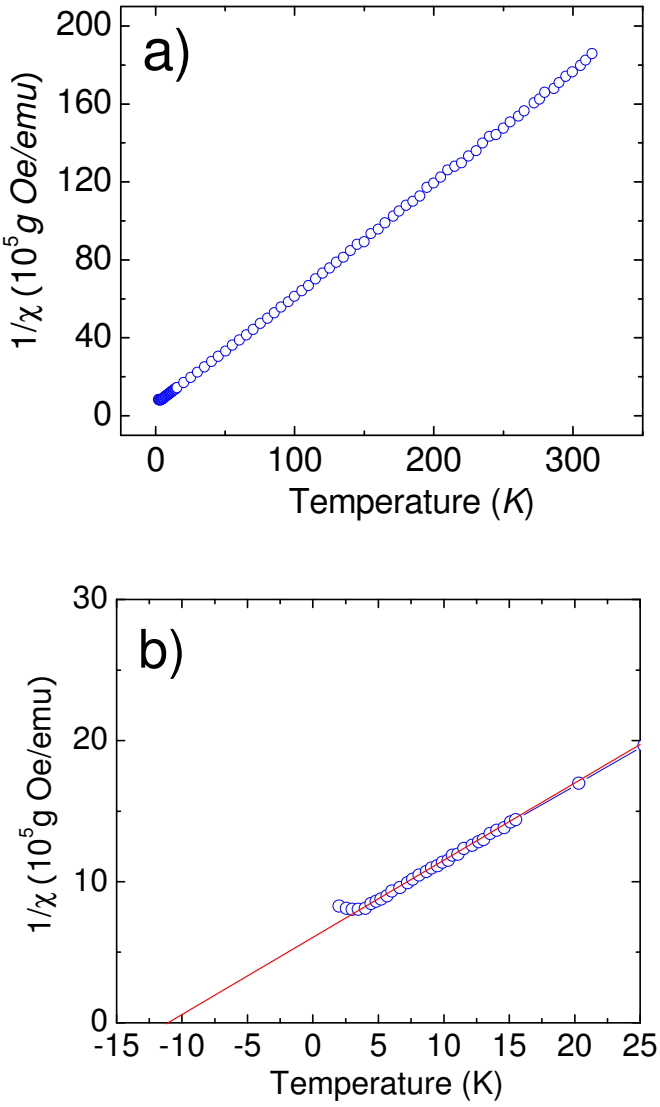

Fig. 4.10. a) The reciprocal susceptibility of an amorphous NiO film deposited using sputtering and b) the enlargement of the low temperature area of a).

It is known that the reciprocal susceptibility can differentiate the paramagnetic or antiferromagnetic behavior of a magnetic material [10]. The susceptibility was measured by SQUID in the temperature range of 2–300 *K* (Fig. 4.10). From the curve,

one can see the linear relationship between the reciprocal susceptibility and the temperature, as shown in Fig. 4.10a. The enlargement of the curve at low temperatures showed a minimum at 3.5 *K* (Fig. 4.10b). Such a minimum is expected in antiferromagnetism [11] since the extension of the linear part led to an intersection with the *x*-axis at -12 *K*. According to the Curie-Weiss law for antiferromagnetism (the magnetic susceptibility $\chi = C/(T-T_c)$), the intersection point is the Curie temperature of the antiferromagnet. In conclusion, the fully amorphous NiO sample is antiferromagnetic with a Néel temperature of 3.5 *K* and a Curie temperature of -12 *K*. The relatively large ratio of Néel temperature/paramagnetic Curie temperature could be attributed to the structural fluctuation of the amorphous structure [12].

4.6 Ferromagnetism in NiO clusters

4.6.1 Estimation of the Curie temperature of NiO clusters

Fig. 4.11 shows the hysteresis loops of the NiO powder annealed at 170 ^{o}C. The hysteresis loops at low temperatures (25 and 2 *K*) showed a ferromagnetic-like behavior. The maximum magnetization at 2 *K* was approximately 105 *emu/g*. The hysteresis loop taken at 2 *K* showed a coercivity of several hundred osterds. However, no coercivity could be observed at 25 *K*, suggesting a superparamagnetism behavior.

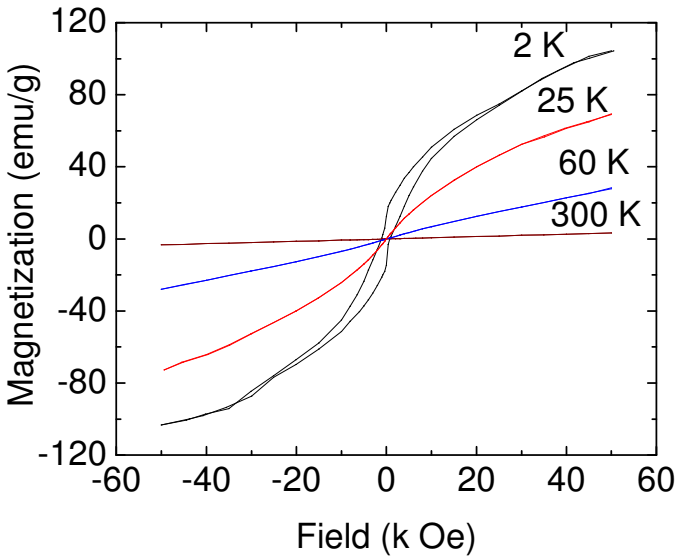

Fig. 4.11. Hysteresis loops of the NiO powder annealed at 170 ^{o}C taken at different temperatures.

For the magnetization curves taken at 60 and 300 *K*, the linear relationship between the magnetization and the applied field suggested a paramagnetic behavior at relatively high temperature.

In order to confirm the ferromagnetism of the NiO powder annealed at 170 ^{o}C, the reciprocal susceptibility was measured with an applied magnetic field of 50 *Oe* (Fig. 4.12). The reciprocal susceptibility is shown to follow the Curie-Weiss law ($\chi = C/(T-T_c)$). It indicates that the powder is ferromagnetic with a Curie temperature of T_C=35 *K*. Below 35 *K*, another critical temperature (T_p= 15 *K*) may be indexed as the spin glass freezing temperature since spin glass behavior has been reported in NiO nanopowders [8, 13].

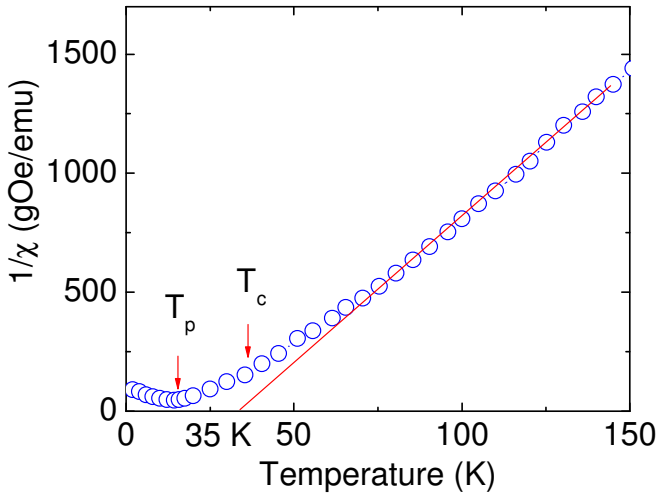

Fig. 4.12. The reciprocal susceptibility of the NiO powder annealed at 170 ^{o}C.

4.6.2 Spin glass behavior

From the previous results, there was another critical temperature in addition to the Curie temperature of the powders. The critical temperature can be the spin glass freezing temperature or blocking temperature of superparamagnetism. DC susceptibility of the sample under different magnetic fields was carried out (Fig. 4.13). It can be seen that the peak is strongly dependent on the applied magnetic field. The cusp shifted to the low temperatures when the magnetic field was increased until it disappeared under a magnetic field of 15 *kOe*. This phenomenon is similar to NiO powders possessing spin glass behavior [13]. Spin glass is a competition interaction between the spin and spin due to the existence of a degree of disorder in magnetic related materials. Spin glass was originally applied to dilute crystalline alloys, such as AuFe or CuMn containing about 1 % of magnetic impurities [12]. For the canonical spin glasses, diluted alloys of transition metals in noble metal hosts show some

characteristic magnetic properties. The details of the information can be obtained in [14].

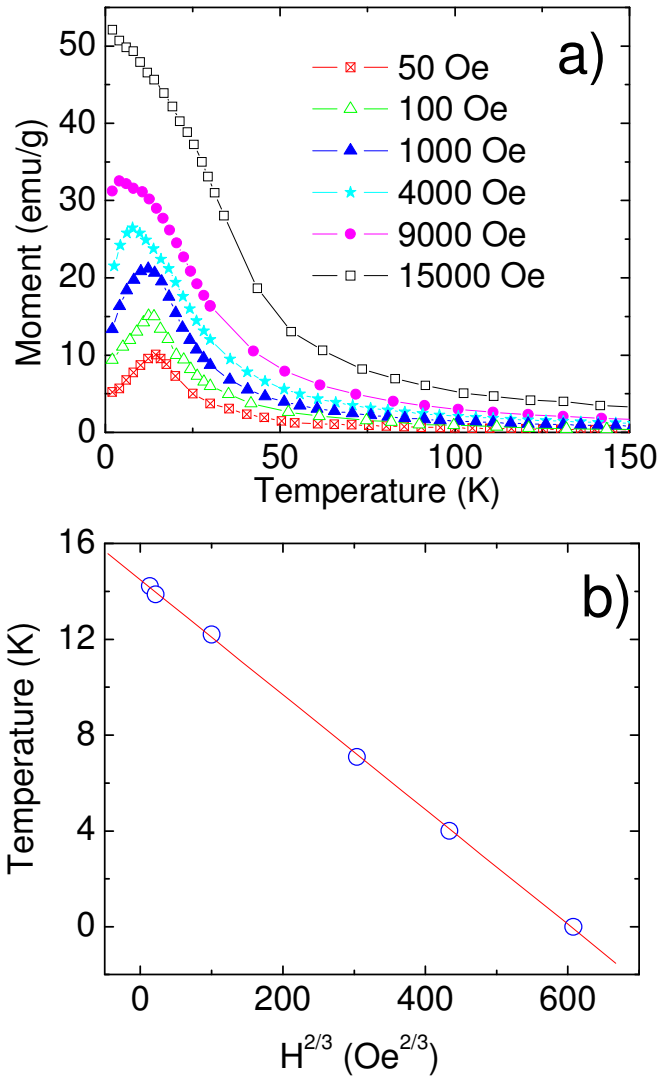

Fig. 4.13. a) Zero-field-cooling (ZFC) curves of the NiO powder annealed at 170 ^{o}C by applying a variety of magnetic fields; b) $H^{2/3} \propto T$ curve of the sample.

In the broadest sense of the term, all the random noncollinear amorphous magnets might be described as spin glass. One of the effective ways to determine spin glass behavior is using the *A-T* line [15]. The fitting formula is shown in Equation (4.1).

$$H_{AT}(T)/\Delta J \propto (1-T/T_F)^{3/2} \tag{4.1}$$

where H_{AT} is the applied magnetic field; T is the temperature at the cusp. By fitting the Equation (4.1) with $H_{AT}^{2/3}$ and T (the temperature at the cusp in Fig. 4.13a), a linear relationship was obtained, as shown in Fig. 4.13b, suggesting a spin glass behavior of the powder.

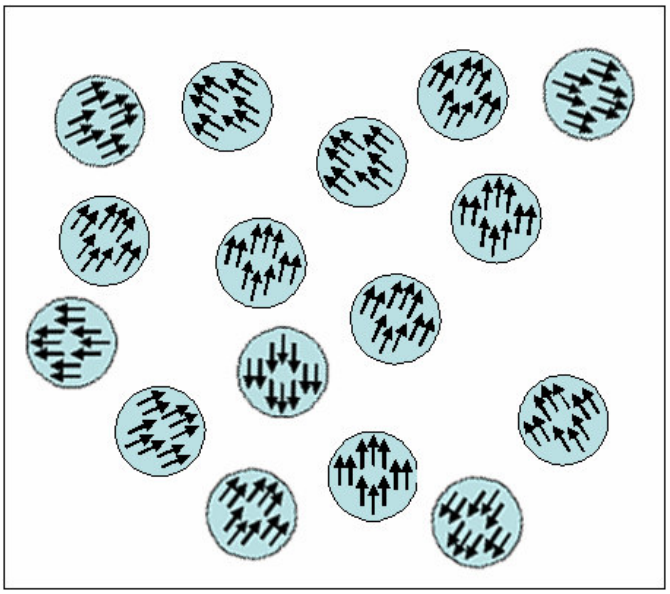

Fig. 4.14. Illustration of the spin glass behavior in the NiO powder annealed at 170 ^oC.

Fig. 4.14 illustrates the possible spin glass interaction in NiO powder after annealing at 170 ^oC. In the powder, small clusters were formed after annealing. Each cluster behaved ferromagnetic with a Curie temperature of 35 *K*. Paramagnetism can be observed at a temperature higher than 35 *K*. With the decrease in the temperature below 35 *K*, ferromagnetic-like behavior appeared due to the exchange coupling between spins inside a cluster. If the temperature further decreases, the random interaction between clusters may be formed via a Ruderman-Kittel-Kasuya-Yosida

(*RKKY)* interaction [16]. The random interaction resulted in a spin glass behavior below 15 *K*.

4.7 First principle calculations

In order to understand the evolution of magnetism of NiO (antiferromagnetism in a uniform amorphous NiO, ferromagnetism and spin-glass in NiO nanoclusters, and antiferromagnetism with canted surface moments in well crystalline NiO nanocrystals), first-principle calculations were performed to investigate the magnetic properties of NiO clusters as well as their dependence on the cluster size. The calculation indicates that the small and simplest cluster structures (see the Fig. 4.15a) prefer the antiferromagnetic state from the energetic point of view. However, ferromagnetic state is preferred by many relatively complicated and medium-sized cluster structures, as demonstrated by one example in Fig. 4.15b. The average magnetic moment per Ni atom (i.e. 2 μ_B) decreases rapidly with increasing the cluster size. As shown in Fig. 4.15c, the cluster consisting of 32 Ni atoms is antiferromagnetic with a small uncompensated magnetic moment of 0.3 μ_B. The study on clusters consisting of a total number of Ni atoms from 20 to 100 has revealed that the Ni atoms on the surface are attributed to the uncompensated magnetic moment. The uniform amorphous structure could be understood as a random assembly of the simplest Ni-O clusters. The antiferromagnetism of amorphous NiO observed by experiment agrees well with the first-principle calculation. Antiferromagnetism is the preferred state of simplest Ni-O bonds which are elements of random networks of the uniform amorphous structure.

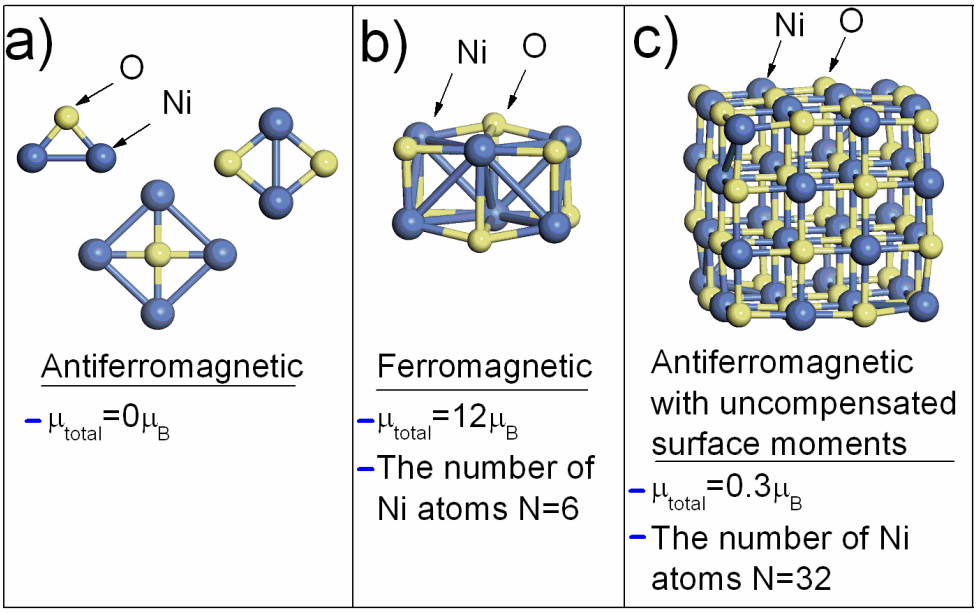

Fig. 4.15. Optimized structures of NiO clusters. a) Samples with small clusters (Ni_2O, Ni_4O and Ni_2O_2) showing antiferromagnetic behavior. Spins are compensated through exchange interaction between Ni atoms and oxygen; b) a sample with medium-sized NiO cluster (Ni_6O_6) showing a ferromagnetic behavior and c) a sample with a large antiferromagnetic NiO cluster ($Ni_{32}O_{32}$) with uncompensated surface moments. Large dark spheres represent nickel atoms while small white spheres indicate oxygen atoms.

As shown in Fig. 4.15b, medium-sized clusters consisting of 5–10 Ni atoms tend to be ferromagnetic. The result also agrees qualitatively well with the experimental observations. The curve of $1/\chi$ versus temperature obeyed the Curie-Weiss law as shown in Fig. 4.12, indicating the ferromagnetic nature of the clusters in the samples after post-annealing at a temperature between 170 and 200 ℃. Experimental results indicated that the ferromagnetism may exist in clusters with a maximum size of approximately 1 *nm* (it is to note that the radius of Ni atoms is approximately 0.18 *nm*). The random distribution of the magnetic anisotropy of these clusters and/or *RKKY* (Ruderman-Kittel-Kasuya-Yosida) interactions between clusters may lead to a spin-glass behavior and require a large magnetic field to reach the magnetization saturation (cluster glass) [17, 19]. As shown in the first-principle calculations, the ferromagnetic

state cannot exist in larger clusters (with a total number of Ni atoms > 20). This is because, for large clusters, the interior recovers its bulk behavior and therefore remains antiferromagnetic. A weak magnetism of the large clusters is attributed to uncompensated surface moments.

4.8 Core/shell interactions in nanocrystals

4.8.1 The description of surface spins and antiferromagnetic core

From experimental results and first principle calculation, fully amorphous NiO was antiferromagnetic. Ferromagnetism was observed in NiO clusters. When the size of NiO became larger than the cluster (1 *nm*), the NiO particles consist of uncompensated surface spins (ferromagnetic coupling) and antiferromagnetic core. The structure of the nanosized NiO is shown in Fig. 4.16. The core/shell structure of antiferromagnetic powders has been widely investigated [8,9,13,18,19,20]. A typical characteristic of the core/shell structure is the powder to show an exchange bias, which is induced the exchange coupling between the surface ferromagnetic spins and antiferromagnetic core. This exchange bias was observed in NiO powders [8,9, 21].

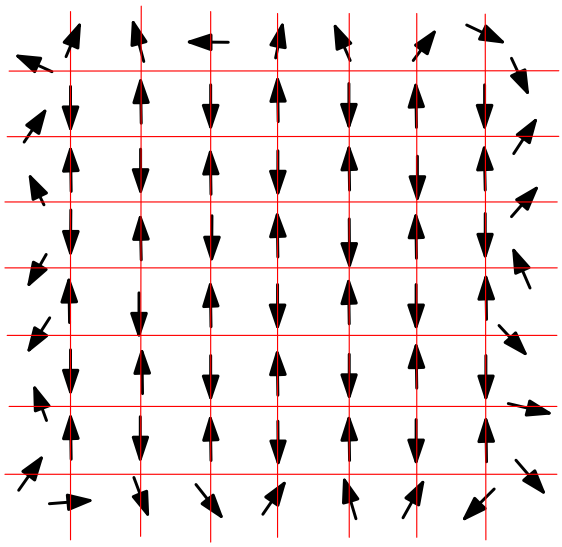

Fig. 4.16. The structure of the NiO powder with surface spins and an antiferromagnetic core.

4.8.2 Annealing temperature dependence on the exchange bias and coercivity of the NiO powders

Fig. 4.17a shows the zero-field-cooling (ZFC) and field-cooling (FC) hysteresis loops of the Ni powder annealed at 170 ^{o}C with a magnetic field of 5 T. The two loops nearly overlapped. This indicates that there is no exchange bias from the powder. The result supports that the NiO nanoclusters annealed at 170 ^{o}C are ferromagnetic and do not have the core/shell behavior. There was no antiferromagnetic component for the exchange coupling. Fig.4. 17b shows the ZFC and FC hysteresis loops of the powder annealed at 650 ^{o}C. It is differenct from the powder annealed at 170 ^{o}C. An exchange bias (absolute value of the difference between the positive coercivity and negative coercivity) of 2.7 kOe can be observed from the FC hysteresis loop. Hysteresis loop of the sample after field cooling shifted to the negative side of the applied magnetic field. The shift is due to the exchange coupling between the surface spins and antiferromagnetic core. The trend of the coercivity and exchange bias of NiO powders

annealed at different temperatures is shown in Fig. 4.17c. Amorphous NiO prepared by sputtering did not show coercivity and exchange bias (first point with cross in Fig. 4.17c). For the powder annealed at 170 ^{o}C, a small coercivity but no exchange bias could be observed. When the annealing temperature was 300 ^{o}C, the largest coercivity of 3.15 *kOe* was obtained. When the annealing temperature was increased further, the coercivity gradually decreased. However, the largest exchange bias was observed in the powder annealed at 450 ^{o}C. When the annealing temperature was higher than 450 ^{o}C, both coercivity and exchange bias monotonically decreased. The trend of coercivity and exchange bias may be related to the "thickness" of the surface spins and the crystallinity of antiferromagnetic core [3, 22-24]. The mechanism of the high coercivity in the powder annealed at 300 ^{o}C is not very clear. It may be related to the small grain size (3.5 *nm*) of the NiO powders. During magnetic reversal, the surface ferromagnetic spins may drag more antiferromagnetic core spins to follow the magnetic reversal paths due to the small size of the NiO core. This is a term called a spin flopping behavior [25].

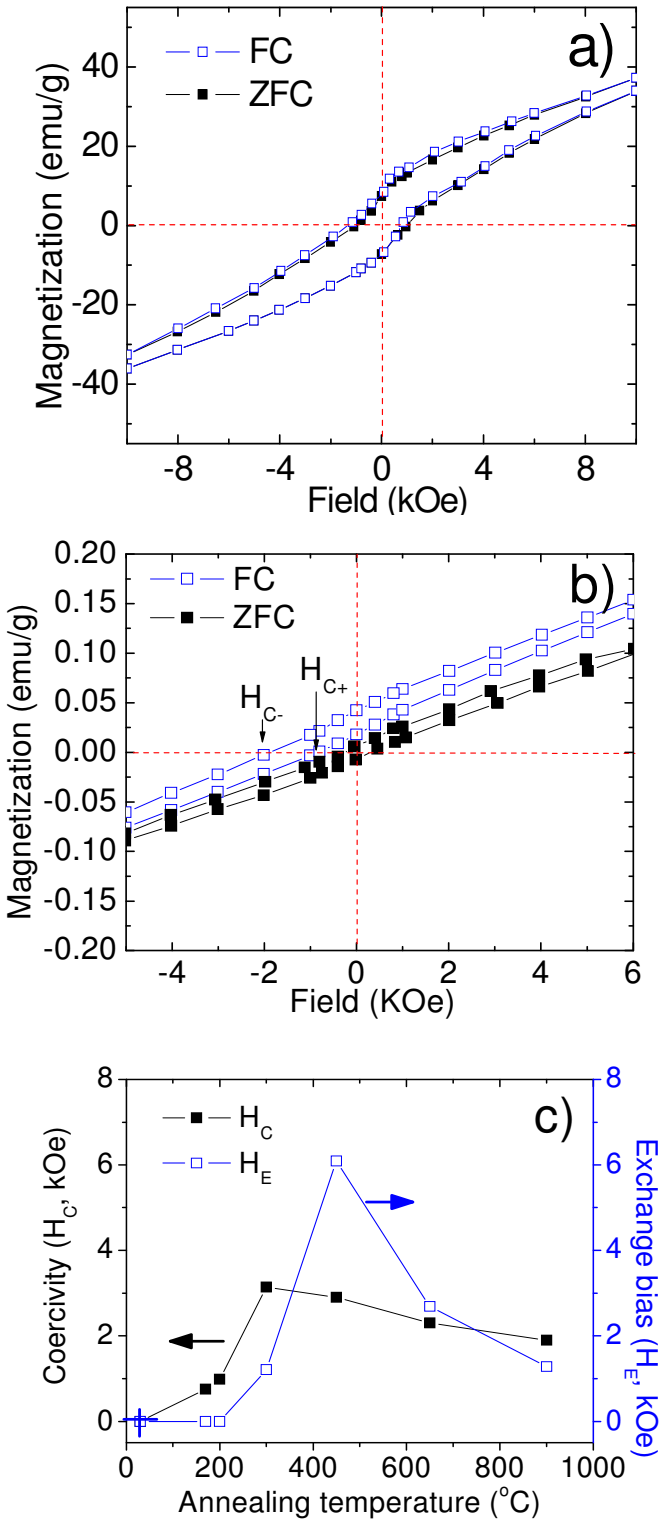

Fig. 4.17. ZFC and FC hysteresis loops of NiO powders annealed at a) 170 °C and b) 650 °C (all the values were taken at 2 K); c) the summary of the exchange bias ($|H_{C-} - H_{C+}|$)and coercivity (H_{C-}) versus annealing temperature of NiO powders. The first point with cross is the value of an amorphous NiO prepared by sputtering.

4.8.3 Temperature dependence of exchange bias and coercivity of NiO powders annealed at different temperatures

Fig. 4.18 shows temperature dependence of NiO powders annealed at different temperatures. Both the exchange bias and coercivity were strongly dependent on the temperature. The exchange bias and coercivity were zero at the temperature above 100 K for the powder annealed at 300 ^{o}C. The coercivity and exchange bias increased monotonically with the decrease in the temperature. The highest coercivity (3.15 kOe) was achieved when the temperature was at 2 K. Similar results were observed for the NiO powder annealed at 450 ^{o}C. Both the coercivity and exchange bias were zero at temperatures above 250 K. The coercivity and exchange bias increased with decreasing the temperature. The exchange bias could still be observed at the temperature of 400 K for the powders annealed at 600 ^{o}C. The graph indicates that the exchange bias is related to a critical temperature, beyond which, the exchange bias disappears. The critical temperature is called the blocking temperature (T_b) [3]. Blocking temperature is of importance both technically and engineering since above the blocking temperature, the antiferromagnetic state disappears. Hence, the applications of exchange couping materials can only be used below the blocking temperature of an antiferromagnet. In addition, the disappearance of the antiferromagnetic state can be used to study the mechanism of exchange coupled films and their magnetic properties. From the analysis above, it showed that the blocking temperature with increasing annealed temperatures, which may be related to the increasse in the grain size of NiO powders.

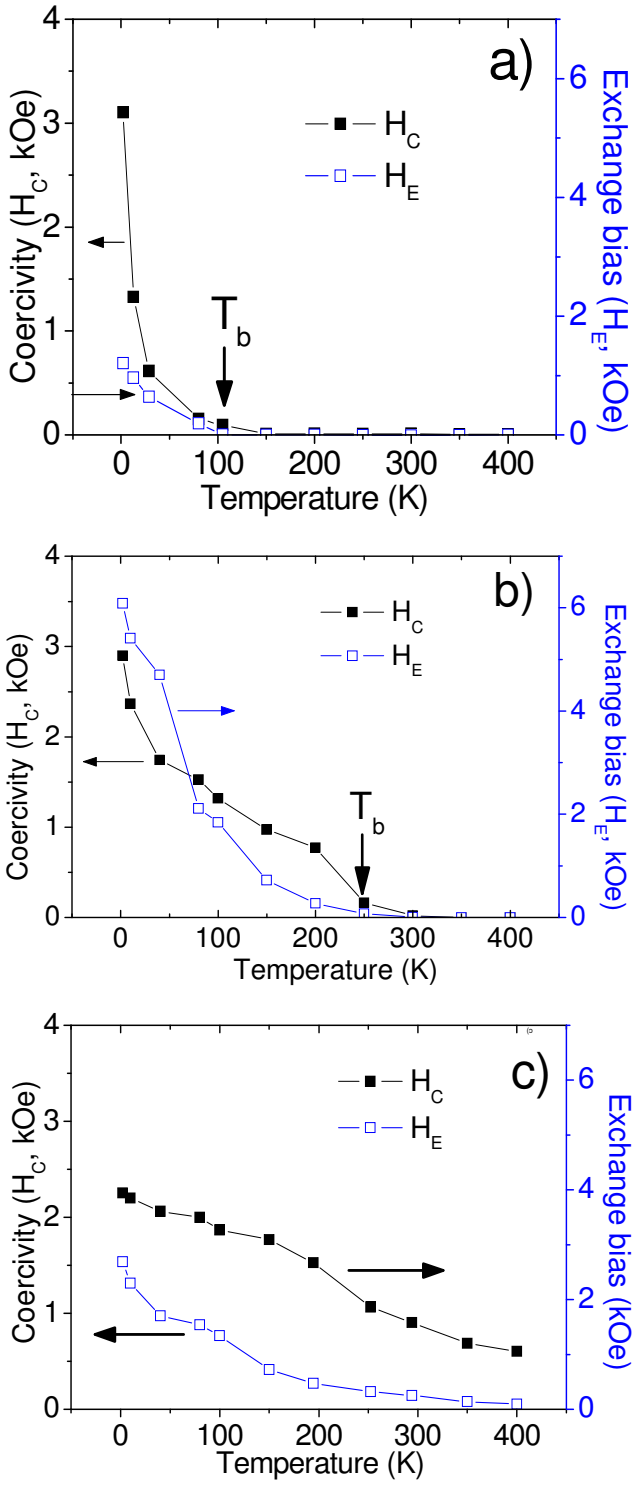

Fig. 4.18. Temperature dependence of the coercivity and exchange bias of NiO powders annealed at a) 300 °C; b) 450 °C and c) 650 °C.

4.9 Superparamagnetism in NiO powders

4.9.1 Superparamagnetism according to Néel model

The above results have shown that there is a blocking temperature for the exchange coupling between the surface spins and antiferromagnetic core. What induces the

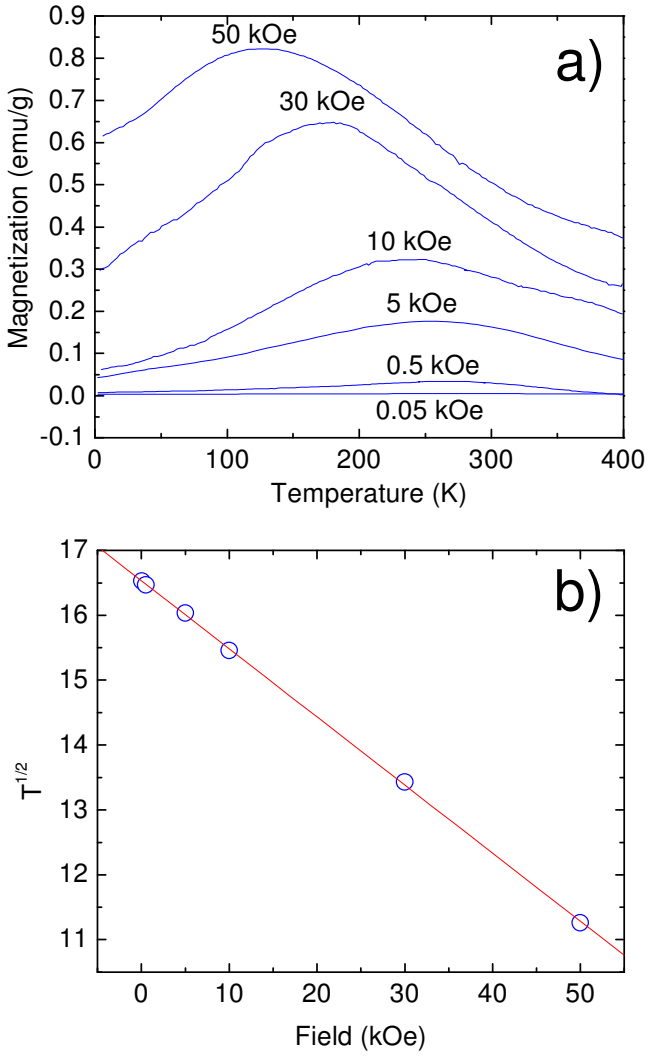

Fig. 4.19. a) Zero-field-cooling (ZFC) curves of the NiO powder annealed at 450 ^{o}C by applying a variety of magnetic fields; b) the square root of the critical temperature as a function of the applied field ($T_C \propto [H_K - H]^2$).

blocking temperature is certainly of great interest. Due to the practical applications, the blocking temperature should be above room temperature. The understanding of the

phenomenon behind the blocking temperature of NiO may enable the adjustment and control of the blocking temperature beyond room temperature.

In order to understand the behavior of the blocking temperature of NiO annealed at different temperatures, zero-field-cooling (ZFC) curves with different applied magnetic fields were carried out**,** as shown in Fig. 4.19. Similar to the NiO powder annealed at 170 ^{o}C, the measured peaks shifted to low temperatures when the applied field increases. Superparamagnetism of NiO powder was observed by Bahl and Richardson *et al* [26,27]. According to Néel's model [28,29], the blocking temperature of superparamagnetism can be represented by the equation shown below:

$$T_b \propto V[H_K - H]^2 \qquad (4.2)$$

where V is the volume of a single particle , H_K is a constant and H is the applied magnetic field during the measurement. By fitting T_b *vs* H^2, Fig. 4.19b was obtained. Obviously, the shift of the peaks can be well fitted using Equation (4.2), suggesting superparamagnetism behavior of the powder. Similarly, ZFC curves of the NiO powder annealed at 300 ^{o}C could also be fitted using Equation (4.2), indicating superparamagnetism behavior. It should be noted that the blocking temperature of the NiO powder annealed at 650 ^{o}C could not be determined as the blocking temperature was higher than 400 K, which is the highest operation temperature of the available SQUID system.

4.9.2 Anisotropy of NiO Powders

From the previous discussion, NiO powder annealed at 300 and 450 ^{o}C showed superparamagnetism. For the non-interacting particles with uniaxial magnetic

anisotropy, the superparamagnetic relaxation can be described by the Néel expression [30].

$$KV = kT \ln(\frac{\tau}{\tau_0}) \quad (4.3)$$

where k is Boltzmann's constant, T is the temperature, K is the magnetic anisotropy energy constant and V is the particle volume. Normally, τ_0 can be taken as 10^{-9} s. For the SQUID measurement, the measurement time is approximately 4 s.

$$KV = kT \ln(\frac{4}{10^{-9}}) \quad (4.4)$$

Then we get EQ (4.5).

$$KV = 22kT \rightarrow K = \frac{22kT}{V} \quad (4.5)$$

If the ordering temperature is assumed as the blocking temperature of the superparamagnetic behavior of NiO powders, the anisotropy energy constant of NiO powders can be estimated. V is $\pi D_m^3 / 6$, where D_m is the average diameter of the grain size obtained from the XRD spectra and TEM analysis, as shown in Fig. 4.4~4.7. T is the ordering temperature observed from the reverse susceptibility of the zero-field-cooling curves. The calculated K values of NiO powders annealed at different temperatures are listed in Table 4.1.

Table 4.1, The calculated anisotropy energy constant of NiO powders annealed at different temperatures.

NiO powders	D_m (nm)	T_b (K)	$\frac{22kT_b}{V}$ (J/m^3)
300 ^oC	4.8	85	4.45×10^5
450 ^oC	7.1	277	4.48×10^5
600 ^oC	18.2	--	--

Table 4.1 shows the calculated anisotropy energy based on Equation 4.5. For the powder annealed at 300 ^oC, the anisotropy energy constant is 4.45×10^5 J/m^3. The value is very close to that of bulk NiO (3.3×10^5 J/m^3). In addition, the anisotropy energy constant of the powders annealed at 450 ^oC showed almost the same value as that of the sample annealed at 300 ^oC. For the sample annealed at the temperature higher than 450 ^oC, the ordering temperature could not be measured because of the limitation of the SQUID, as described in the previous part. The slightly higher anisotropy energy constant of the powders annealed at 300 and 450 ^oC the theoretical value may be due to the error in the calculation of the grain size or the exchange interaction of the powders. The grain size for the 300 ^{o}C annealed samples should be 5.28 nm and the grain size of 450 ^{o}C annealed sample should be 7.81 nm, corresponding to the theoretical anisotropy constant (3.3×10^5 J/m^3). The calculation confirmed that NiO powders annealed at 300 and 450 ^oC showed superparamagnetism. For the NiO powder annealed at 600 ^oC, the calculated critical temperature is 465 K, using K=4.48 $\times10^5$ J/m^3.

4.10 Summary

In this chapter, NiO in the amorphous, cluster and nanocrytalline states was investigated in detail. It showed that NiO in the amorphous state was antiferromagnetic. It had a Néel temperature of 3.5 *K* and a Curie temperature of -12 *K*. NiO powder annealed at 170 ^{o}C had a cluster size of 1-2 *nm*. The clusters showed a maximum magnetization of 105 *emu/g*. The susceptibility study indicated that the NiO powder showed a ferromagnetic behavior with a Curie temperature of 35 *K*. In addition, the powder showed a spin glass behavior with a freezing temperature of 15 *K*.

NiO powders turned to nanocrystalline structures when the powders were annealed temperatures above 170 ^{o}C. The crystallinity of NiO became better with increasing the annealing temperature. By T_P vs H^2 fitting, it demonstrated that NiO powders annealed at 300 and 450 ^{o}C showed superparamagnetism. The magnetization decreased monotonically when the annealing temperature increased. The finite size effect is attributed to the magnetization behavior since the portion of surface spins becomes less for the larger grain size of NiO powders.

The coercivity and exchange bias behaviors were also investigated. The amorphous NiO did not show a hysteresis loop. Hence it did not have an exchange bias or coercivity. NiO powder annealed at 170 ^{o}C did not show a shift of the hysteresis loop in the entire temperature range due to the ferromagnetic behavior of the powder. The coercivity was relatively small at low temperature. However, the NiO powder annealed at 300 ^{o}C showed the largest coercivity. The coercivity may be contributed by the high anisotropy of the surface spins and/or the spin flopping of the NiO core. Large exchange bias was observed when the NiO powder was annealed at 450 ^{o}C. This may

be due to the small portion of surface spins and good crystallinity of antiferromagnetic core of NiO. In order to confirm the structural evolution and magnetic properties of the NiO powders from amorphous, cluster, nanocrystalline to well crystalline structure, first principles calculations were carried out to investigate the arrangement of the Ni and O atoms in these states. The results agree well with the experimental observation.

References

[1]. G.H. Yu, C.L. Chai, F.W. Zhu, J.M. Xiao, and W.Y. Lai, Appl. Phys. Lett. 78, 1707 (2001).

[2]. D.H. Ham, J.G. Zhu, and J.H. Judy, J. Appl. Phys. 81, 4996 (1997).

[3]. J. Nogués and I.K. Schuller, J. Magn. Magn. Mater. 192, 203 (1999).

[4]. C. Kuanr, K. Bijoy, R.E. Camley, and Z. Celinski, J. Appl. Phys. 93, 7723 (2003).

[5]. B. Negulescu, L. Thomas, Y. Dumont, M. Tessier, N. Keller, M. Guyot, and C. Papusoi, J. Optoelectron. Adv. Mater. 4, 333 (2002).

[6]. T. Fix, S. Colis, K. Sauvet, J.L. Loison, G. Versini, G. Pourroy, and A. Dinia, J. Appl. Phys. 99, 043907 (2006).

[7]. P. Seneor, A.B. Mantel, and F. Petroff, J. Phys.: Condens. Matter. 19, 165222 (2007).

[8]. R.H. Kodama, A.E. Berkowitz, E.J. McNiff Jr., and S. Foner, Phys. Rev. Lett. 77, 394 (1996).

[9]. T. Ambrose and C.L. Chien, Phys. Rev. Lett. 76, 1743 (1996).

[10]. S. Chikazumi, "Physics of Magnetism" Robert E. Krieger, Malabar, p280 (1965).

[11]. A. Hirofumi, T. Katsuhis, F. Koji, and M. Shunsuke, Phys. Rev. B, 74, 012411 (2006).

[12]. K. Moorjani and J.M.D. Coey, "Magnetic Glasses", Elsevier, Amsterdam, p339 (1984).

[13]. S.D. Tiwari and K.P. Rajeev, Thin Solid Films 505, 113 (2006).

[14]. J. Durand and M.F. Lapierre, J. Phys. F 6, 1185 (1976).

[15]. J.R.L. de Almedia and D.J. Thouless, J. Phys. A 11, 983 (1978).

[16]. M.A. Ruderman and C. Kittel, Phys. Rev. 96, 99 (1954).

[17]. L. Wang, J. Ding, H.Z. Kong, Y. Li, and Y.P. Feng, Phys. Rev. B 6, 214410 (2001).

[18]. M. Gruyters, Phys. Rev. Lett. 95, 077204 (2005).

[19]. T. Ambrose and C.L. Chien, Phys. Rev. Lett. 76, 1743 (1996).

[20]. J. Nogués, J. Sort, B. Langlais, V. Skumryev, S. Suriňach, J.S. Muňoz, and M.D. Baró, Phys. Reports, 422, 65 (2005).

[21]. D.T. Margulies, F.T. Parker, F.E. Spada, R.S. Goldman, J. Li, R. Sinclair, and A.E. Berkowitz, Phys. Rev. B 53, 9175 (1996).

[22]. M.D. Stiles and R.D. McMichael, Phys. Rev. B, 63, 064405 (2001).

[23]. V. Baltz, J. Sort, S. Landis. B. Rodmacq, and B. Dieny, Phys. Rev. Lett. 94, 117201 (2005).

[24]. S.S.P. Parkin, V.S. Speriousu, L.M. Falicov, F. Mejialira, and J.L. Morán-López (EDs.), "Magnetic Properties of Low-Dimensional Systems II", Springer, Berlin, p110 (1990).

[25]. R.H. Kodama, S.A. Makhlouf, and A E. Berkowitz, Phys. Rev. Lett. 79, 1393 (1997).

[26]. C.R.H. Bahl, M.F. Hansen, T. Pedersen, S. Saadi, K.H. Nielsen, B. Lebech, and S. Mørup, J. Phys.: Condens. Matter. 18, 4161 (2006).

[27]. J.T. Richardson , D.I. Yiagas, B. Turk, K. Forster, and M.V. Twigg, J. Appl. Phys. 70, 6977 (1991).

[28]. T. Bitoh, K. Ohba, M. Takamatsu, T. Shirane, and S. Chikazawa, J. Phys. Soc. Jpn. 64 1305 (1995).

[29]. M.E. Hilo, K. O'Grady, and R.W. Chantrell, J. Magn. Magn. Mater. 114, 307 (1992).

[30]. L. Neél, Ann. Geophys. 5, 99 (1949).

Chapter 5

Magnetic Properties of Ni/NiO Nanocomposites Prepared by Reactive Sputtering

5.1 Introduction

In Chapter 4, the experimental and theoretical work on the magnetic properties of nanostructured NiO powders showed that NiO in a cluster state had a ferromagnetic behavior and possessed a magnetization as high as 105 *emu/g*. However, the high magnetization could only be observed at very low temperature due to its low Curie temperature. It is well known that a nanocomposite of two magnetic phases may exhibit a single magnetic ordering temperature [1-8]. Therefore, the Curie temperature of the NiO clusters may be raised through a suitable coupling with a ferromagnetic phase which possesses a high ordering temperature. In this project, Ni/NiO nanocomposites have been fabricated and studied. It was found that a high magnetization at room temperature could be achieved in the composite consisting of Ni nanograins and NiO clusters. On the other hand, relatively high coercivity at room temperature with a large exchange bias could be obtained in a Ni/NiO composite when the NiO is in a nanocrystalline structure state.

5.2 Experimental Procedure

As discussed in Chapter 4, only relatively large grains (>5 *nm*) of NiO films could be obtained when deposited by sputtering using a sintered NiO target in the available sputtering system. Therefore, NiO films were prepared by reactive sputtering in this work.

Ni/NiO films with a total thickness of 50 *nm* were deposited by sputtering using a single Ni target with a purity of 99.99 %. In order to obtain a Ni/NiO nanocomposite, the sputtering was carried out alternatively under pure argon atmosphere for the deposition of Ni and under an oxygen partial pressure of 1.4×10^{-3} *torr* for the

deposition of NiO. In order to avoid the formation of layered structure, the individual Ni and NiO layers were only with a nominal thickness of 2 *nm*. The deposition rate for the Ni and NiO films was approximately 0.1 *nm/s*. The base pressure of the chamber was 2×10^{-6} *torr*. The deposition pressure was 7×10^{-3} *torr*. The deposition power was 20 *W*. In this work, the research is concentrated on Ni/NiO nanocomposites with a Ni:NiO ratio of 1:1.

5.3. Structural Characterization

5.3.1 Cross-section TEM analysis

Fig. 5.1a shows a cross-section TEM image of a Ni/NiO nanocomposite film. From the image, it is confirmed the deposited film is a relatively uniform Ni/NiO nanocomposite without a layered structure. The study showed that neither Ni or NiO with a thickness of 2 *nm* were not able to form a continuous layer [8]. The formation of a composite is due to the fact that the NiO particles/grains may fill in the crevices of Ni film and vice versa. Hence, the microstructure was a nanocomposite of Ni/NiO. Fig. 5.1b shows the selected area electron diffraction (SAED) of the film in the cross-section. The three rings are indexed to *fcc*-Ni (111), Ni (200) and Ni (220) and no NiO is identified in the as-sputtered state. Hence, NiO may exist as an amorphous structure. Annealing was carried out in an argon atmosphere (a flow rate of 100 *ml/min*) for 30 *min*.

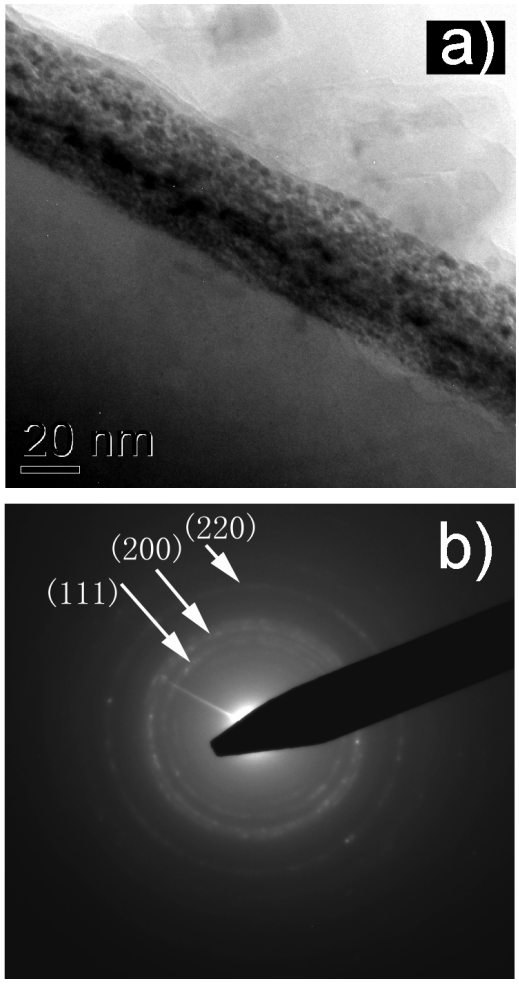

Fig. 5.1 Cross-section TEM micrograph of a Ni/NiO composite,a) and the selected area electron diffraction (SAED) pattern, indicating a Ni phase, b).

5.3.2 XRD analysis

In order to study the effect of annealing on the composite and to make sure that the films were composed of a Ni and NiO, annealing was carried out at different temperatures under an argon atmosphere with a constant period of 30 *min*. As shown in the XRD spectra (Fig. 5.2), only a small peak of *fcc*-Ni (111) could be observed from the as-deposited film. This result indicated that the grains of Ni were very small after the deposition at room temperature, while the NiO was in an amorphous state (as observed and discussed in Chapter 4). After the composite was annealed at 200 ^{o}C, the

intensity of the Ni (111) peak was higher. In addition, *fcc*-Ni (200) peak gradually appeared. However, NiO peaks could not be seen, indicating that NiO may still keep in a disordered state (probably in a cluster state as described in Chapter 4). After the composite was annealed at 350 ^{o}C, a very broad peak of *fcc*-NiO (200) appeared. Based on the Scherrer equation, the average grain size of the NiO was estimated to be 2.8 *nm*, showing a very small grain size (it should be noted that the equipment broadening has been correct. The HFMW of the equipment is approximately 0.1^{o}). When the composite was annealed at 500 ^{o}C, strong peaks could be observed, indicating a better crystallinity compared to that annealed at 350 ^{o}C. The grain size of the NiO was approximately 7.8 *nm* calculated from the Scherrer equation.

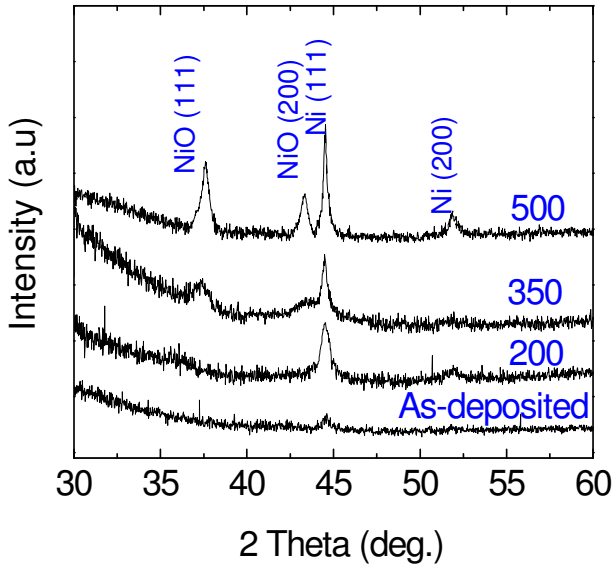

Fig. 5.2. XRD spectra of Ni/NiO composites annealed at different temperatures.

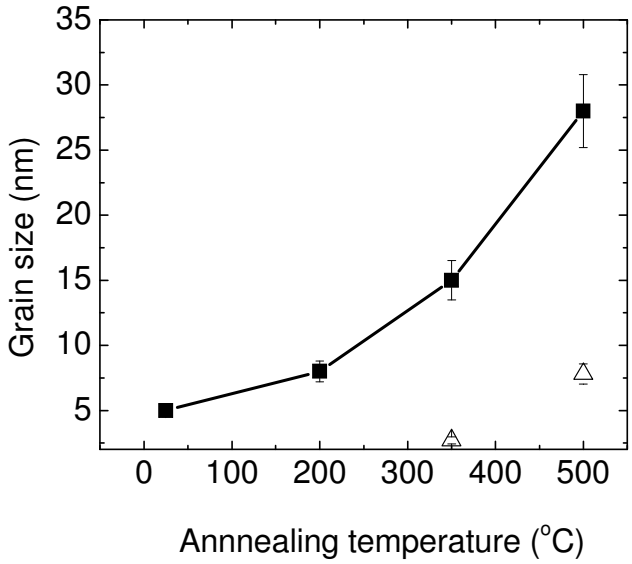

Fig. 5.3. The average grain size of the Ni and NiO phase in Ni/NiO composites calculated from Scherrer equation. The line is a guide to eyes. The two triangle points in the graph are the grain sizes of the NiO films after annealing at 350 and 500 ^{o}C, respectively.

Fig. 5.3 shows the grain size of Ni in the composite dependent on the annealing temperature. The grain size was estimated from the XRD spectra using Scherrer equation. It increased with increasing the annealing temperature. From the graph, the average grain size of the Ni was approximately 5 *nm* when the composite was in the as-deposited state. The grain size of the Ni reached 28 *nm* when the composite was annealed at 500 ^{o}C. The grain sizes of the NiO in the composite annealed at 350 and 500 ^{o}C are also shown in Fig. 5.3 (the two triangle points), which are much smaller than that of Ni.

5.3.3 In-plane TEM analysis

Fig. 5.4 shows plane-view TEM micrographs of Ni/NiO composites before and after annealing at different temperatures. From the micrograph of the as-deposited film (Fig.

5.4a), a large amount of amorphous structure was found. In addition, a *fcc*-Ni (111) plane with a d-spacing of 0.2 *nm* could be identified. The grain size of the Ni was in the range of 5–8 *nm*, consistent with the calculation from XRD patterns. From the discussion in Chapter 4, the amorphous structure was supposed to be NiO. Hence, the as-deposited film consisted of Ni nanograins surrounded by the amorphous NiO. When the composite was annealed at 200 ^{o}C, the bright-field image also indicated a *fcc*-Ni (111) plane with a d-spacing of 0.2 *nm* (Fig. 5.4 b). There was not much change in the grain size of Ni. A large amount of disordered structure (shown by the contrast difference) presented. No crystalline NiO phase could be found, suggesting that NiO may be still in the disordered/amorphous state. In the dark-field image, relatively large grains in the range of 5-8 *nm* and very small grains (1–2 *nm*) coexisted (Fig. 5.4c). The small grains may be NiO grains, similar to that discussed in Chapter 4, i.e, NiO powder after annealing at 170–200 ^{o}C resulted in a structure of clusters with a size in the order of 1 *nm*. Hence, in a Ni/NiO composite, small clusters of the NiO may also be formed after it was annealed at 200 ^{o}C. When the composite film was annealed at 350 ^{o}C, a lattice of *fcc*-NiO (111) plane with a d-spacing of 0.24 *nm* could be observed (Fig. 5.4d). The film showed a better crystallinity than that of the film in the as-deposited state and the film annealed at 200 ^{o}C. The average grain size of the NiO was smaller than 5 *nm*. At the same time, a relatively large grain with a d-spacing of 0.2 *nm* could be seen from the image, signaling Ni grains. The TEM results showed the NiO evolution from amorphous, cluster to nanocrystalline structure in the Ni/NiO composite films with increasing the annealing temperature.

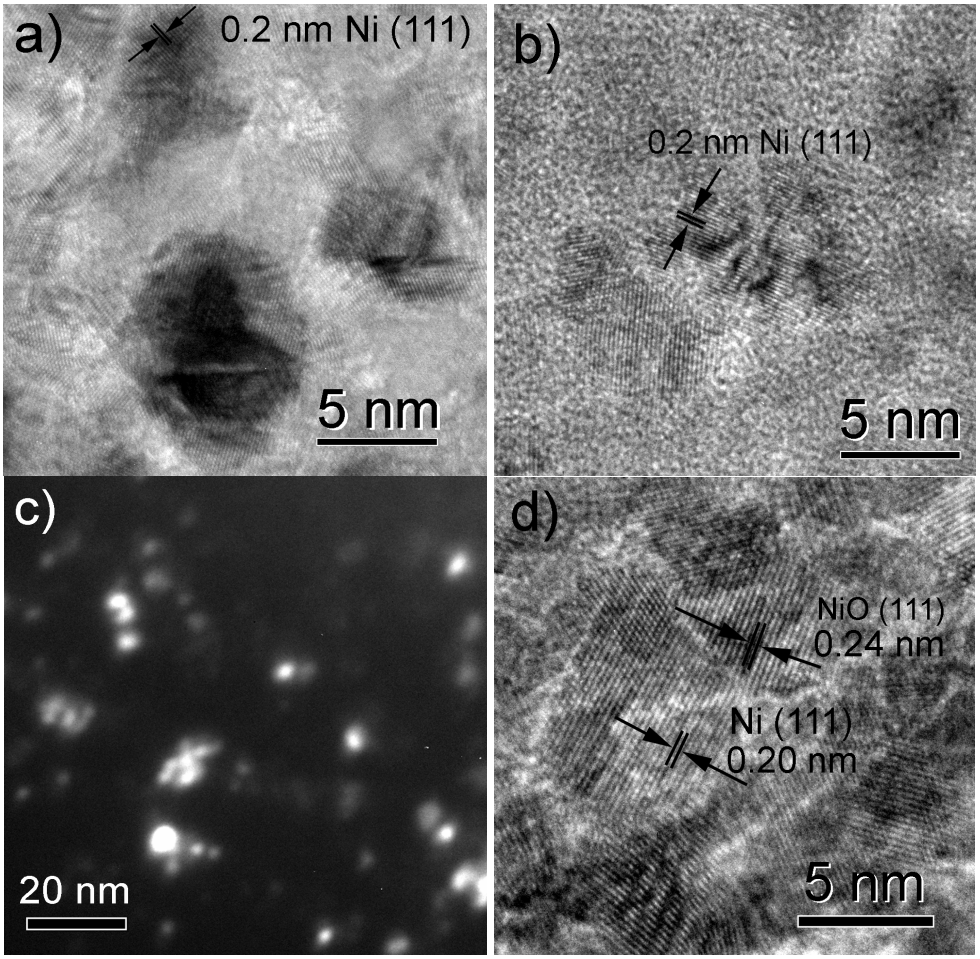

Fig. 5.4. Bright-field TEM micrographs of a Ni/NiO composite a) in the as-deposited state; b) after annealing at 200 ^{o}C under an argon atmosphere; c) dark-field micrograph of a composite after annealing at 200 ^{o}C and d) bright-field micrograph of a Ni/NiO composite after annealing at 350 ^{o}C under an argon atmosphere.

5.4 Magnetization of a Ni/NiO composite

5.4.1 Saturation magnetization of a Ni/NiO composite annealed at different temperatures

NiO phase has shown various states in Ni/NiO composites after annealing at different temperatures. The investigation of the magnetization of the composites may be of interest. Fig. 5.5 shows the room temperature saturation magnetization of a Ni/NiO composite after annealing at different temperatures. In the as-deposited state, the NiO was in an amorphous state. The magnetization was low (approximately 25 *emu/g*). As

discussed in Chapter 4, fully amorphous NiO was antiferromagnetic. Hence, the magnetization was expected to be around 27 *emu/g* (50 % of the saturation magnetization of pure Ni, 54 emu/g), consistent with the experimental result (25 *emu/g*).

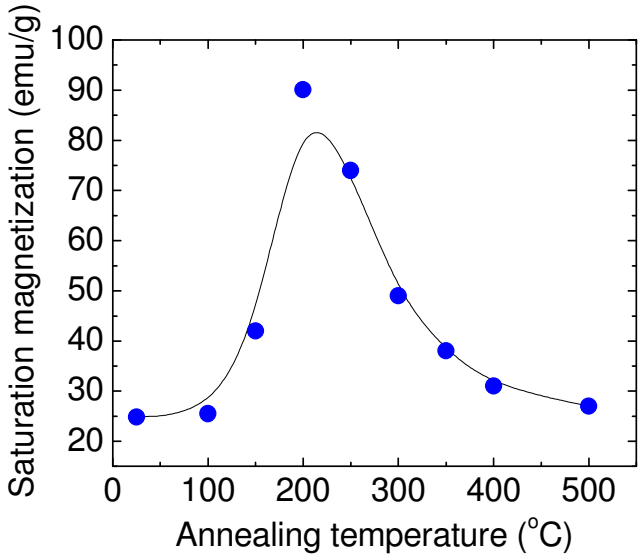

Fig. 5.5. Room temperature saturation magnetization of Ni/NiO composites annealed at different temperatures under an argon atmosphere.

With increasing the annealing temperature, the magnetization drastically increased. A saturation magnetization of 91 *emu/g* at room temperature was achieved when annealing was carried out at 200 ^{o}C. If the annealing temperature is higher than 200 ^{o}C, the saturation magnetization will decrease. It has been predicted that Ni can possess a moment of 1.8 μ_B/*atom* when it is in a cluster state with only 3-5 atoms [9]. The high magnetic moment of Ni nanoclusters was confirmed experimentally by Apsel *et al* [10]. However, in this work, the grain size of Ni was larger than 5 *nm* after annealing at 200 ^{o}C. The Ni phase was not in the small cluster state and the Ni phase may not be attributed to the high magnetization. Therefore, the high magnetization is possible from the NiO phase. In Chapter 4, it showed that nanoclusters of NiO could have a

maximum magnetization of 105 *emu/g*. In this chapter, NiO was firstly deposited by sputtering in an amorphous state. Then the film was annealed at 200 ^{o}C. The situation is similar to that of the NiO powder annealed at 170 ^{o}C, as described in Chapter 4. Dark-field TEM image shown in Fig. 5.4c showed the small clusters of NiO, similar to that shown in Chapter 4. Therefore, the cluster NiO may contribute to the high magnetization. When the annealing of the composite was carried out at a temperature higher than 200 ^{o}C, the saturation magnetization monotonically decreased. This is due to the grain size of the NiO gradually increaseing and the NiO becomes an antiferromagnet with increasing the annealing temperature. An antiferromagnet has a low magnetization. Hence, the saturation magnetization of the composite decreased. It should be noted that a composite annealed at 170 ^{o}C resulted in a magnetization approximately 85 *emu/g*, slightly lower than that annealed at 200 ^{o}C.

5.4.2 In-plane and out-of-plane hysteresis loops of a Ni/NiO composite annealed at 200 ^{o}C

In order to confirm the high magnetization of a Ni/NiO composite after annealing at 200 ℃, the following three experiments (room temperature hysteresis loops, Curie temperature and temperature-dependent magnetization) were carried out. Fig. 5.6 shows the in-plane and out-of-plane hysteresis loops of a Ni/NiO composite annealed at 200 ^{o}C. The loops were measured at 300 *K*. The hysteresis loops showed that the composite had a saturation magnetization of 91 *emu/g*, as discussed in Fig. 5.5. The coercivity was approximately 220 *Oe*, which was similar to that of pure Ni film. It implies that the NiO clusters may not affect the coercivity of Ni significantly at room temperature. From the curve, one can observe that the saturation field of the film in the out-of-plane was as large as 7–8 *kOe*. Similar phenomenon was also encountered in the

Ni films deposited by polyol process [11]. It is known that a continuous magnetic thin film will exhibit a similar trend for a saturation field magnitude (when measured out-of-plane) to its saturation magnetization due to the shape anisotropy [11]. The high saturation field of the composite indicates that the saturation magnetization of the film is higher than that of bulk Ni (Ni in the form of thin film requires a saturation field of 4–5 *kOe*).

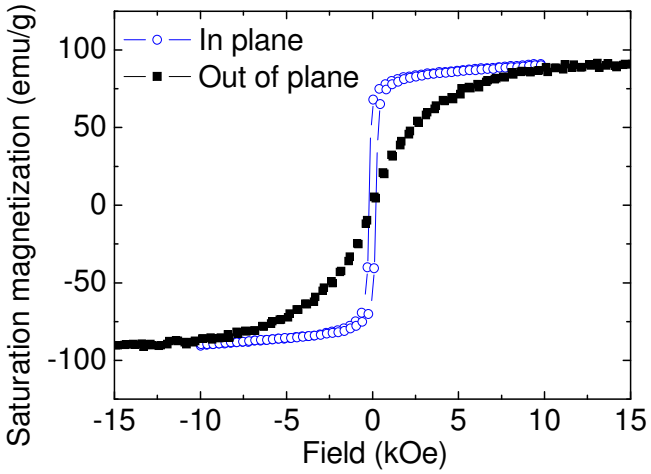

Fig. 5.6. In-plane and out-of-plane hysteresis loops of a Ni/NiO composite annealed at 200 ^{o}C (the loops were taken at 300 K).

5.4.3 Temperature dependence of magnetization of Ni/NiO composite annealed at 200 ^{o}C

Fig. 5.7 shows the maximum magnetization (under an applied field of 10 *kOe*) versus temperature in the temperature range of 2–400 *K*. The magnetization increased from ~90 *emu/g* at room temperature to ~110 *emu/g* at 2 *K*. The behavior was very different to bulk Ni, which has an increase in the magnetization of approximately 5 % from room temperature to 2 *K*. The magnetization of the Ni/NiO composite increased rapidly at low temperatures (below 100 *K*). It might be associated with the ordering temperature of NiO clusters since NiO clusters can show higher magnetization at lower temperature.

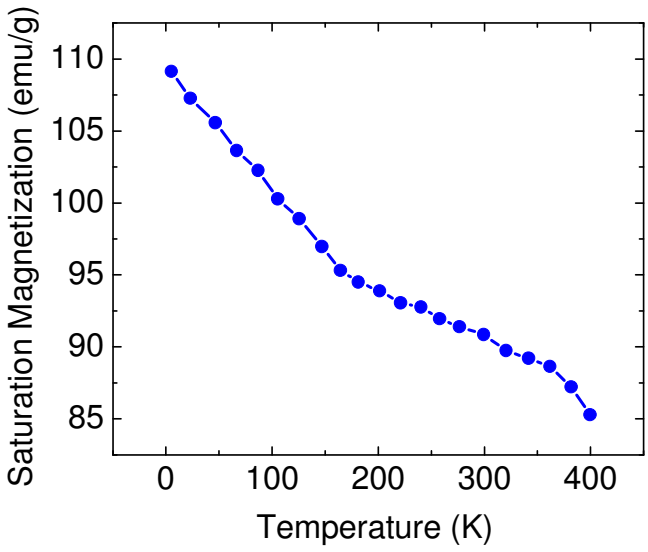

Fig.5.7. Temperature dependence of the saturation magnetization of a Ni/NiO composite after annealing at 200 ℃.

5.4.4 Curie temperature of Ni/NiO composite annealed at 200 ^{o}C

The NiO clusters were supposed to have a significant contribution to the high magnetization of the composite annealed at 200 ℃. However, it showed in Chapter 4 that NiO clusters had a high magnetization only at low temperature. Therefore, the high magnetization at room temperature in this work must be due to the exchange coupling between the ferromagnetic Ni (it has a high Curie temperature but a relatively low magnetization) and ferromagnetic NiO clusters (it possesses a high magnetization, but a low Curie temperature, around 35 K as described in Chapter 4). For a nanocomposite with two ferromagnetic phases, the overall Curie temperature may be given based on the mean-field model [4, 5]. In this model, the interaction responsible for the Curie temperature (T_C) of a ferromagnet is the exchange energy, $E_{\text{int}ra}$, neighboring spins S_i and S_j:

$$E_{\text{int}\,ra} = -2J_{\text{int}\,ra}S_i \bullet S_j \tag{5.1}$$

For the interlayer interaction, the interlayer exchange energy $E_{\text{int}\,er}$ is given by

$$E_{\text{int}\,er} = -J_{\text{int}\,er}\frac{M_{N\,i} \bullet M_{NiO}}{\left|M_N i\right|\left|M_{NiO}\right|} \tag{5.2}$$

In the first approximation, one can calculate T_C by

$$T_C = \frac{1}{K_B}(\frac{2}{3}J_{i\,ntra}S(S+1)Z + J_{\text{int}\,er}\frac{M_{Ni} \bullet M_{NiO}}{\left|M_{N\,i}\right|\left|M_{NiO}\right|}) \tag{5.3}$$

here, T_C is the Curie temperature of the composite. K_B is the Boltzmann constant. M is the magnetization. From the Equation (5.3), T_C is strongly dependent on the interlayer exchange coupling term. In this work, both nanocrystalline Ni and NiO clusters are ferromagnetic. However, the Curie temperature of the NiO in the cluster state is very low (around 35 K). The strong exchange coupling may result in an overall Curie temperature higher than that of the NiO in the cluster structure. The temperature-dependent magnetization curve is shown in Fig. 5.8. A Curie temperature of 593 K was obtained. The Curie temperature was much higher than that of the NiO clusters (35 K), and was lower compared to that of bulk Ni (630 K), as shown in Fig. 5.8 [12]. The overall Curie temperature of the composite falling in between the high Curie temperature and low Curie temperature of the two ferromagnetic phases is consistent with that reported [4-5]. Due to the direct coupling between NiO and Ni phase, there is only one Curie temperature for the Ni/NiO composite [6, 7, 13].

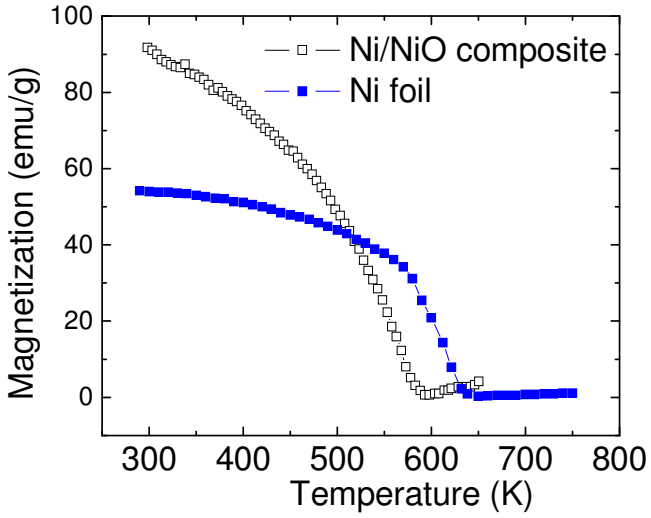

Fig. 5.8. Curie temperature of the Ni foil and Ni/NiO composite annealed at 200 ^{o}C.

5.5. Exchange bias phenomenon in a Ni/NiO composite

5.5.1 Hysteresis loops taken at different temperatures

It is well known that exchange bias could be obtained in a Ni/NiO nanocomposite because of the exchange coupling between ferromagnetic Ni and antiferromagnetic NiO [14,15]. However, the exchange bias was small as well as the coercivity. In this work, Ni/NiO composites annealed at different temperatures were selected for the investigation of the exchange bias and coercivity in order to reveal the effect of the grain size effect on the magnetic properties of the composite. Fig. 5.9 shows the hysteresis loops of the composites in the as-deposited state and after annealing at 200℃. During the experiment, the samples were cooled down from 400 *K* to the measured temperature under a constant magnetic field of 10 *kOe*.

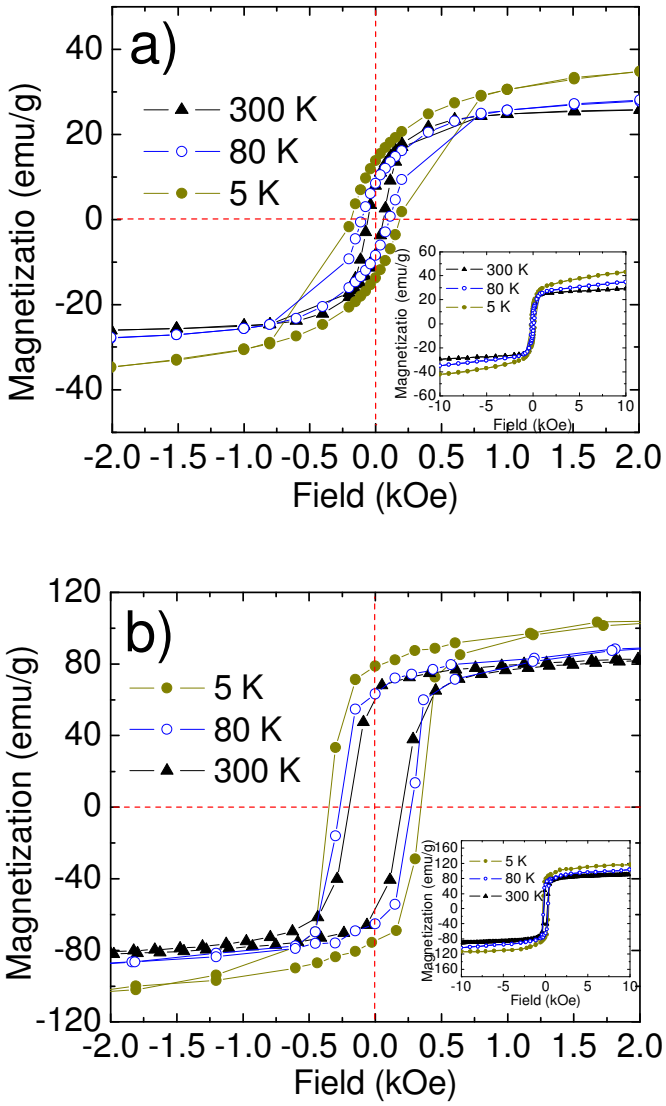

Fig. 5.9. Hysteresis loops of Ni/NiO composites a) in the as-deposited state; b) annealed at 200 ^{o}C with an applied magnetic field of 10 kOe. The insets are the hysteresis loops in a large range of the applied field (10 kOe) of the corresponded plot.

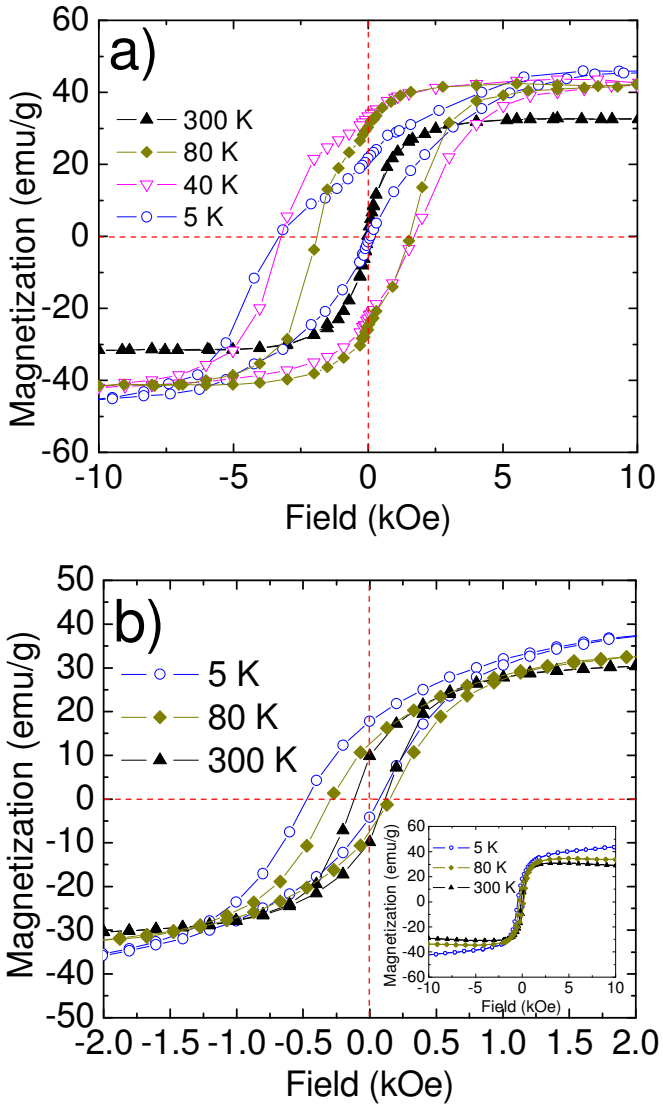

Fig. 5.10. Hysteresis loops of Ni/NiO composites a) annealed at 350 ^{o}C with an applied magnetic field of 10 kOe and b) annealed at 500 ^{o}C under an applied magnetic field of 10 kOe. The insets are the hysteresis loop in a large range of the applied field (10 kOe) of the corresponded plot.

The as-deposited sample had very low coercivity and did not have exchange bias as the hysteresis loops showed symmetrical shapes (Fig. 5.9a). The low values of coercivity are close to those of pure Ni films as discussed in Chapter 3. As NiO in the amorphous state has a very low Néel temperature, no exchange bias is expected for this sample. After annealing at 200 ℃, the composite consisted of a mixture of Ni and ferromagnetic NiO clusters. No exchange bias could be found in this sample (Fig. 5.9b), confirming that the small NiO clusters did not possess the antiferromagnetic nature.

High coercivity and exchange bias were found in the sample after annealing at 350 ℃, as shown in Fig. 5.10a. After annealing at 500 ℃ (Fig. 5.10b), there was a significant reduction in coercivity. As discussed previously, the sample anneakled at 350 ℃ had a small grain size of NiO. The grain size of NiO increased significantly after annealing at 500 ℃. This work showed that the grain size may play an important role in the coercivity and exchange bias. NiO with a grain size of approximately 2.8 *nm* can result in a high coercivity in a Ni/NiO exchange coupling system. Spin flopping and random field anisotropy, which may result from the small grain size of antiferromagnet, may be attributed to the high coercivity [16-18].

5.5.2 Temperature dependence of the exchange bias and coercivity of the composite annealed at 350 ^{o}C

Fig. 5.11 shows the temperature dependence of the exchange bias and coercivity of a Ni/NiO composite after annealing at 350 ℃. A strong temperature dependence of coercivity and exchange bias was found. At room temperature, both the coercivity and exchange bias were small. When the temperature was decreased to approximately 200

K, the coercivity increased significantly up to 2 *kOe*. The value is very large for Ni film since it is known that Ni is one of the soft magnetic materials. When the temperature was below 80 *K*, the coercivity increment became relatively stagnant. This may be related to the competition of dipolar interaction energy among Ni particles and the exchange coupling between Ni and NiO. Similarly, the exchange bias was close to zero when the temperature was above 200 *K* and drastically increased as the temperature decreased below 200 *K*. The blocking temperature of the composite can be determined to be approximately 200 *K*. It should be noted that a Ni/NiO composite annealed at the temperature other than 350 ^{o}C did not show a significant change of coercivity and exchange bias when the temperature decreases.

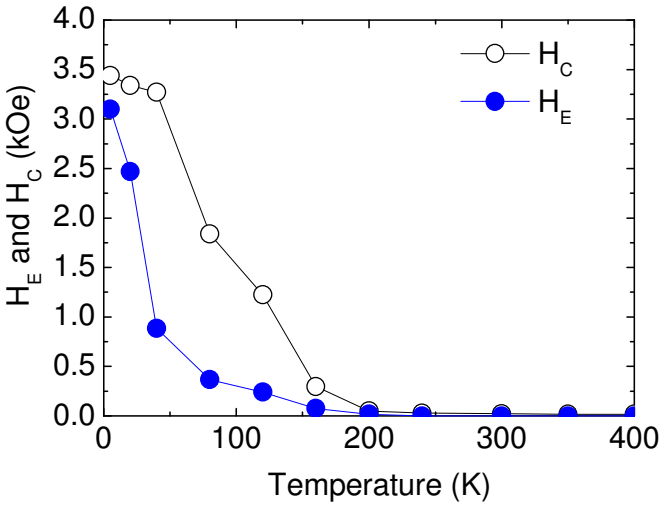

Fig. 5.11. Temperature dependence of the exchange bias (H_E) and coercivity (H_C) of a Ni/NiO composite annealed at 350 ^{o}C.

5.5.3 ZFC and FC curves of a Ni/NiO composite annealed at 350 ^{o}C

It is known that zero-field-cooling (ZFC) and field-cooling (FC) curves can determine the blocking temperature of a ferromagnet/antiferromagnet exchange coupling system. Fig. 5.12 shows the ZFC and FC curves of a Ni/NiO composite annealed at 350 ^{o}C.

The graph indicates that the blocking temperature is approximately 234 *K*, consistent with the temperature obtained from the curve of the exchange bias dependence on temperature, as shown in Fig. 5.11.

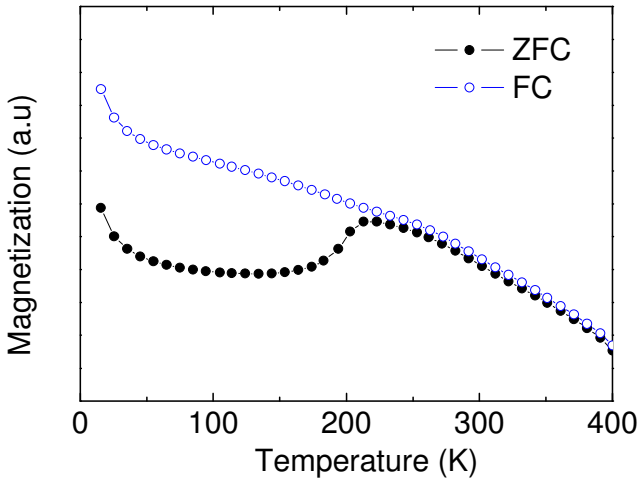

Fig. 5.12. ZFC and FC curves of a Ni/NiO composite annealed at 350 ^{o}C.

5.6. Composition effect

In this work, Ni and NiO with an atomic ratio of 1:1 (50 % Ni and 50 % NiO) were selected for the investigation of magnetization and magnetic properties. In order to clarify whether it is reasonable, the magnetic properties of other compositions were studied for a comparison. The coercivity and exchange bias of the composites with various compositions are listed in Table 5.1. From the table, if changing the composition of the composite to 30*t*% Ni and 70*t*% NiO, the coercivity was only 340 *Oe* at 5 *K* and the exchange bias was as small as 75 *Oe*. For the composite with 70 % Ni and 30 % NiO, the coercivity and exchange bias were also strongly reduced, indicating that the composition of 50 % Ni and 50 % NiO is ideal for the investigation. The composite with 50 % Ni and 50 % NiO has been discussed in the previous paragraphs, which has shown a high magnetization, high coercivity and large exchange

bias under the optimized condition. Hence, in the later chapter of this work, the composite with a composition of 50 % Ni and 50 % NiO is used for the investigation

Table 5.1 Composition effect of Ni and NiO on the coercivity and exchange bias. The exchange bias and coercivity were measured from the composite after annealing at 350 ^{o}C for 30 min.

Composition (*at %*)	Coercivity (*Oe*, 5 *K*)	Exchange bias (*Oe*, 5 *K*)
30Ni70NiO	340	75
50Ni50NiO	1605	3100
70Ni30NiO	510	15

5.7. Summary

In this chapter, crystalline Ni and amorphous NiO composite films were deposited. In the as-deposited film, the magnetization was relatively low. The composite showed a saturation magnetization of 91 *emu/g* at room temperature after annealing at 200 ^{o}C under an argon atmosphere. When the annealing was carryout out at 350 ^{o}C, the composite showed a remarkable high coercivity and large exchange bias at low temperatures. The high magnetization of Ni/NiO composite was due to the ferromagnetic behavior of NiO clusters, as shown experimentally and theoretically in Chapter 4. The coupling between Ni and NiO may be attributed to the high magnetization above room temperature. This means that the exchange coupling between Ni and NiO helps to establish the long range order of NiO clusters at room temperature. The high coercivity of a Ni/NiO composite annealed at 350 ^{o}C may be related to the small grain size of NiO. Due to the small grain size of NiO, the spin flopping and random field anisotropy may exist, resulting in high coercivities at low temperatures. The work clearly showed the grain size effect of NiO on the magnetic properties of Ni/NiO composites. NiO in a cluster state led to a high magnetization.

NiO with a grain size of 2–5 *nm* led to a high coercivity and large exchange bias. If the grain size of NiO was larger than 5 *nm*, a decrease in exchange bias and coercivity could be observed in the Ni/NiO composite.

References

[1]. S.U. Yuldashev, Y. Kim, N. Kim, H. Im, T.W. Kang, S. Lee, Y. Sasaki, X. Liu and J.K. Furdyna, Japn. J. Appl. Phys. 43, 2093 (2004).

[2]. J. Wu, G.S. Dong, and X.F. Jin, Phys. Rev. B 70, 212406 (2004).

[3]. R. Skomski and D.J. Sellmyer, J. Appl. Phys. 87, 4756 (2000).

[4]. U. Bovensiepen, F. Wilhelm, P. Srivastava, P. Poulopoulos, M. Farle, A. Ney, and K. Baberschke, Phys. Rev. Lett. 81, 2368 (1998).

[5]. A. Hernando, I. Navarro, C. Prados, D. Garcia, M. Vázquez, and J. Alonso, Phys. Rev. B 53, 8223 (1996).

[6]. A. Aspelmerier, M. Tischer, M. Farle, M. Russo, K. Baberschke, and D. Arvanitis, J. Magn. Magn. Mater. 146, 256 (1995).

[7]. F. May, M. Tischer, D. Aranitis, J.H. Dunn, H. Henneken, H. Wende, R. Chauvistré, and K. Baberschke, J. Phys. IV (France) 7C2, 389 (1997).

[8]. M. Gruyters, Phys. Rev. Lett. 95, 077204 (2005).

[9]. J. Morenzin, H. Kietzmann, P.S. Bechthold, G. Ganteför, and W. Eberhardt, Pure Appl. Chem. 72, 2149 (2000).

[10]. S.E. Apsel, J.W. Emmert, J. Deng, and L.A. Bloomfield, Phys. Rev. Lett. 76, 1441 (1996).

[11]. G.M. Chow, J. Ding, and J. Zhang, Appl. Phys. Lett. 80, 1028 (2002).

[12]. F. May, P. Srivastava, M. Farle, U. Bovensiepen, H. Wende, R. Chauvistré, and Babeschle, J. Magn. Magn. Mater. 177-181, 1220 (1998).

[13]. F. Nolting, E. Arenholz, A.T. Young, A. Scholl, H. Ohldag, and J. Stöhr, unpublished, http\\sls.web.psi.ch/view.php/science/docs/annual/sls97.pdf.

[14]. M. Jimbo, J. Kurita, K. Sakakibara, T. Goto, and T. Shigeoka, J. Magn. Magn. Mater. 199, 431（1999).

[15]. J. van Lierop, L.H. Lewis, K.E. Williamsb, and R.J. Gambino, J. Appl. Phys. 91, 7233 (2002).

[16]. S. Zhang and Z. Li, Phys. Rev. B 65, 054406 (2001).

[17]. S. Zhang, D.V. Dimitrov, G.C. Hadjipanayis, J.W. Cai, and C.L. Chien, J. Magn. Magn. Mater. 199, 468 (1999).

[18]. T.C. Schulthess and W.H. Butler, Phys. Rev. Lett. 81, 4516 (1998).

Chapter 6

Coercivity and Exchange Bias of Ni/NiO Nanocomposite Films Prepared by Oxidation during Magnetic Annealing

6.1 Introduction

In the last chapter, a Ni/NiO nanocomposite exhibited high coercivity and large exchange bias after annealing at 350 ℃. However, at room temperature, the coercivity and exchange bias were very low. Therefore, these materials need to be further developed to have a high coercivity and large exchange bias at room temperature in order to meet the requirements of practical applications. High coercivity materials are known to be candidates for permanent magnet and high density recording media [1,2].

As reported previously, magnetic annealing may induce certain microstructure, which can benefit coercivity [3-5]. In this chapter, Ni/NiO composites have been synthesized by the oxidation at a temperature of 380 ℃ under the application of a magnetic field.

6.2 Experimental procedure

Ni films with a nominal thickness of 50 *nm* were prepared by magnetron sputtering. The base pressure was 3×10^{-6} *torr*. The sputtering pressure was 7.5×10^{-3} *torr* and the power was 200 *W*. The as-deposited films were then magnetically annealed at 380 ^{o}C in an oven (Lakeshore, 4500), which was installed on a Lakeshore VSM 7300 system. In order to make sure the annealing temperature was higher than the Néel temperature of NiO (250 ^{o}C), the annealing temperature was chosen to be 380 ^{o}C. The applied field produced by VSM 7300 system is 0, 0.5, 1, 5 and 10 *kOe*, which direction is parallel to the film. During magnetic annealing, an oxygen partial pressure of oxygen of 0.0005, 0.001, 0.005 and 0.01 *torr* were flowed into the over to controlled the atmosphere by a digital flow meter. The film was cooled naturally to room temperature by switching off the heating powder. During the cooling, the magnetic field was still applied until to room temperature.

6.3 Effect of composition on the magnetic properties of Ni/NiO composite

In order to obtain high coercivity in a Ni/NiO composite, magnetic annealing was used for the sample preparation. In the last chapter, it showed that the composition of 50 % Ni and 50 % NiO in atomic ratio was optimal for the exchange coupling. In this chapter, oxygen partial pressure was varied in order to find the required partial pressure to obtain the desired composition of 50 % Ni and 50 % NiO. Table 6.1 shows the composite magnetization and composition of Ni in the dependence of oxygen partial pressure. From the table, the composition of the composite is close to 50 % Ni and 50 % NiO when the oxygen partial pressure is 0.001 *torr*. Indeed, the sample with a composition close to 50 % Ni and 50 % NiO showed the highest value of the coercivity and exchange bias at room temperature. The film exhibited a very high coercivity of 2.4 *kOe* and large exchange bias of 60 *Oe* at 298 *K*. The later study (as shown subsequently in this chapter) will be concentrated on the sample with a composition of 45.2 % Ni in atomic ratio. The results are compared with a Ni sample without magnetic annealing.

Table 7.1: The magnetization, composition, coercivity and exchange bias of Ni/NiO composites performed magnetic annealing at 380 ^{o}C under an oxygen partial pressure of 0 (N0), 0.0005 (N0a), 0.001 (N0b), 0.005 (N0c) and 0.01 torr (N0d) respectively. The composition was obtained by calculating the magnetization of the films.

	Ni Composition (at%)	Magnetization (*emu/g*)	Coercivity (*Oe*)	Exchange bias (*Oe*)
N0	100	54	200	0
N0a	67	41	490	5
N0b	45.2	24.4	2400	60
N0c	22.3	12.0	620	34
N0d	10.4	5.6	260	18

6.4 Effect of magnetic field on the magnetic properties of Ni/NiO composite

The effect of magnetic field on the nanocomposite during the magnetic annealing is shown in Fig. 6.1. The film after magnetic annealing under 0 *kOe* (N0e, dash) had a low coercivity (0.31 *kOe*) and small exchange bias (0.05 *kOe*). The film after magnetic annealing under 0.5 *kOe* (N0f, solid) showed a relatively large coercivity (1.0 *kOe*) and an exchange bias of 0.18 *kOe*. The exchange bias and coercivity of both N0e and N0f were much smaller than those of N0b performed magnetic annealing under 10 *kOe* (dot) (exchange bias 0.6 *kOe*, coercivity 5.9 *kOe* at 80 *K*). The result indicates the

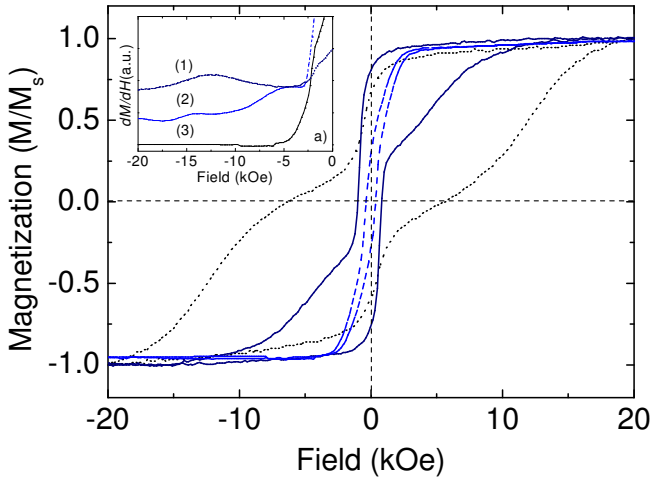

Fig. 6.1. The hysteresis loops of sample N0 films with a subsequently magnetic annealing under a field of 0 kOe (N0e, dash), 0.5 kOe (N0f, solid), and 10 kOe (N0b, dot), respectively. The oxygen partial pressure is 0.001 torr and the temperature is 380 ^{o}C.

importance of a sufficiently high magnetic field during magnetic annealing. A sufficient field is critical for the spin alignment of the interface between antiferromagnet/ferromagnet to induce an effective exchange coupling [8, 12]. The field for the alignment of the interface spins in a bilayer of Ni/NiO needs to be larger than 1 *kOe* [12]. In this study, magnetic field of 1 and 5 *kOe* was also applied for the magnetic annealing. The results showed that the hysteresis loops were similar to that

after annealing under a magnetic field of 10 *kOe*, indicating that the critical field was approximately 1 *kOe*.

6.5 Phase and microstructure analysis

6.5.1 XRD analysis

The highest coercivity (2.4 *kOe*) was achieved in a composite with a composition of 45.2 *at%* Ni. Hence, the film was studied in detail. The XRD spectrum of the sample is shown in Fig. 6.2. *Fcc*-Ni together with *fcc*-NiO phases was observed from this graph. Using Scherrer equation, the average grain size was calculated to be approximately 4.1 *nm* for NiO and 10.8 *nm* for Ni (both calculations are based on the (111) peak).

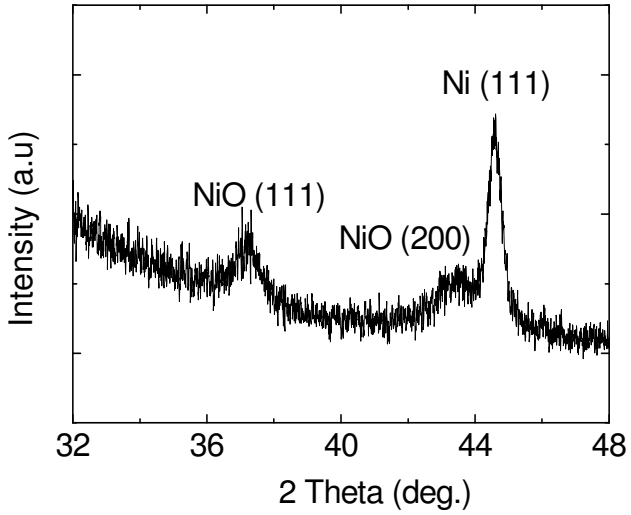

Fig. 6.2. XRD spectrum of a Ni film after magnetic annealing at 380 ^{o}C under an oxygen partial pressure of 0.001 torr.

6.5.2 TEM analysis

Fig. 6.3a shows the microstructure of and as-deposited pure Ni film analyzed by TEM. The grain size is in the range of 5–8 *nm*. A large amount of grain boundary was seen from the graphs. After the film was magnetically annealed under an oxygen partial

pressure of 0.001 *torr* at 380 ℃ (N0b, Fig. 6.3b), the shape of the grains changed to non-spherical. The grain size of the composite was smaller than that of the as-deposited film. In addition, no evident grain boundary could be observed. From the micrograph, fcc-Ni (111) with a d-spacing of 0.24 *nm* could be identified. The grain size of the NiO was less than 5 *nm*, consistent with XRD result. *Fcc*-Ni (111) with a d-spacing of 0.20 *nm* was also seen in the micrograph, indicating a composite of Ni and NiO. The grain size of Ni was estimated to be 8–10 *nm*, also in agreement with XRD analysis.

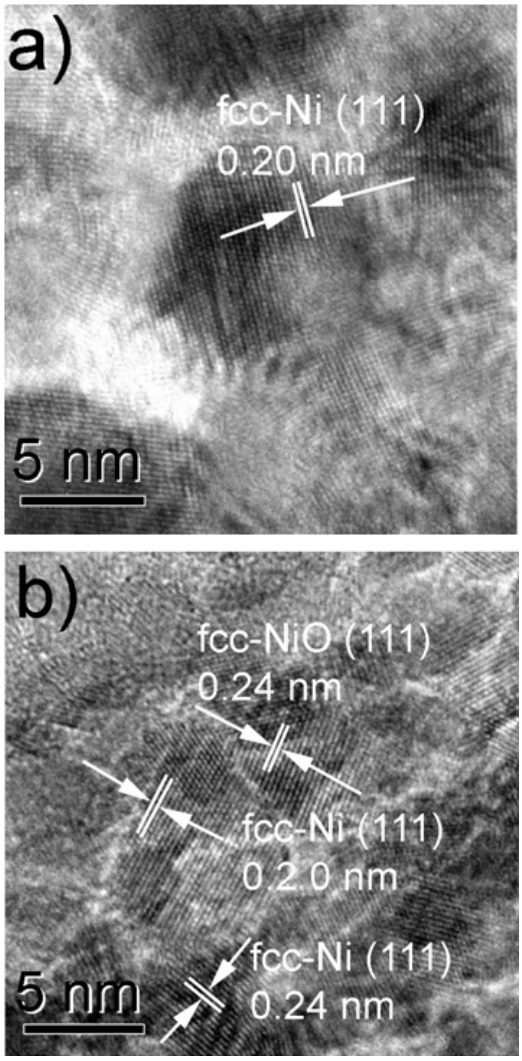

Fig. 6.3. TEM micrographs of a) N0 and b) N0 with a magnetic annealing at 380 ℃ for 20 min under an oxygen partial pressure of 0.001 torr (N0b).

The cross-section TEM micrograph of a Ni/NiO composite prepared by magnetic annealing is shown in Fig. 6.4. One layer of NiO was seen on the surface of the composite with a thickness approximately 5 *nm*. Inside the composite, both *fcc*-NiO (111) and *fcc*-Ni (111), Ni (200) could be identified, suggesting the formation of a composite. The graph showed that the average grain size of the NiO was smaller than 5 *nm*, consistent with the XRD and TEM results. As reported in [6,7], the oxidation of a metal film began from the surface and proceeded inside the film through the grain boundary of metallic film by the diffusion of metal or oxygen atoms. If there is a small amount of NiO phase in the composite, most of the NiO phase may be on the top of the film. The composite can be considered as a bilayer of the NiO and Ni (N0a). A small exchange bias (5 *Oe*) and low coercivity (490 *Oe*) were obtained, as shown in Table 6.1. When the film was further oxidized to the optimal condition (N0b, 54.8 % NiO), NiO was formed both on the surface and inside the film. The film then was a nanocomposite of the Ni and NiO.

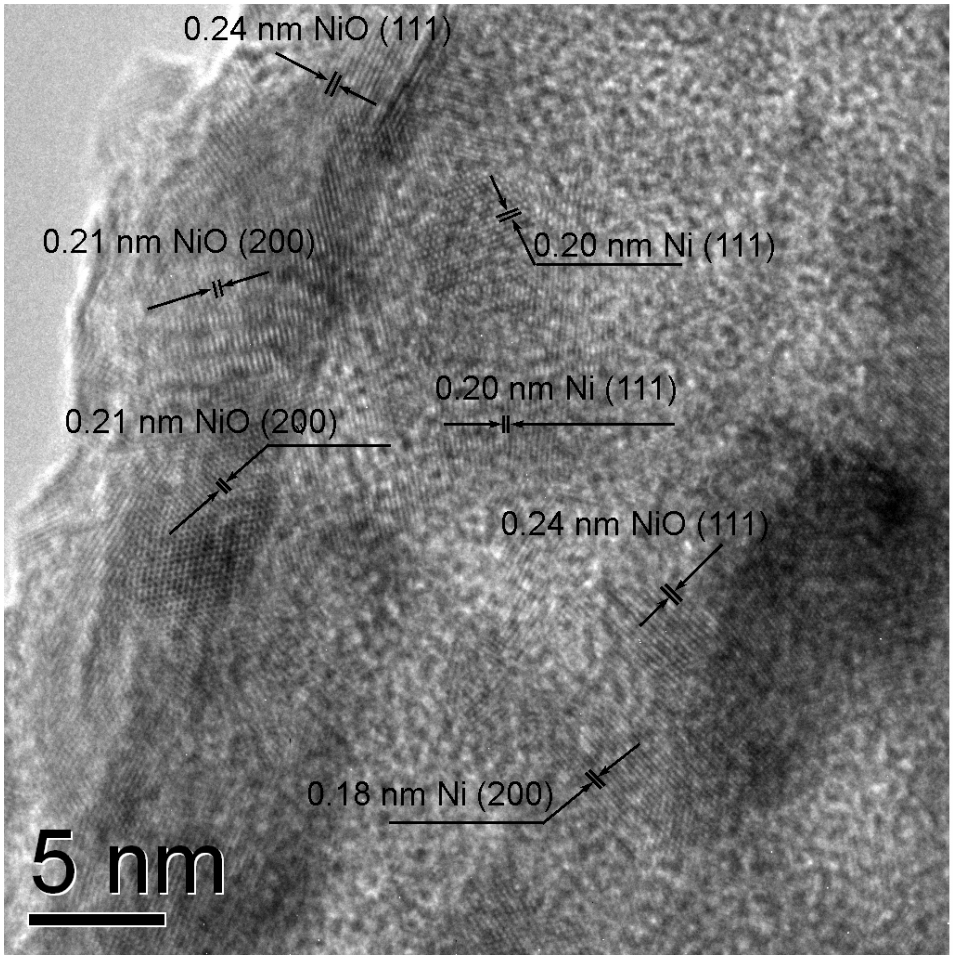

Fig. 6.4. Cross-section TEM micrograph of a Ni/NiO composite prepared by magnetic annealing.

6.6 Magnetic properties of Ni/NiO composites prepared by magnetic annealing

6.6.1 Room temperature hysteresis loops

The hysteresis loop of N0 and N0b taken at room temperature are illustrated in Fig. 6.5. The pure Ni film (N0) showed a low coercivity (0.21 *kOe*) and zero exchange bias since there was no antiferromagnetic component in the film. N0b showed a coercivity of 2.4 *kOe* with an exchange bias of 60 *Oe* at room temperature. Since Ni is one of the soft magnetic materials, it cannot possess so high coercivity. The small grains of the NiO may play an important role [9].

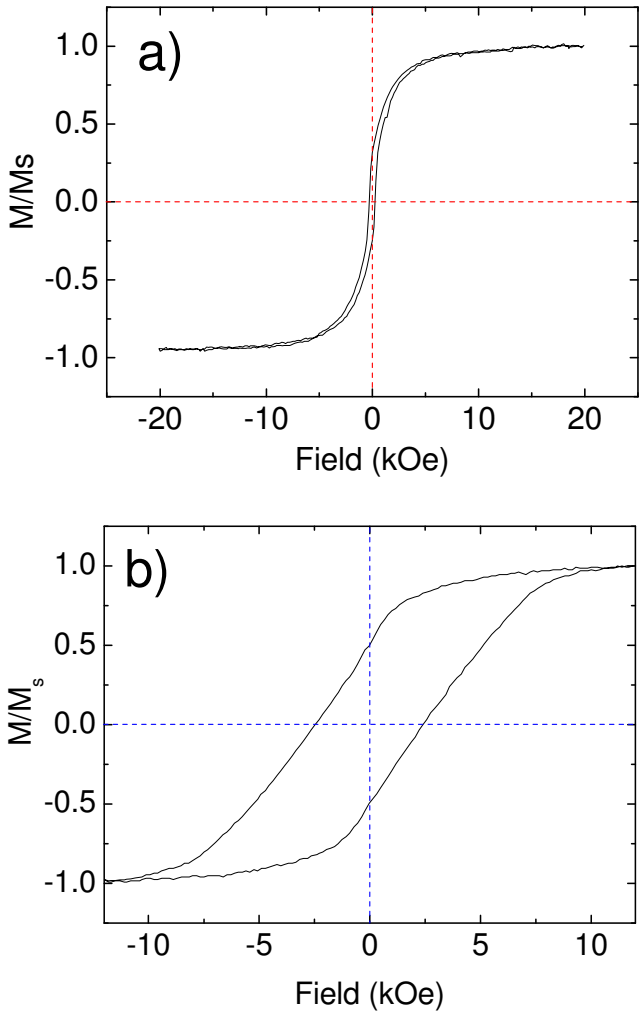

Fig. 6.5. Room temperature hysteresis loop of a) the as-deposited Ni film (N0) and b) the Ni film performed magnetic annealing at 380 ^{o}C under an oxygen partial pressure of 0.001 torr (N0b).

6.6.2 Temperature dependence of exchange bias and coercivity

The exchange bias and coercivity of the film as a function of the temperature are shown in Fig. 6.6. The exchange bias and coercivity did not change much between 240 and 295 *K*. Significant increment of the exchange bias and coercivity was observed when the temperature was below 240 *K*. The temperature dependence of the exchange bias and coercivity is similar, suggesting that the exchange coupling between Ni and NiO may be attributed to the high coercivity [10]. The coercivity reached 6.5 *kOe* and

the exchange bias was approximately 0.68 *kOe* at 80 *K*, which is much larger than reported (coercivity, 1.1 kOe and exchange bias, 0.3 K) [11].

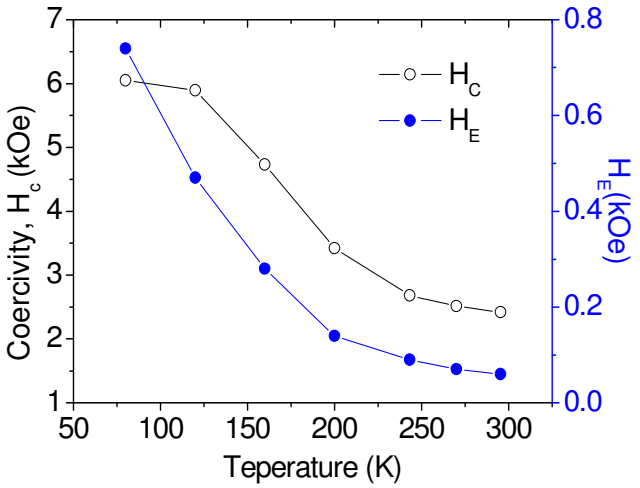

Fig. 6.6. Coercivity and exchange bias of N0b as a function of the temperature.

6.6.3 Blocking temperature

In Chapter 5, the high coercivity of a sputtered Ni/NiO composite after annealing at 350 ^{o}C could only be observed at a very low temperature. In this chapter, high coercivity of the composite after magnetic annealing at 380 ^{o}C was achieved at room temperature. From Chapter 4, the superparamagnetism of the NiO greatly affected the magnetic behavior of the Ni/NiO composite. The chapter indicated that if the blocking temperature (blocking temperature here is defined as the temperature when the exchange coupling between an antiferromagnet and ferromagnet disappears) was higher, the large coercivity might be achieved at a relatively higher temperature. The high coercivity at room temperature may be due to a high blocking temperature of the superparamagnetism of NiO. The zero-field-cooling (ZFC) and field-cooling (FC) curves showed that the blocking temperature of N0b was approximately 305 *K* (Fig.

6.7). The high blocking temperature of the composite may be due to the magnetic annealing method, in which NiO was formed through the grain boundary of metallic films via the diffusion of metal or oxygen atoms [6, 7]. This way of forming NiO may allow the NiO grains connect to each other. The connected NiO might result in an increase in the blocking temperature above room temperature. Hence, at room temperature, the exchange coupling between NiO and Ni may lead to a high coercivity. Fig. 6.6 showed that when the temperature decreased, the coercivity steadily increased, indicating that the exchange coupling may be attributed to the high coercivity [10,12,13].

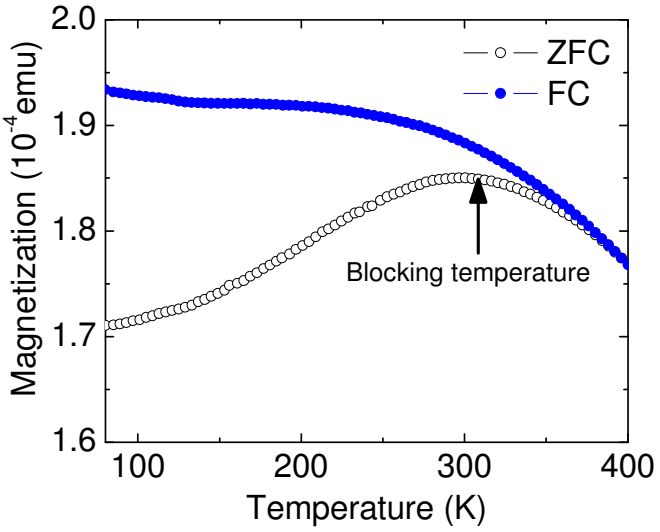

Fig. 6.7. Zero-field-cooling (ZFC) and field-cooling (FC) curves of a Ni/NiO composite prepared by magnetic annealing at 380 ^{o}C under an oxygen partial pressure of 0.001 torr (N0b) with an applied magnetic field of 10 kOe.

6.6.4 ΔM curve analysis

Fig. 6.8 shows $\Delta M(H)$ curve of the as-deposited Ni film and the magnetic annealed film with a high coercivity. A strong exchange coupling was observed in the as-deposited Ni film prepared by sputtering. However, negative $\Delta M(H)$ was shown in

the magnetically annealed films, suggesting dipolar coupling in the composite after annealing. The reduce exchange coupling (dipolar coupling) may be one of the reasons for the high coercivity [14, 15].

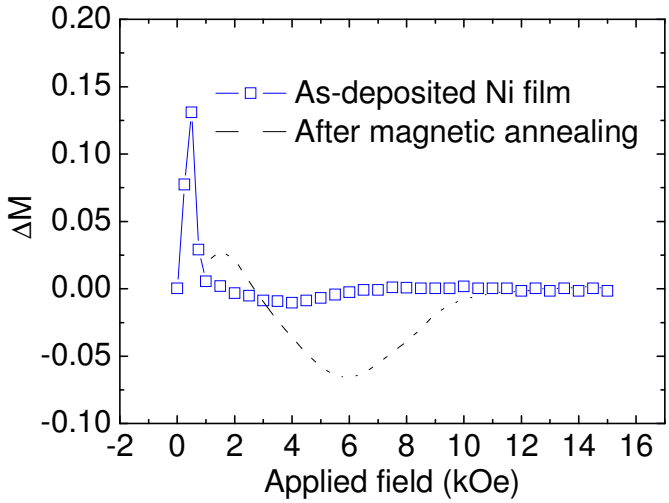

Fig. 6.8. ΔM curves of the as-deposited film and the as-deposited film after magnetic annealing at 380 ^{o}C under an oxygen partial pressure of 0.001 torr for 20 min (N0b).

6.7 Summary

In summary, a high coercivity of 2.4 *kOe* at room temperature was achieved in a Ni/NiO composite, which was formed by annealing Ni film in an oxygen partial pressure of 0.001 *torr* at 380 ^{o}*C* by applying a magnetic field of 10 *kOe*. The effect of the magnitude of the magnetic field on the magnetic properties of the composite during magnetic annealing was investigated in detail. In a Ni/NiO composite prepared by magnetic annealing, NiO had a small grain size. The small grain size (2-4 nm) of NiO may play an important role in the exchange coupling between Ni and NiO. The effective exchange coupling due to the small grain size of NiO results in a high coercivity. Compared to the relatively high coercivity at low temperature as discussed in Chapter 5, the composite in this work can show a relatively high coercivity at room

temperature. This may be due to the special preparation method. During magnetic annealing, NiO was initially formed on the surface. Then it was later formed by the diffusion of the oxygen or Ni atoms. The grain boundary and the NiO phase formed by the oxidation might act as the channels for the atoms diffusion. Hence, the NiO phases were connected to each other. The connected NiO phases showed a blocking temperature above room temperature. Hence, the strong exchange coupling resulted in a high coercivity beyond room temperature. However, other factors, e.g. the interface formation of the Ni/NiO during magnetic annealing above its Néel temperature, the dipolar interaction of Ni grains, may affect the coercivity and exchange bias.

References

[1]. F.S. Luborsky, Electro-Technology 9, 107 (1962).

[2]. S. Gangopadhyay, G.C. Hadjipanayis, C.M. Sorensen, and K.J. Klabunde, IEEE Trans. Magn. 28, 3174 (1992).

[3]. T. Suzuki, Z.G. Zhang, A.K. Singh, J.H. Yin, A. Perusal, and H. Osawa, IEEE Tran. Magn. 41,555 (2005).

[4]. Y.C. Wang, J. Ding, J.B. Yi, B.H. Liu, Y. Yu, and Z.X. Shen, Appl. Phys. Lett. 84, 2596 (2004).

[5]. Y.C. Wang, J. Ding, J.B. Yi, B.H. Liu, Y. Yu, and Z.X. Shen, J. Magn. Magn. Mater. 282, 211 (2004).

[6]. N. Cabrera and N.F. Mott, Reports Prog. Phys. 12, 163 (1949).

[7]. P.H. Holloway and J.B. Hudson, Surf. Sci. 43, 123 (1974).

[8]. M. Fraune, U. Rudiger, G. Guntherodt, S. Cardoso, and P. Freitas, Appl. Phys. Lett. 77, 3815 (2000).

[9]. C.H. Nam, B. K. Cho, and S. Lee, J. Appl. Phys. 93, 6584 (2003).

[10]. C. Leighton, J. Nogues, B.J. Akerman, and I.K. Schuller, Phys. Rev. Lett. 84, 3466 (2000).

[11]. J. van Lierop, L.H. Lewis, K.E. Williamsb, and R.J. Gambino, J. Appl. Phys. 91, 7233 (2002).

[12]. Y.J. Tang, D.J. Smith, B.L. Zink, F. Hellman, and A.E. Berkowitz, Phys. Rev. B 67, 054408 (2003).

[13]. A.E. Berkowitz and K. Takano, J. Magn. Magn. Mater. 200, 552 (1999).

[14]. Z.L. Zhao, J. Ding, K.Inaba, J.S. Chen, and J.P. Wang, Appl. Phys. Lett. 83, 2196 (2003).

[15]. J.G. Zhu and H.N. Bertram, J. Appl. Phys. 69, 4709 (1991).

Chapter 7

Coercivity and Exchange Bias of Co/CoO Nanocomposite Films Prepared by Oxidation during Magnetic Annealing

7.1 Introduction

In the previous chapters, Ni, NiO and Ni/NiO composite were prepared by sputtering or co-precipitation. Ni in an amorphous state has low magnetization. NiO in a cluster state displayed relatively high magnetization at low temperatures. A Ni/NiO composite could display a high coercivity and high magnetization that are dependent on the microstructure. Co is also one of the natural ferromagnetic materials. CoO has cubic structure similar to that of NiO. Hence, one may wonder whether Co, CoO and Co/CoO composite show similar magnetic properties to those of Ni, NiO and Ni/NiO composite.

7.2 Experimental procedure

Co films with a thickness of 50 *nm* were deposited on glass substrates by a magnetron DC sputtering system (Discovery 18, Denton, USA). The Co films were then magnetically annealed in a furnace with a flow of mixed gas (argon/oxygen, 100 *ml/min*). The magnitude of the applied field was 1000 *Oe*. The annealing temperature was 200 ^{o}C. The relatively low annealing temperature is to avoid the formation of Co^{3+}. In order to obtain a Co/CoO composite with a composition of 50 % Co and 50 % CoO in atomic ratio, the oxygen ratio of the mixed gas was varied to 1, 3, 5, 8, 10 % during the annealing. It was found that when the oxygen partial pressure was 3 %, the composition of the Co was 46.7 % close to 50 %. Oxygen in other ratios during annealing led to the composition of the Co far way from 50 %.

7.3 The results of Co and CoO prepared by sputtering

Firstly, Co films were deposited using sputtering. Experiments showed that the magnetization of a Co film was close to that of the bulk Co and the magnetization did

not depend on the sputtering power. These results are different from that of a Ni film. The magnetization of a Co film did not depend on the thickness either. From the TEM images, all the Co films showed well crystalline structures. Further investigation showed that a good linear relationship between the sputtering time and thickness was observed, which is similar to that of Ni film.

Secondly, CoO films were prepared by the deposition of Co films using sputtering under an oxygen partial pressure. From XRD spectrum, the as-deposited film was amorphous after the deposition under an oxygen partial pressure of 1.4×10^{-3} *torr*, similar to the NiO film deposited under a high oxygen partial pressure. However, from XPS analysis, both Co^{2+} and Co^{3+} coexisted in the film. It is known that Co_3O_4 is also an antiferromagnet with a Néel temperature of approximately 25 *K*, much lower than that of CoO (292 *K*). The mixture of the two phases (CoO and Co_3O_4) in the composite makes the investigation of the finite size effect difficult. When a Co/CoO composite was deposited alternatively similar to that of a Ni/NiO composite with a subsequent annealing at 200 ^{o}C, the composite showed low magnetization (85 *emu/g*) at room temperature and it should be noted that the composite might not be a pure Co and CoO mixture as Co^{3+} still existed. Hence, in this work, the Co/CoO composite prepared by sputtering was not investigated in detail. Efforts were also made to fabricate CoO powders. Similarly, CoO was easily oxidized to Co^{3+}. The finite size effect of Co_3O_4 powders have been studied by Salah A. Makhlouf [1]. The mixture of CoO and Co_3O_4 powders were not suitable for the magnetization and coercivity investigation. Therefore, the powders of CoO were not studied. From the discussion above, it is not easy to fabricate a pure CoO phase. In Chapter 6, it was showed that a Ni/NiO composite, formed by post annealing, demonstrated a high coercivity but low

magnetization at room temperature. In this work, the magnetic annealing method was used for the preparation of a Co/CoO composite. During the magnetic annealing, efforts were made to form the composite with a ratio of Co/CoO close to 50 %/50 %. XPS and Raman spectroscopy analysis indicated that the Co in the Co/CoO composite was in the divalent state.

7.4 Characterization and microstructure analysis

7.4.1 XRD analysis

Fig. 7.1 shows the XRD spectra of Co/CoO composites under different ratios of oxygen. The as-deposited film was a pure Co film with a mixture of *hcp* and *fcc* structure. After magnetic annealing under an oxygen ratio of 1 %, both the peak intensities of both *fcc*-Co (111) and *hcp*-Co (100) planes decreased. When the oxygen ratio was 3 % during magnetic annealing, the peak of *hcp*-Co (100) totally disappeared, while a weak peak of *fcc*-Co (111) still existed, and a CoO (200) peak could be clearly observed. The results indicated that after annealing in oxygen atmosphere with a ratio of 3 %, a Co/CoO composite was formed. When the oxygen ratio further increased to 10 %, no Co phase could be identified. The XRD scanning showed a CoO phase with the plane of CoO (111) and CoO (200).

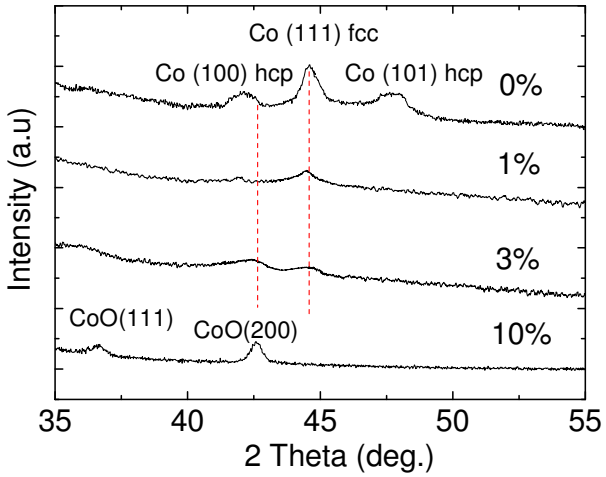

Fig. 7.1. XRD spectra of Co films after magnetic annealing under different oxygen ratios.

7.4.2 Raman spectroscopy analysis

The XRD spectra showed a structure evolution of a Co film after annealing under different ratios of oxygen. It is known that Raman spectroscopy is one of the most effective ways to observe nanostructured CoO phase [2, 3]. Hence, the prepared samples were studied by a Raman spectroscopy, as shown in Fig. 7.2. For the Co film annealed in an oxygen ratio of 0 % (pure Co film), no peaks could be observed, due to the pure metallic bond of Co films. When the oxygen ratio increased to 1 %, CoO phase was clearly shown. However, in the XRD analysis, CoO in this film could not be identified. The result suggests that a small amount of CoO may be formed when the oxygen ratio is 1%, though it cannot be detected by XRD. With increasing the oxygen ratio during magnetic annealing, the intensity of the corresponded peaks of the CoO increased, indicating an increase in the amount of the CoO. It should be noted that Co_3O_4 phase was not found from XRD or Raman spectra.

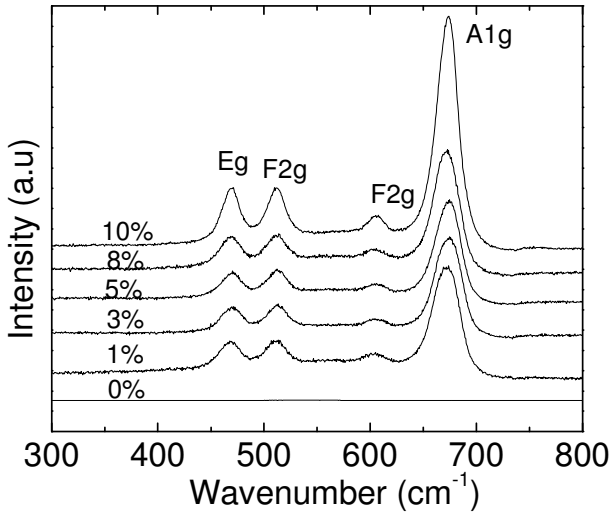

Fig. 7.2. Raman spectra of Co/CoO films annealed under an oxygen ratio of 1 %, 3 %,5 %, 8 % and 10 % at 200 ^{o}C , respectively.

7.4.3 TEM analysis

Fig. 7.3 shows the TEM micrographs of a pure Co film and Co/CoO composites prepared by magnetic annealing. The as-deposited film (Fig. 7.3a) showed that the grain size of the Co was 5–8 *nm*. Grain boundary could be clearly observed. After the film was annealed under an oxygen ratio of 3 %, the grain size strongly decreased (Fig. 7.3b). The grain size of the Co and CoO was 2–4 *nm*, similar to that of the Ni/NiO composite prepared by magnetic annealing in Chapter 5. When the oxygen ratio increased to 10 % (Fig. 7.3c), the grain size increased to 6–10 *nm*. From XRD spectra shown in Fig. 7.1 and the Raman spectra shown in Fig. 7.2, the phases corresponded to Co and CoO. The results show that a Co/CoO composite with a very small grain size (2–4 *nm*) can be formed using magnetic annealing.

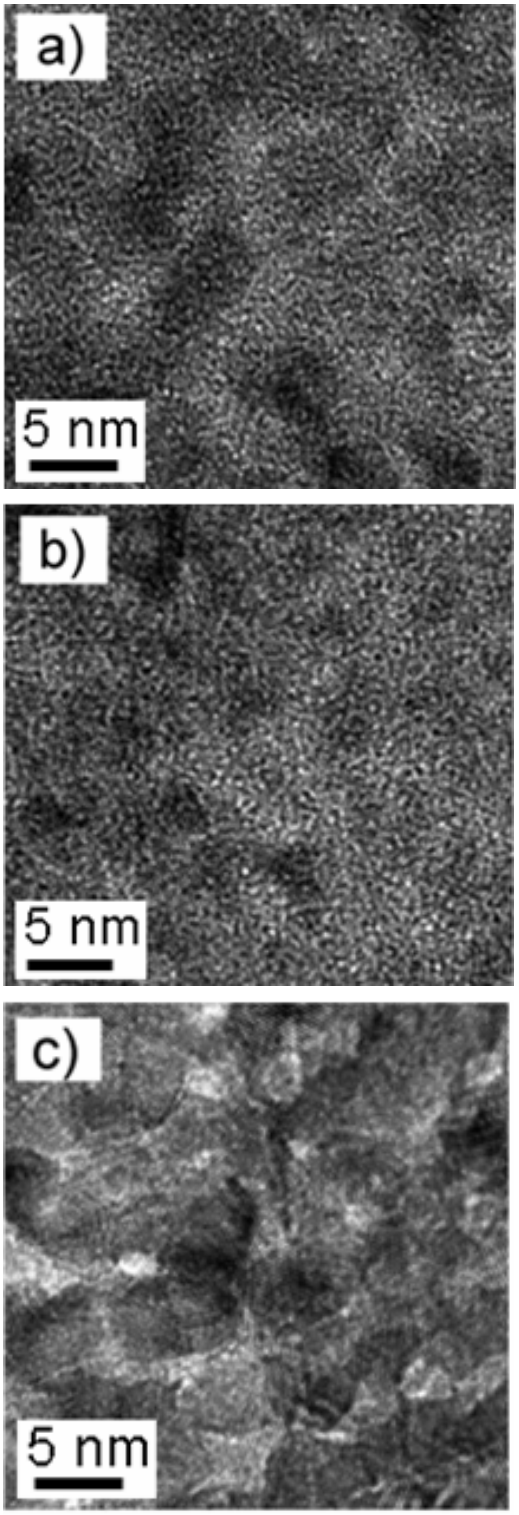

Fig. 7.3. HRTEM micrographs of a) a pure Co film; b) a Co film after magnetic annealing at 200 ^{o}C for 1 h under an oxygen ratio of 3 %; c) a Co film after magnetic annealing at 200 ^{o}C for 1 h under an oxygen ratio of 10 %.

7.5 Composition study and its effect on the magnetic properties

Fig. 7.4 indicates the saturation magnetization of the Co (oxygen ratio is zero) and Co/CoO composites under different ratios of oxygen. Fig. 7.4a showed that the magnetization decreased with increasing oxygen ratio. The results suggest an increase in the CoO phase in the composite since the magnetization is only contributed from Co

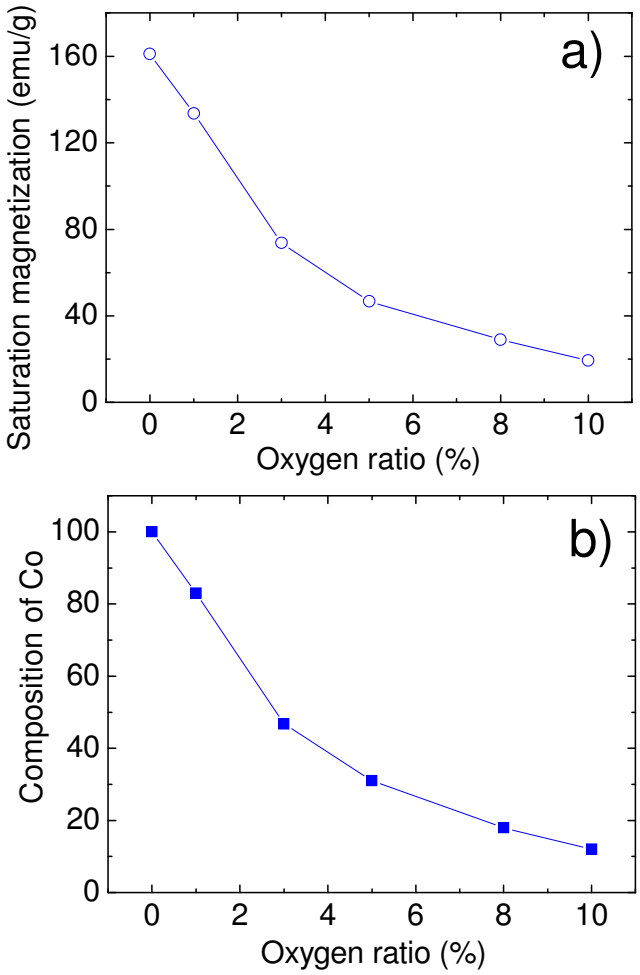

Fig. 7.4. a) The saturation magnetization of Co/CoO composites annealed under different oxygen ratios and b) the composition of the Co in Co/CoO composites annealed under different oxygen ratios.

phase. The magnetization decreased to approximately 10 *emu/g* when the oxygen ratio was 10 %. It is assumed that the magnetization is attributed to the ferromagnetic Co

because CoO is paramagnetic at room temperature. Based on the saturation magnetization of the Co (160 *emu/g*), the composition of the films can be calculated. The composition is shown in Fig. 7.4b. The graph showed that CoO phase monotonically increased with increasing the oxygen ratio. When the oxygen ratio was 3 %, the composition of the Co/CoO composite was 46.7 % Co and 53.3 % CoO in the atomic ratio.

Since the composition and microstructure (from TEM image) of Co/CoO composites varied significantly after annealing under different oxygen ratios, the magnetic properties of the composites should also vary. The coercivity and exchange bias of the composite prepared by annealing under a variation of oxygen ratios are shown in Fig. 7.5. Both the coercivity and exchange bias were low for low oxygen ratio. When the oxygen ratio was increased, the coercivity and exchange bias increased, which may be due to exchange coupling between Co and CoO. The largest coercivity and exchange bias were obtained when the oxygen ratio was 3 %. Further increasing the oxygen ratio, the coercivity and exchange bias decreased, indicating that 50 % Co and 50 % CoO is the optimal composition. When the oxygen ratio was too high, the Co phases were then totally isolated by the CoO phases. The weak dipolar interaction of Co grains may lead to a small exchange bias and low coercivity [4].

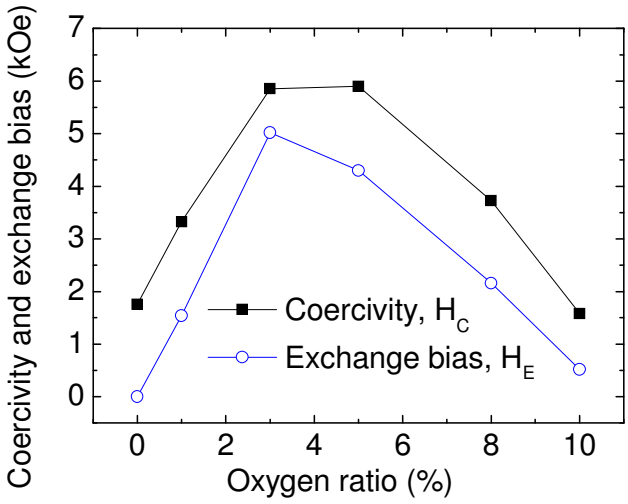

Fig. 7.5. The exchange bias and coercivity as a function of the oxygen ratio during magnetic annealing at 200 ^{o}C for 1 h (all the values were taken at 80 K).

7.6 Temperature dependence of the magnetic properties

Since exchange coupling of the Co and CoO may be attributed to the high coercivity and large exchange bias when the oxygen ratio was 3 %, the temperature dependence of the coercivity and exchange bias of the composite was measured as shown in Fig. 7.6. The coercivity and exchange bias increased monotonically with the decreasing temperature, suggesting the behavior is due to the exchange coupling between Co and CoO [5]. The exchange bias was zero when the temperature was 300 *K*, which is higher than the Néel temperature of the CoO (292 *K*). At 240 *K*, the exchange bias suddenly increased to approximately 200 *Oe*, suggesting that the blocking temperature was close to 240 *K*. Similarly, when at the temperature below 240 *K*, the coercivity evidently increased.

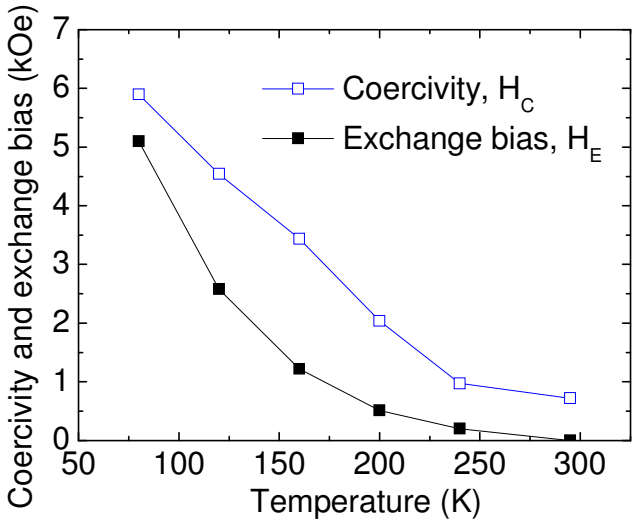

Fig. 7.6. The coercivity and exchange bias of a Co/CoO composite prepared by the annealing of a Co film under 3 % O_2 at 200 ^oC for 1 h.

Fig. 7.7 shows the zero-field-cooling (ZFC) and field-cooling (FC) curves of a Co/CoO composite after magnetic annealing under the oxygen ratio of 3 %. The applied field was 50 *Oe* for the field cooling and measurements. From the curve, one can see that the cusp of zero-field-cooling curve was approximately 275 *K*, which is supposed to be the blocking temperature of the composite [6]. The result agrees with that obtained from the temperature dependence of exchange bias, as shown in Fig. 7.6.

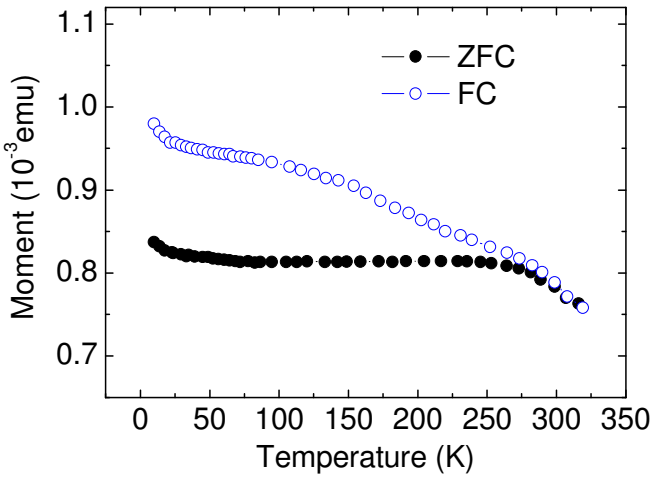

Fig. 7.7. ZFC and FC curves of a Co/CoO composite prepared by magnetic annealing.

7.7 Comparison of the hysteresis loops of a Co/CoO composite by magnetic annealing under an oxygen environment and by sputtering with an oxygen partial pressure

In order to conduct a comparison, a Co/CoO composite with a composition close to 50 %Co and 50 %CoO was prepared by reactive sputtering. Fig. 7.8 shows the hysteresis loops of the Co/CoO composites formed by magnetic annealing and reactive sputtering. The graph showed that the coercivity and exchange bias of the magnetically annealed sample were 5.9 and 5.5 *kOe* respectively, while the coercivity and exchange bias of a Co/CoO composite by reactive sputtering were much lower (coercivity, H_C=2.8 *kOe* and exchange bias, H_E=1.1 *kOe*). The ratio of remanence/saturation magnetization of the magnetically annealed sample (95.4 %) was also higher than that of the sample prepared by reactive sputtering (93 %). The result indicates that the magnetic annealing method to form a Co/CoO composite is one more effective way to achieve a high coercivity and large exchange bias. The small grain size of the CoO may play an important role for the high coercivity and large exchange bias.

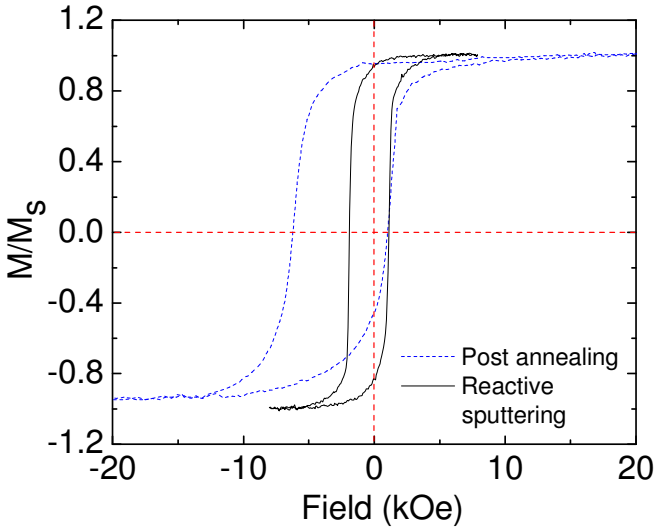

Fig. 7.8. Hysteresis loops (80 K) of a Co/CoO composite by the annealing of a Co film under 3 % O_2 at 200 ^oC for 1 h (dot) and a Co/CoO composite prepared by reactive sputtering under an oxygen partial pressure of 1×10^{-5} torr (solid).

7.8 Summary

In this chapter, magnetic annealing was used for the preparation of Co/CoO composites under an oxygen environment. The oxygen ratio effect on the magnetic properties was investigated. It was found that a Co/CoO composite could display a high coercivity and large exchange bias when the annealing temperature was 200 ^{o}C and the oxygen ratio was 3 %. The composite prepared using the magnetic annealing method showed a larger exchange bias and higher coercivity than those of the film prepared by reactive sputtering. Investigation showed that a Co/CoO composite prepared by magnetic annealing had a very small grain size, which is similar to that of a Ni/NiO composite, as shown in Chapter 6. The inhomogeneous exchange coupling due to the small grain size may be the reason for the high coercivity and large exchange bias. The work in this chapter suggests that magnetic annealing may be an effective way to form antiferromagnet/ferromagnet composite, which shows a strong exchange coupling, resulting in a relatively high coercivity and large exchange bias. The method may be useful as a guide to prepare magnetic materials for applications in hard magnetic materials and spintronic devices.

References

[1]. S.A. Makhlouf, J. Magn. Magn. Mater. 246, 184 (2002).

[2]. M. Magnuson, S.M. Butorin, J.H. Guo, and J. Nordgren, Phys. Rev. B 65, 205106 (2002).

[3]. L. Braicovich, M. Taguchi, F. Borgatti, G. Ghiringhelli, A. Tagliaferri, N.B. Brookes, T. Uozumi, and A. Kotani, Phys. Rev. B 63, 245115 (2001).

[4]. E. Girgis, R.D. Portugal, H. Loosvelt, M.J. Van Bael, I. Gordon, M. Malfait, K. Temst, C. Van Haesendonck, L.H.A. Leunissen, and R. Jonckheere, Phys. Rev. Lett. 91, 187202 (2003).

[5]. C. Leighton, J. Nogues, B.J. Jonsson-Akerman, and I. K. Schuller, Phys. Rev. Lett. 84, 3466 (2000).

[6]. J. Nogues and I.K. Schuller, J. Magn. Magn. Mater. 192, 203 (1999).

Chapter 8

Conclusions and Future Works

8.1. Conclusions

In this work, microstructure and magnetic properties of Ni, NiO, Ni/NiO, Co, CoO, and Co/CoO were studied in detail. The high magnetization and high coercivity of the Ni/NiO, Co/CoO samples were investigated. The results showed that exchange coupling was attributed to the high magnetization and high coercivity of the composite samples prepared by different methods. The details of the study are summarized below:

1) Ni films deposited with a high sputtering rate with a power of 200 *W* led to a disordered structure. The films showed relatively low magnetization compared with that of Ni bulk. The low magnetization is due to the existence of the disordered structure. A slow deposition rate with a power of 20 *W* resulted in a film with good crystallinity and the magnetization of the film was close to the bulk Ni (54 *emu/g*). It was also found that the thickness of the film was linear to the deposition time and the deposition power.

2) Amorphous nickel oxide films were successfully prepared by sputtering using a Ni target in an oxygen partial pressure of 1.4×10^{-3} *torr*. The susceptibility measurement of the sample showed that the amorphous NiO was antiferromagnetic with a Néel temperature of approximately 3.5 *K*.

3) NiO clusters (1-2 *nm*) were successfully fabricated by the co-precipitation method. With increasing the annealing temperature, the grain size of the NiO increased. By measuring the magnetic properties of the powders, it was found that the powders in the cluster state showed a maximum value of saturation magnetization of 105 *emu/g* at 2 *K*. The susceptibility measurement showed that the cluster NiO demonstrated a ferromagnetic behavior with a Curie

temperature of 35 *K*. The powders in the nanocrystalline state indicated much lower magnetization. And they showed a structure of uncompensated surface magnetic spins and antiferromagnetic core. In these powders, large exchange bias and high coercivity could be observed. The ferromagnetism of NiO nano-clusters was confirmed by the first principle calculations. The calculation results showed that nickel oxide in a fully amorphous state was antiferromagnetic. Nickel oxide in a cluster state was ferromagnetic with a maximum magnetic moment of 2 μ_B per Ni ion, agreeing well with the experimental results.

4) Ni/NiO composite films were prepared by an alternative deposition of Ni and NiO with thicknesses of 2 *nm*. Magnetic measurement showed that the film had low magnetization in the as-deposited state. When the film was annealed at 200 ^oC, a saturation magnetization of 91 *emu/g* could be observed at room temperature. The value is much higher than that of bulk Ni (54 emu/g). Ferromagnetic NiO clusters are attributed to the high magnetization. When the composite was annealed at 350 ^oC, a high coercivity and large exchange bias were obtained at low temperatures. However, the magnetization of the composite is very low. The investigation indicates that the size of the NiO plays an important role in the high coercivity and large exchange bias of a Ni/NiO composite. The exchange coupling between the NiO and Ni is attributed to the high coercivity and large exchange bias.

5) A Ni/NiO composite, which was prepared by annealing Ni film with an oxygen partial pressure under an applied magnetic field, showed a coercivity of 2.4

kOe at room temperature. The small grain size of NiO formed by oxidation is attributed to the high coercivity via the exchange coupling between NiO and Ni.

6) A Co/CoO composite was also prepared by annealing Co film in an oxygen environment with an applied field. The composite showed a high coercivity at low temperatures due to the low Néel temperature of CoO (292 *K*). A Co/CoO composite prepared by magnetic annealing showed a higher coercivity and remanence than those of the composite prepared by reactive sputtering measured at the same temperature (80 *K*).

8.2. Future works

1) This work indicated that NiO in a cluster state is ferromagnetic with high magnetization, which can be used for the preparation of high magnetization materials by exchange coupling with a ferromagnet, such as Ni. However, the magnetization of Ni is relatively low. Fe and FeCo alloy have a higher saturation magnetization. NiO/FeCo composites are more promising for the practical applications. Hence, the study of the magnetization of a NiO/FeCo composite may be of interest.

2) In this work, the high magnetization of a Co/CoO composite has not been obtained because of the limitation of the equipment. Another method, e.g. Molecular beam epitaxy (MBE), may be useful for the preparation of a Co/CoO composite with high magnetization.

3) In addition, the microstructure and magnetic properties of the Fe_2O_3 with different grain sizes may be of interest as it is one of the antiferromagnets with

a very high Néel temperature. The composite of Fe/Fe_2O_3 may be promising for commercial applications, if high coercivity and/or high magnetization can be achieved.

4) The physics of the exchange-coupled NiO/Ni and CoO/Co composites needs to be further investigated. It would also be interesting to study the magneto-transport properties for spintronic applications.